

**Experimental Investigation of Magnetohydrodynamic  
Flow For An Intense Proton Target**

A Dissertation Presented

by

**Hee Jin Park**

to

The Graduate School  
in Partial Fulfillment of the  
Requirements  
for the Degree of

**Doctor of Philosophy**

in

**Mechanical Engineering**

**Stony Brook University**

August 2008

**Stony Brook University**

The Graduate School

**Hee Jin Park**

We, the dissertation committee for the above candidate for the  
Doctor of Philosophy degree,  
hereby recommend acceptance of this dissertation.

---

Foluso Ladeinde, Dissertation Co-Advisor,  
Professor, Department of Mechanical Engineering

---

Harold G. Kirk, Dissertation Co-Advisor,  
Physicist, Department of Physics, Brookhaven National Laboratory

---

Lili Zheng, Chairperson of Defense,  
Professor, Department of Mechanical Engineering

---

Kirk T. McDonald , Outside Member,  
Professor, Physics Department, Princeton University

---

James Glimm, Outside Member,  
Professor, Department of Applied Math. & Stat., Stonybrook University

This dissertation is accepted by the Graduate School.

---

Lawrence Martin  
Dean of the Graduate School

Abstract of the Dissertation

**Experimental Investigation of Magnetohydrodynamic  
Flow For An Intense Proton Target**

by  
**Hee Jin Park**  
**Doctor of Philosophy**  
in  
**Mechanical Engineering**  
Stony Brook University  
**2008**

Efficient production of pions can be achieved by colliding an intense proton beam with a high-Z target. The experiments of Hg jet on the interaction of an intense proton beam in magnetic field has been carried out for the thesis work. The primary diagnostics in this work employed the technique of back-illuminated laser shadow photography to freeze the transient events. The images are recorded by several high speed cameras. The performance of the optical diagnostic system is presented.

Flowing mercury in a magnetic field causes induced currents, which produce distortions of the mercury jet. The effect of Lorentz force is investigated theoretically in a stability analysis of the conducting flow in the presence of a magnetic field. The effects of Lorentz force on the vortices are also investigated

qualitatively. The role of joule damping as a loss on a time scale of magnetic damping term in global kinetic energy is discussed.

Quantitative and qualitative data analysis using image processing based on probability approach is described. The experimental measurement of the various dynamic behaviors of Hg jet in magnetic field through image processing is presented. In experiment, it is observed that the imposition of magnetic field tends to suppress the fluctuating motion in Hg jet and correspondingly the jet surface is more stabilized, where the  $Re$  is large enough and the  $Re_m$  is 0.26. Finally, the disruption of Hg jet with the proton beam and the magnetic field effect to its suppression are presented. The collected images of beam-jet interaction shows the response of Hg jet due to the proton beam induced energy deposition. The filament velocity induced by the energy deposition and the time response of the velocity in magnetic field is presented, where joule damping effect is explained. The experimental results investigated the performance and feasibility of utilizing liquid jet as a target for future accelerator. The experimental key components were designed and constructed at Princeton University, ORNL, MIT Plasma Science and Fusion Center, CERN, and BNL respectively.





# Table of Contents

List of Figures	xvii
List of Tables	xviii
Acknowledgements	xix
Nomenclature	xxiii
<b>1 Introduction</b>	<b>1</b>
1.1 Neutrino Factory For High Power Neutrino Beam . . . . .	1
1.1.1 The concept of neutrino factory . . . . .	1
1.1.2 Neutrino physics . . . . .	3
1.2 A High Power Target For Neutrino Factory . . . . .	4
1.2.1 Material consideration for a high power target . . . . .	4
1.2.2 Moving metallic target for pion production . . . . .	5
1.2.3 Free mercury jet flow in magnetic field for a high power target . . . . .	6
1.2.4 Impact of the MHD mercury jet experiment for an in- tense proton target . . . . .	8
1.3 Mercury Target Issues . . . . .	9

1.3.1	Mercury jet disruption by energy deposition from an intense proton beam . . . . .	9
1.3.2	Magnetohydrodynamic issues in mercury jet target . .	10
1.3.3	Overview of experimental investigation of MHD flow and discussion . . . . .	11
<b>2</b>	<b>Magnetohydrodynamic Issues of Mercury Flow in Magnetic Field</b>	<b>18</b>
2.1	Governing Equations for MHD Flow . . . . .	20
2.1.1	Electromagnetic equations . . . . .	20
2.1.1.1	<i>electromagnetic relation in a linear material</i> .	21
2.1.1.2	<i>Maxwell's equations</i> . . . . .	22
2.1.2	The Navier Stokes and magnetic induction equations in a conducting liquid flow . . . . .	23
2.1.2.1	<i>magnetic Reynolds number</i> . . . . .	26
2.1.2.2	<i>frozen-in theorem in magnetic induction equation</i>	27
2.1.2.3	<i>the diffusion limit in induction equation</i> . . .	28
2.2	The Energy Equation in MHD . . . . .	28
2.2.1	Energetics and effects of Lorentz force . . . . .	29
2.2.2	Magnetic damping with joule dissipation . . . . .	30
2.3	Vorticity Equations in MHD flow . . . . .	32
2.3.1	Governing equations for vorticity . . . . .	33
2.3.2	Vorticity suppression . . . . .	34
2.3.2.1	<i>spanwise magnetic field effect to vorticity suppression</i> . . . . .	35

2.3.2.2	<i>longitudinal and transverse magnetic field effect to vorticity suppression</i> . . . . .	35
2.4	One Dimensional Pipe Flow in Transverse Magnetic Field . . .	37
2.4.1	Non-dimensional form of the governing equations using cylindrical coordinates . . . . .	38
2.4.1.1	<i>boundary conditions in pipe flow</i> . . . . .	39
2.4.2	Exact solutions of pipe flow in magnetic field . . . . .	39
2.5	Stability of Conducting Flow in a Magnetic Field . . . . .	40
2.5.1	Propagation of waves at an interface separating two flows in magnetic field . . . . .	41
2.5.2	Magnetic pressure and tension . . . . .	43
<b>3</b>	<b>Experimental Method for Investigation of Magnetohydrodynamic Mercury Jet Flow</b>	<b>47</b>
3.1	Optical Diagnostics as a Principal Diagnostics of High Power Target Experiment . . . . .	48
3.1.1	Working principle of shadowgraph for optical diagnostics	48
3.1.2	Development of optical diagnostic system . . . . .	50
3.1.2.1	<i>the optical imaging system and viewports design</i>	51
3.1.2.2	<i>the consideration for focusing and tilting alignment of optics</i> . . . . .	55
3.1.2.3	<i>high speed cameras and light sources</i> . . . . .	56
3.1.2.4	<i>radiation-hardness</i> . . . . .	59
3.1.2.5	<i>scintillating fiber channel</i> . . . . .	60
3.1.3	Schematic of electronic trigger and high speed camera control . . . . .	61

3.2	Windows Consideration as Viewports for Observation . . . . .	63
3.2.1	Fiducial mark on windows . . . . .	63
3.2.2	Impact resistance test . . . . .	63
3.2.3	Pressure leaking test of sapphire windows . . . . .	64
3.3	Integrated Experimental Setup for High Power Target . . . . .	64
3.3.1	Mercury loop system in solenoid magnet . . . . .	64
3.3.1.1	<i>the considerations in nozzle design</i> . . . . .	66
3.3.2	Water jet observation for nozzle performance test . . . . .	67
<b>4</b>	<b>Results of Experimental Investigation of MHD Flow for an Intense Proton Target</b>	<b>78</b>
4.1	Image Analysis for Data Reduction . . . . .	79
4.1.1	Image acquisition . . . . .	79
4.1.2	Image processing . . . . .	80
4.1.3	Study on the scaling length and the location of center of window . . . . .	82
4.2	Motion of Mercury Jet and Stability in Magnetic Field . . . . .	84
4.2.1	Jet deflection and surface flattening . . . . .	84
4.2.2	Trajectory of mercury jet projectile in magnetic field . . . . .	90
4.2.3	Pressure loss and magnetic effect to the Hg delivery pipe . . . . .	92
4.2.3.1	<i>pressure loss in pipe flow</i> . . . . .	94
4.2.3.2	<i>the measurement of wall tap pressure</i> . . . . .	98
4.3	Interaction of an Intense Proton Beam with the Hg Jet in a Magnetic Field . . . . .	99
4.3.1	Proton Beam dynamics . . . . .	99
4.3.1.1	<i>pulse structure</i> . . . . .	101

4.3.1.2	<i>proton beam characteristics . . . . .</i>	102
4.3.2	Mechanism of the interaction and the Hg jet response to the energy deposition by the proton beam . . . . .	102
4.3.2.1	<i>Hg jet pressurization by energy deposition of proton beam . . . . .</i>	102
4.3.2.2	<i>typical beam-jet interaction in magnetic field .</i>	103
4.3.3	Hg jet disruption and magnetic suppression of the dis- ruption . . . . .	104
4.3.3.1	<i>characteristics of beam structure in disruption length, harmonic 8 and 16 . . . . .</i>	105
4.3.3.2	<i>disruption length with 14 GeV proton beam .</i>	106
4.3.3.3	<i>disruption length with 24 GeV proton beam .</i>	106
4.3.3.4	<i>validation of measurements of Viewport 3 through comparison with Viewport 4 . . . . .</i>	107
4.3.4	Damping of filaments in a magnetic field . . . . .	108
4.3.4.1	<i>triggering timing of high speed camera consid- ering the electronic delay . . . . .</i>	108
4.3.4.2	<i>Onset of filamentation on the jet surface . . .</i>	109
4.3.4.3	<i>filaments velocity with 14 GeV beam in a mag- netic field . . . . .</i>	109
4.3.4.4	<i>filaments velocity with 24 GeV beam in a mag- netic field . . . . .</i>	110
4.3.4.5	<i>delay of onset of filamentation and transient time response of filament in a magnetic field .</i>	110

## 5 Conclusions 152

<b>Bibliography</b>	<b>159</b>
<b>A Tabular Data for Chapter 3 and Chapter 4</b>	<b>165</b>
A.1 Specifications of Optics . . . . .	165
A.2 Mercury Properties . . . . .	167
<b>B Mathematical Derivation for Chapter 2</b>	<b>168</b>
B.1 The governing equations for MHD in cylindrical coordinates .	168
B.2 Derivation of Rayleigh's instability at an interface separating two flows in magnetic field . . . . .	170
B.2.1 <i>kinematic boundary condition at interface</i> . . . . .	170
B.2.2 <i>hydrodynamic stability in magnetic field</i> . . . . .	171
B.2.3 <i>dynamic boundary condition at interface</i> . . . . .	172

# List of Figures

1.1	Pion yield versus atomic mass number of the target at three proton beam energies, Osaki (2001) and Mokhov (2000). . . .	14
1.2	Pion yield from Hg targets versus tilt angle between the target/beam axis and the solenoid axis and versus the radius of the target, Osaki (2001) and Mokhov (2000). a.) Pion yield versus tilt angle. b.) Pion yield versus target radius. . . . .	15
1.3	Geometry of key elements of target system and Viewports, showing the overlap between the mercury jet, magnetic axis, and the proton beam. a.) Top view. b.) Side view. . . . .	16
1.4	Schematics of the relative overlap between proton beam axis, Hg jet axis , and solenoid magnet axis. . . . .	17
2.1	Wave-shaped interface separating two different fluids traveling at different average speeds. . . . .	45
2.2	Axes and electrodes of circular duct. . . . .	46
3.1	Displacement of light beam for shadowgraph. . . . .	68



3.2	Design of optical layout and installation of 4 Viewports of primary containment vessel. a.) Conceptual integration of optics to primary containment vessel. b.) Photograph of installation of optics to primary containment vessel. c.) Schematic layout of optical components. . . . .	69
3.3	Photograph of optical head assembly and its illumination of laser. a.) Front view of optical head assembly. b.) Side view of optical head assembly. c.) Illumination of fiber-optics head assembly. . . . .	70
3.4	Polished fiber end, 50X and 800X magnifications, respectively	71
3.5	Schematic of synchronized signal of high speed camera and laser pulse. . . . .	72
3.6	Schematic of electrical triggering and high speed camera control in tunnel for experiment. . . . .	73
3.7	Top fiducial on the front window and bottom fiducial on the rear window. a.) Photo of fiducial on the sapphire window assembled in Viewport. b.) Image of fiducial captured by camera.	74
3.8	Photographs of the entire MERIT experiment. a.) Sectional side view of mercury loop system integrated with 15 T solenoid magnet. b.) Fabricated mercury loop system assembled with 15 T solenoid magnet (Top view). . . . .	75
4.1	Image data conversion for image analysis. a.) Collected image data. b.) 2 bit scaled image data. . . . .	116
4.2	Sensitivity of threshold in a 2 bit scaled image conversion. . .	117

4.3	Jet height determination from image analysis. a.) Histogram of number of events in the jet height measurement. b.) Fitted histogram distribution. . . . .	118
4.4	Mercury jet flows as observed from the 3 Viewports. The jet flows from left to right on each image. The first, second, and third columns represent Viewport 1, 2, and 3, respectively. The individual caption shows the applied magnetic induction field. The jet velocity is 15m/s. Images on Viewport 2 has a 14° clockwise rotation due to the SMD software. a.) B=0T. b.) B=0T. c.) B=0T. d.) B=5T. e.) B=5T. f.) B=5T. g.) B=10T. h.) B=10T. i.) B=10T. j.) B=15T. k.) B=15T. l.) B=15T. .	119
4.5	Same as Fig. 4.4 but with a jet velocity of 20 m/s. a.) B=0T. b.) B=0T. c.) B=0T. d.) B=5T. e.) B=5T. f.) B=5T. g.) B=10T. h.) B=10T. i.) B=10T. j.) B=15T. k.) B=15T. l.) B=15T. . . . .	120
4.6	Calculated solenoid magnetic induction field map. a.) Radial field map. b.) Axial field map. c.) Transverse component of magnetic induction field along jet axis. d.) Longitudinal component of magnetic induction field along jet axis. . . . .	121
4.7	Hg jet height measurement in magnetic field by fitting estimation. a.) Jet height. b.) Jet height ratio. . . . .	122
4.8	Hg jet height measurement in magnetic field by direct average. a.) Jet height. b.) Jet height ratio. . . . .	123
4.9	Intermittency of Hg jet at Viewport 2. The jet velocity is 15 m/s. a.) B=0T. b.) B=5T. c.) B=10T. d.) B=15T (continued).	124

4.9	Intermittency of Hg jet at Viewport 2. The jet velocity is 20 m/s. e.) B=0T. f.) B=5T. g.) B=10T. h.) B=15T. . . . .	125
4.10	Surface fluctuations in a magnetic field. . . . .	126
4.11	Trajectory of beam axis and Hg jet axis projectile with respect to magnetic axis in magnetic field. . . . .	127
4.12	Hg jet angle at the center of magnetic axis (Viewport 2) as a function of magnetic field. . . . .	128
4.13	Pipe inlet pressure for the driving jet. a.) Static pressure. b.) Dynamic pressure. . . . .	129
4.14	Longitudinal Hg jet flow velocity in magnetic field. . . . .	130
4.15	Infrastructures for experiment at CERN. a.) Proton synchrotron and TT2 tunnel for experiment. b.) 16 harmonics of beam extraction in proton synchrotron. . . . .	131
4.16	Installation of integrated experimental components in tunnel TT2/TT2A for high power target experiment. . . . .	132
4.17	Photographs of the Hg jet interaction with 16 TP, 14 GeV/c proton beam at 5 T. Captured at Viewport 3 at 500 $\mu$ s frame rate (continued). . . . .	133
4.17	Photographs of the Hg jet interaction with 16 TP, 14 GeV/c proton beam at 5 T. Captured at Viewport 3 at 500 $\mu$ s frame rate (continued). . . . .	134
4.17	Photographs of the Hg jet interaction with 16 TP, 14 GeV/c proton beam at 5 T. Captured at Viewport 3 at 500 $\mu$ s frame rate. . . . .	135

4.18	Calculated energy deposition density to cross sectional area of Hg jet with 14 GeV/c proton beam in 0 T (Striganov, 2008). .	136
4.19	Calculated energy deposition density to cross sectional area of Hg jet with 24 GeV/c proton beam in 0 T (Striganov, 2008). .	137
4.20	Standard deviation of disruption length as a function of disruption length and the function of fitted curve. The fitted curve is $\sigma_{disruption} = 2.99 + 0.6144 \ln(L_{disruption} - 2.7062)$ . . . . .	138
4.21	Proton beam pulse structure of harmonic 8 and harmonic 16 in 14 GeV and 6 TP. . . . .	139
4.22	Disruption length of Hg jet depending on the beam pulse structure as a function of 14 GeV beam intensity in 5 T. $TP = 10^{12}$ protons . . . . .	140
4.23	Disruption length of Hg jet as a function of 14 GeV beam intensity and magnetic field. Harmonic 16 with 16 bunches is used. . . . .	141
4.24	Disruption length of Hg jet as a function of 24 GeV beam intensity and magnetic field. . . . .	142
4.25	Validation of disruption measurement for the evaluation of evolution of disruption length from Viewport 3. a) Disruption length at Viewport 3. b.) Disruption length at Viewport 4. c.) Difference of the disruption length at Viewport 3 and Viewport 4. . . . .	143
4.26	The triggering time for high speed camera upon beam arrival.	144

4.27	Photographs of filament evolution on the Hg jet surface as a function of time at 25 $\mu$ s frame rate. The beam is 10 TP, 24 GeV. The magnetic field is 10 T. . . . .	145
4.28	Filament velocity as a function of 14 GeV beam intensity and magnetic field. . . . .	146
4.29	Filament velocity as a function of 24 GeV beam intensity and magnetic field. . . . .	147
4.30	Time response of filament velocity as a function of magnetic field with 14 GeV, 20 TP beam. . . . .	148
4.31	Time response of filament velocity as a function of magnetic field with 24 GeV, 10 TP beam. . . . .	149
4.32	Energy decay in magnetic fields. . . . .	150
4.33	Integrated total energy with respect to time in magnetic fields.	151

# List of Tables

3.1	Specifications of high speed cameras. . . . .	76
3.2	Effects of irradiation up to an equivalent radiation dose of 1 Mrad on the reflectance and transmittance of the components of the optical diagnostic system. Reflectance is inferred on the Au-coated mirror and transmittance is inferred on all other components. . . . .	77
4.1	Pressure head losses by geometry in pipe for mercury loop. . .	113
4.2	Characteristics of the proton beam (Efthymiopoulos, 2008). . .	114
4.3	Estimated values of jet trajectory in magnetic fields. . . . .	115
A.1	Specifications of optical components in optical diagnostics. . .	165
A.2	Properties of mercury. . . . .	167

## ACKNOWLEDGEMENTS

The author greatly appreciates the indispensable guide and constant encouragements from Dr. Harold Kirk at Brookhaven National Laboratory and Prof. Foluso Ladeinde, who served as the author's dissertation advisor.

The author would like to express a special appreciation to Prof. Kirk McDonald at Princeton University and Dr. Thomas Tsang at Brookhaven National Laboratory for their contribution to the procedures used in this work.

The author would also like to thank Prof. Lili Zheng for agreeing to be the Chair of his dissertation committee, Prof. James Glimm, for agreeing to serve on the dissertation committee, Prof. Roman Samulyak, for valuable suggestions on the analysis of the experimental results.

This work was supported in part by the United States Department of Energy Contract No. DE-AC02-98CH10886. The experiment was carried out at CERN (European Organization for Nuclear Research) in Geneva, Switzerland and the analysis performed at Brookhaven National Laboratory. The text of this dissertation in part is a reprint of the materials as it appears in Review of Scientific Instruments **79**, 045111(2008). The co-authors listed in the publication directed and supervised the research that forms the basis for this dissertation.

Finally, the author wishes to express his deep appreciation to his family for the encouragement and support.

## Nomenclature

<b>B</b>	Magnetic induction field, $T$ ( $Wb/m^2$ )
<b>H</b>	Magnetic field, $A/m$
<b>E</b>	Electric field, $N/C$ ( $V/m$ ); Global kinetic energy, $J$
<b>J</b>	Current density, $A/m^2$
<b>V</b>	Electric potential, $V$
<b>D</b>	Electric displacement field, $C/m^2$ ; Energy dissipation, $J/s$
<b>P</b>	Polarization density, $C/m^2$ ; Probability
<b>M</b>	Magnetization density, $J/(T \ m^3)$
$T$	Temperature, $^{\circ}C$ ( $K$ )
<b>B<sub>o</sub></b>	Applied magnetic field, $T$ ( $Wb/m^2$ )
$v$	Directional fluid velocity, $m/s$ ; Mean velocity, $m/s$
$U$	Mean velocity in the $x$ coordinate direction, $m/s$
$e$	Specific internal energy, $J/kg$
$x, y, z$	Cartesian coordinates, $m$
$\mu$	Magnetic permeability, $H/m$ ( $N/A^2$ )
$\varepsilon$	Electrical permittivity, $F/m$ ( $C^2/(N \ m^2)$ )
$\chi_e$	Electrical susceptibility
$\chi_m$	Magnetic susceptibility
$\varepsilon_o$	Electrical permittivity of free space, $F/m$ ( $C^2/(N \ m^2)$ )
$\mu_o$	Magnetic permeability of free space, $H/m$ ( $N/A^2$ )
$t$	Time, $s$
$\epsilon$	Amplitude of a sinusoidal wave, $m$
$\alpha_v$	Volume coefficient of thermal expansion, $K^{-1}$



$c_p, c_v$	Specific heat capacity, $J/(g\ K)$
$\lambda$	Wavelength of a sinusoidal wave, $m$
$c$	Wave velocity, $m/s$
$p$	Pressure, $N/m^2$
$\rho$	Density, $kg/m^3$
$g$	Gravity, $m/s^2$
$M$	Mass, $kg$ ; Molar mass, $g/mol$
$\zeta$	Intermittency factor
$\Gamma$	Surface tension, $N/m$
$\gamma$	Ratio of specific heats, $c_p/c_v$
$\eta$	Absolute viscosity, $kg/(m\ s)$
$\nu$	Kinematic viscosity, $\eta/\rho$ , $m^2/s$
$\sigma$	Electrical conductivity, $S/m$ ; Standard deviation
$L$	Characteristic length; Pipe length, $m$
$\tau$	Joule damping term
$I_T$	Initial intensity of light, $cd$
$I_o$	Intensity of light, $cd$
$\omega$	Vorticity, $s^{-1}$
$\psi$	Stream function, $m^2/s$
$\phi$	Velocity potential, $m^2/s$
$\phi_E$	Electric potential, $V$
$E_{dep}$	Energy deposition, $J/g$
$f$	Focal length, $m$ ; Force, $N$ ; Friction factor
$\tau$	Wall shear stress, $N/m^2$
$\xi$	free surface perturbation, $m$

$h$	Head loss, $m$
$K$	Loss coefficient; Bulk modulus, $N/m^2$
$A$	Cross sectional area, $m^2$
$e$	Surface roughness, $m$ ; Error, %
$a$	Radius of circular pipe, $m$
$d$	Diameter of circular pipe, $m$
$R$	Gas constant, $J/(K \text{ mol})$ ; Radius of curvature of the centerline of the elbow, $m$
$G$	Pressure ratio
$C$	Contraction coefficient; Discharge coefficient; Constant
$Q$	Flow rate, $m^3/s$
$\beta$	Ratio of diameter
$Re_m$	Magnetic Reynolds number
$Re$	Reynolds number
$Fr$	Froude number
$Al$	Alfven Number
$Ha$	Hartmann number
$We$	Weber number
$N$	Stuart number; Number of events
$\nabla \cdot$	Divergence operator
$\nabla \times$	Curl operator
$\times$	Cross product operator
$\cdot$	Inner product operator; Multiplication

### ***Superscripts***

'	Differentiation with respect to variable; Perturbation; Fluctuation
.	Differentiation with respect to time

### ***Subscripts***

$x, y, z$	Component values over the cartesian coordinates
$o$	Component mean value
$R$	Reference location

# Chapter 1

## Introduction

Accelerator-based sources of exceptionally intense, tightly focused beams of x rays and ultraviolet radiation make possible both basic and applied research in fields from physics to biology to technology that are not possible with more conventional equipment. The development of a high-intensity source of muons can be useful for the production of high-energy neutrino, thereby opening the door for a broad range of important new physics experiments such as neutrino oscillation. The concept is to use a high-intensity proton beam incident on a mercury jet to produce pions which decay to give the muons. These muons are magnetically captured, accelerated, and then inserted into a storage ring.

### **1.1 Neutrino Factory For High Power Neutrino Beam**

#### **1.1.1 The concept of neutrino factory**

Accelerators are used to accelerate primary particle beams such as protons and electrons. The required statistics in the collision processes demand a very

high flux of primary particles. On interaction of the primary particles with a target, it is possible to produce secondary beams of elementary particles like pions, neutrons, and gammas. Primary protons pass through a linear accelerator and further through a synchrotron, bunch compressors, and accumulators to achieve a beam with a certain energy, intensity and beam structure. This beam is directed toward a target. On interaction with the target, secondary particles of different kinds are produced. A neutrino factory is the ultimate tool for producing a high-intensity neutrino beam to study neutrino oscillations. The neutrino factory is based on a new concept of an accelerator that produces a high-intensity, high-energy beam of muon and electron neutrinos. It will allow an investigation of a new domain in neutrino physics such as

- High intensity. Its flux is  $10^3$  times greater than conventional neutrino beams.
- High energy. It features a very high beam energy of 20 to 50 GeV.
- In a neutrino factory, the muon sign can be selected. Thus, it is possible to deliver particles and anti-particles.

The basic concept of the Neutrino Factory is the production of muon neutrinos and anti-electron neutrinos from the decay of muons that are circulating in a storage ring. An intense proton beam is delivered to a target, where pions are produced. These pions are collected in a solenoidal magnetic field, which can capture both charged states of pions. The pions decay into muons in a decay channel. The muon beam has both a large energy spread and transverse

emittance. The energy spread is reduced using a phase rotation, while emittance is improved by ionization cooling. The cooled beam is accelerated (in a linac followed by two recirculating linacs) to energies of 20 to 50 GeV and injected into a storage ring.

### 1.1.2 Neutrino physics

Muons are a promising source of neutrinos. They have a short lifetime of  $2.2\mu s$ . Muons cannot be produced directly, so pions have to be produced first. The first stage of a neutrino factory is thus a high-power proton driver that deliver protons onto a target, where pions are produced. These pions have to be collected and transported. After about 20m, most of the pions decay into muons. A neutrino beam can be produced from the decay of high-energy muons:

- Pions from  $Proton + Material \longrightarrow \pi^\pm + X$
- Muons from  $\pi^\pm \longrightarrow \mu^\pm \nu_\mu (\bar{\nu}_\mu)$
- Neutrinos from  $\mu^\pm \longrightarrow e^\pm \bar{\nu}_\mu \nu_e (\nu_\mu \bar{\nu}_e)$

At this stage, the muon beam has a low phase space density and resembles more a cloud than a beam. The next step is to create a usable muon beam. Phase rotation as well as ionization cooling is applied to reduce the energy spread and the emittance of the muon beam. Once the beam is cooled, it can be accelerated to a final energy of 20 to 50 GeV. In the final stage of a

neutrino factory, the accelerated muons are injected into a storage ring with long straight sections.

## **1.2 A High Power Target For Neutrino Factory**

### **1.2.1 Material consideration for a high power target**

The intensity of the muon beam is directly proportional to the power of the proton beam which initiates the process. Considering that a high intensity proton beam is required in order to generate the required muons, the choice of the target material becomes a particularly important issue. Modeling studies (Osaki, Palmer, Zisman, Gallardo, 2001) point to high-Z materials being more efficient at producing pions of both signs, whereas low-Z materials are better at preventing the absorption of the produced pions. The pion yield per proton increases with the atomic number of the target, as shown in Fig. 1.1 from a MARS calculation. A high-Z material is desirable because the pion production cross-section increases with increasing Z. However, the intense proton beam would melt a target made of a solid high-Z material. A target system using a flowing stream of mercury could recycle the spent target. Several types of target material have been proposed including copper, graphite, and mercury.

Since these targets are envisaged as being stationary, one must consider the problem of removing the energy deposited by the beam without interfering with the production of the particles.

### 1.2.2 Moving metallic target for pion production

While schemes for moving solid targets can be envisaged (Thieberger, Kirk, Weggel, McDonald, 2003), a flowing liquid target is simpler, and mercury as a high Z material presents itself as the liquid metal. The liquid target should be in the form of a free jet, rather than being confined in containment, since the beam-induced cavitation of the liquid metal can be destructive to solid walls in the immediate vicinity of the interaction region. Another issue associated with the proton beam is the effect of the energy that it deposits in the target. The temperature of the target rises almost instantaneously after the beam pulse, resulting in large internal stresses that might crack a solid target or disperse a liquid target (Kirk *et al*, 2001). In the case of a liquid jet target, the dispersal of the jet by the beam should not be destructive to the surrounding target system components and should not adversely affect pion production during subsequent beam pulses, either on the microsecond scale, if several micro-pulses are extracted from a proton synchrotron, or on the scale of the macro-pulse period. The operation of a liquid metal jet inside a strong magnetic field raises several magnetohydrodynamic issues such as possible deformation of the jet's shape and trajectory, as well as the effect of the magnetic field on the beam-induced dispersal of the jet.



### 1.2.3 Free mercury jet flow in magnetic field for a high power target

The free mercury jet in magnetic field is proposed for a high power target to overcome the issues described in the above chapter. The concept is to use a high intensity proton beam incident on a Hg jet to produce pions which decay to give the muons (Gabriel *et al*, 2001). The key elements of the target system are an intense proton source, mercury jet, and capture of the generated pions in a high field solenoidal magnet (McDonald, 2001). The schematics of the key elements of the target system is described in Fig. 1.3.

Previous studies (Osaki, Palmer, Zisman, Gallaro, 2001) indicated that pion yield is maximized with a mercury target in the form of a 1 cm diameter at the interacting center, tilted by about 150 milliradian with respect to the magnetic axis. The target is tilted with respect to the axis of the capture solenoid, thus permitting the pions, whose trajectories are spirals, to leave the side of the target with a minimal probability for re-entering the target volume. The pion yield per proton increases with the atomic number of the target, as shown in Fig. 1.1 from a MARS calculation. For 24 GeV protons, a high-Z target is superior in yield. As the pions emerge from the target at large angles to the beam, and follow helical paths that may intersect the target at more than one point, it is advantageous for the target to be in the form of a narrow rod, tilted at a small angle to the magnetic axis. As shown in Fig. 1.2, suitable parameters for a mercury target are a tilt angle of 150 mrad and a target radius of 5 mm.

Based on the previous studies described in the above, the experimental setup parameters are determined. The layout of experimental setup is briefly described in the below and will be more discussed in chapter 3. Fig. 1.4 shows the detailed schematic of the overlap between key components of the experiment. The trajectory of the mercury jet overlaps with the proton beam over 30 cm. The velocity of the jet is 15 m/s. The facility is a closed piping loop, constructed primarily of 316 stainless steel, and designed to circulate liquid mercury. The parameters of the proton beam and solenoid system are determined by the required conditions of particle production rates (Alessi *et al*, 1998). Basic system parameters consist of a proton energy 24 GeV, number of protons in one bunch  $\approx 3 \times 10^{13}$ . Only 10 % of the beam power is absorbed inside the target. The solenoid has a length is 100 cm, inside radius is 7.5 cm, and a maximum magnetic field is 15 T. The solenoid magnet is tilted at 67 milliradian angle with respect to the beam. The beam arrives at an angle 34 milliradian with respect to the jet which has a radius  $\approx 0.5$  cm, as schematically shown in Fig. 1.4. The 24 GeV proton beam is directed on to the solenoid at 67 milliradian off the solenoid axis, so that most high momentum particles do not travel straight down the beam line (Gallardo *et al*, 2001). If there are no magnetic and gravitational effects on the mercury jet trajectory, the beam should enter at the bottom surface of Hg jet at Viewport 1, which is located at approximately 30 cm from the nozzle and the beam should exit on the top surface of Hg jet at Viewport 3, which is located at approximately 60 cm from the nozzle. The required jet velocity is determined by two conditions:

1), the need to replenish the target before the arrival of subsequent proton beam pulse, and 2), it should be high enough to overcome the deceleration force induced by Lorentz force (Hassanein, Kinkashbaev, 2001).

Initial tests involving the interaction of proton beams on mercury targets were performed at the Brookhaven Alternating Gradient Synchrotron (AGS) (Kirk *et al.*, 2001), and continued at the CERN ISOLDE facility (Lettry *et al.*, 2003). The BNL test featured a 24 GeV proton beam interacting with a free mercury jet with a nozzle diameter of 1 cm and a velocity of 2.5 m/s. The delivered proton bunch was focused to  $<1$  mm radius, resulting in a peak energy deposition of 80 J/g, delivering 24 GeV proton beam at 15 Hz (Tsoupas *et al.*, 2003). These initial tests did not have a magnetic field on the target. A parallel effort was undertaken to study the effects of high velocity mercury jets in the presence of high-magnetic fields, but with no proton beam.

#### **1.2.4 Impact of the MHD mercury jet experiment for an intense proton target**

The previous experiments did not perform the mercury jet in a high magnetic field interacting with an intense proton beam. In this work, we integrated the mercury jet, solenoid magnet, and intense proton beam all together. The performance and feasibility of utilizing liquid metal jet as a target for an intense proton beam is explored experimentally, which is the explicit objective of the experiment. The liquid jet target concept is recyclability otherwise the target would be destroyed. Therefore, the power of the target has to be eval-

uated in terms of the replacing capability and validated experimentally. In order to validate the performance of the target, the MHD jet behavior in a strong magnetic field has to be investigated. The response of the mercury jet due to the energy deposition by interacting with an intense proton beam has to be studied and the magnetic field effect to the disruption of mercury jet has to be studied, as well. The experimental results reveals that the effect of the Lorentz force to the jet stabilization as well as the deflection of jet. The experimental results will provide feasibility of utilizing liquid metal jet as a target for an intense proton beam. Also, the results will validate the phenomenology of conduction flow in magnetic field based on the MHD theory.

## **1.3 Mercury Target Issues**

### **1.3.1 Mercury jet disruption by energy deposition from an intense proton beam**

The production of large fluxes of particles using high energy, high intensity proton pulses impinging on solid or liquid targets presents unique problems which have not yet been entirely solved. The large amount of power deposition required in the material coupled with the short pulse duration produce large, almost instantaneous local heating. The resulting sudden thermal expansion can result in damage causing stresses in solids and in the violent disruption of liquid jets. The volume expansion initiates vibrations in the material. The amplitude of these vibrations is such that stresses that exceed the strength of the material can be generated, causing mechanical failure (Thieberger *et al*,

2003).

The interaction of the proton beam with the mercury target leads to very high heating rates in the target. When proton beam energy reaches approximately 100 kJ/pulse range, the heat from the beam could melt or crack a high-Z target.

### **1.3.2 Magnetohydrodynamic issues in mercury jet target**

Liquid metal jets are proposed as potential target candidates because the heat energy can be removed along with the moving liquid. There are three important problems that are associated with the use of liquid metal targets in these environments. First, as the liquid jet penetrates the magnetic field, perturbations in jet motion and deceleration may occur because of the large field gradients at the entrance and exit of the solenoid. Second, during the intense pulse of energy deposition in a short time, the resultant stress could break up the target. Third, the liquid jet can develop instabilities in the strong inhomogeneous magnetic field and after beam interaction, because of the jet break up induced by the energy deposition of beam. These instabilities can change the jet shape into one that is significantly less efficient for pion production (Hassanein, Kinkashbaev, 2001).

Mercury flow in a magnetic field experiences induced currents, which cause the jet to produce transverse forces normal to jet axis direction resulting deflection normal to jet axis (Gallardo *et al*, 2001). In addition, axial currents

are induced if the jet axis does not coincide with the magnetic field axis. These axial currents produce elliptical distortions of the mercury jet. Faraday's law can be used to obtain the azimuthal current density from changing the axial field in the local coordinate system of the Hg jet. The transverse component of the magnetic field normal to the jet axis also varies along the trajectory of the mercury jet. The axial current density can be related to the changing transverse component of the magnetic field normal to the jet axis. These axial currents produce a magnetic force. This force will be balanced by a restoring force from the surface tension of the mercury, and with the condition that the mercury is an incompressible liquid, will produce an elliptic deformation of the mercury jet.

### **1.3.3 Overview of experimental investigation of MHD flow and discussion**

A proof-of-principle experiment at the CERN Proton Synchrotron that combined a free mercury jet target with a 15T solenoid magnet and a 24 GeV primary proton beam was performed. The experiment validates the target concept for producing an intense secondary source of muons by showing the jet repetition rate to replace the disrupted target by the energy deposition from an intense proton beam. The PS runs in a harmonic-16 mode and can fill up to  $2 \times 10^{12}$  protons/bunch. The spot RMS size in experiment is approximately 1.5 mm. This allows up to  $30 \times 10^{12}$  protons per pulse on the mercury target, generating a peak energy deposition of 180 J/g. For this experiment, a high

magnetic field pulsed solenoid with a bore of 15 cm is designed. This magnet is capable of delivering a pulsed peak field of 15 T. which is cooled to 80 K by liquid nitrogen to reduce the resistance of its copper coils. The Hg jet delivery system generates a mercury jet from 1 cm diameter nozzle with velocities up to 15 m/s. The primary diagnostic of the beam-jet interaction is optical. A set of four view-ports along the interaction region is connected by imaging fiber-optic bundles to four high speed cameras.

Each pulse of the proton beam delivered to this system constitutes a separate experiment. About 360 beam pulses are utilized in a beam-on-demand mode at CERN. These pulses span a range of intensities and time intervals between the multiple extracted bunches per pulse. The magnet operates over a range of field strengths of 0 – 15 T.

In chapter 2, the full MHD governing equation using Maxwell's equations are presented. Various modeling of conducting flow in a magnetic field are formed, where the contribution of Lorentz force to the hydrodynamic equations is presented and discussed. The formulated and reviewed theory is introduced to explain and support the MHD experimental results.

In chapter 3, the detailed layout of experimental setup and its installation are presented. The design of each key components for the experiment such as nozzle, solenoid magnet and mercury loop system is presented. As a primary diagnostics, the scientific development of optical diagnostics employing the high speed cameras and infrared lasers to freeze the transient motion of mercury jet is presented and the performance of the scientific instrument as

well as the methodology to capture images are discussed in detail.

In chapter 4, MHD behaviors of the mercury jet in a magnetic field are discussed based on the observation from the experiments. Also, the characteristics of the mercury jet in a magnetic field interacting with an intense proton beam are presented. The key results to validate the feasibility of the High-Z liquid target is addressed based on the experimental measurements and the beam pulse structures.

To conclude the study, the concluding remark are presented and the discussion based on the MHD theory and the experimental results is summarized in chapter 5. The discrepancy and/or consistency between expecting results from MHD theory and the experimental results are discussed and explained to leave a room for a future study.

This program explores the full variety of beam/target conditions anticipated in the design of Neutrino Factories driven by proton synchrotron of 4 MW beam power.



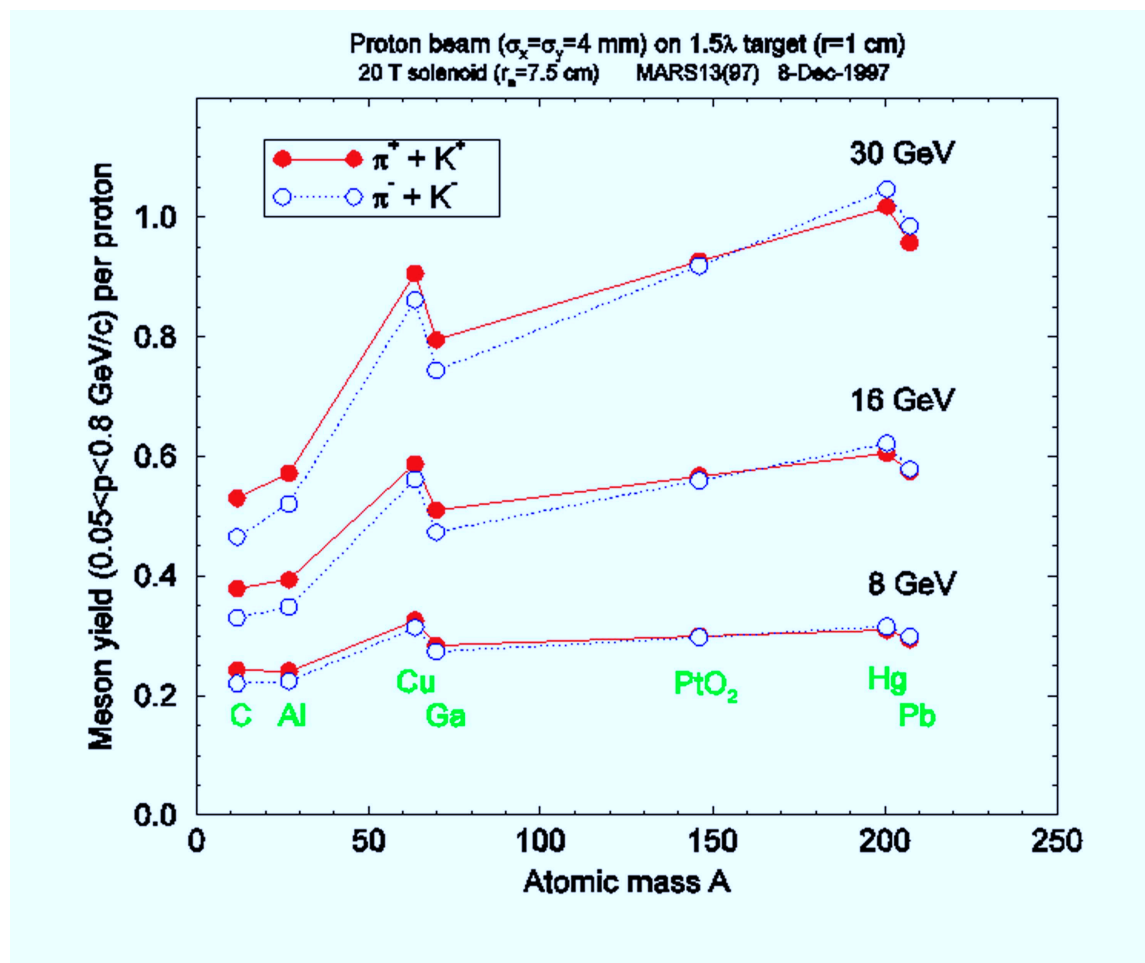


Figure 1.1: Pion yield versus atomic mass number of the target at three proton beam energies, Osaki (2001) and Mokhov (2000).

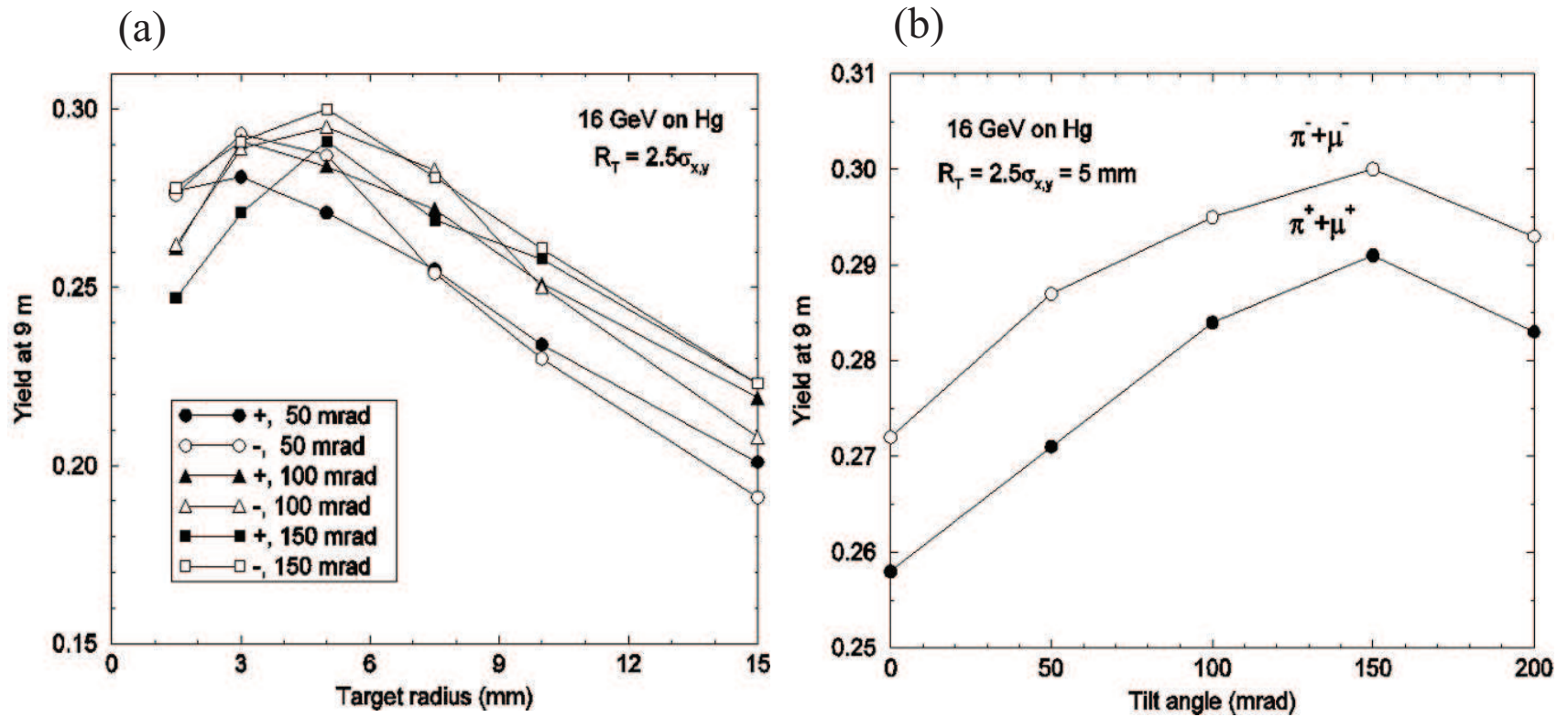


Figure 1.2: Pion yield from Hg targets versus tilt angle between the target/beam axis and the solenoid axis and versus the radius of the target, Osaki (2001) and Mokhov (2000). a.) Pion yield versus tilt angle. b.) Pion yield versus target radius.

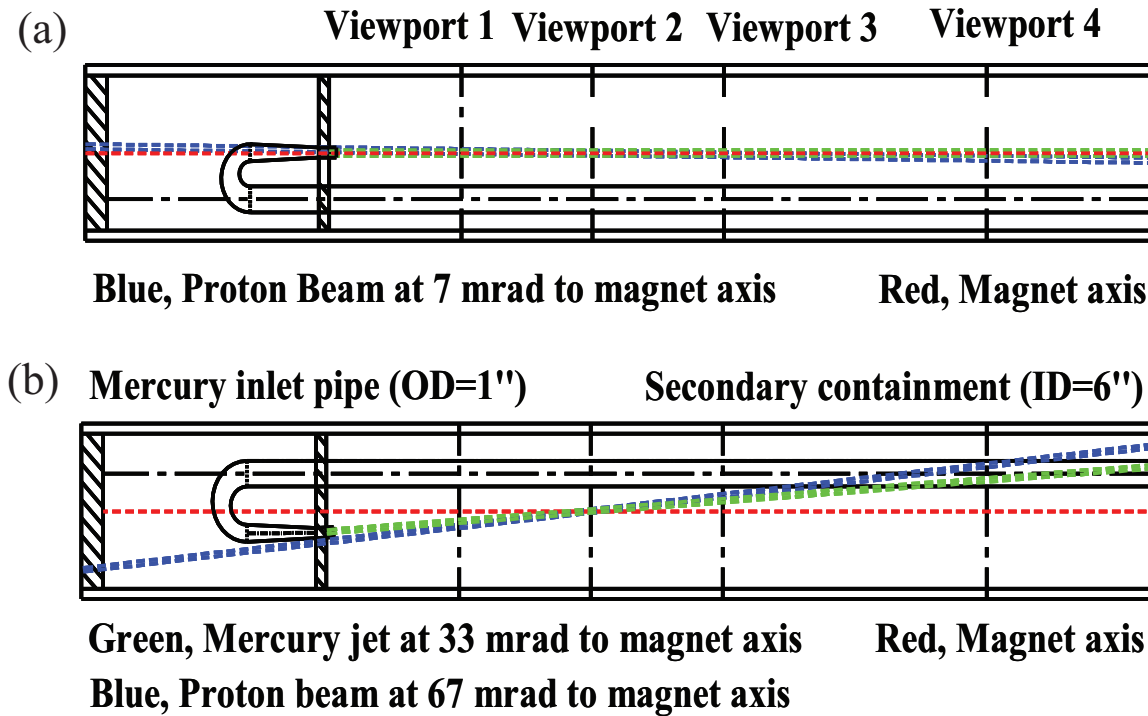


Figure 1.3: Geometry of key elements of target system and Viewports, showing the overlap between the mercury jet, magnetic axis, and the proton beam. a.) Top view. b.) Side view.

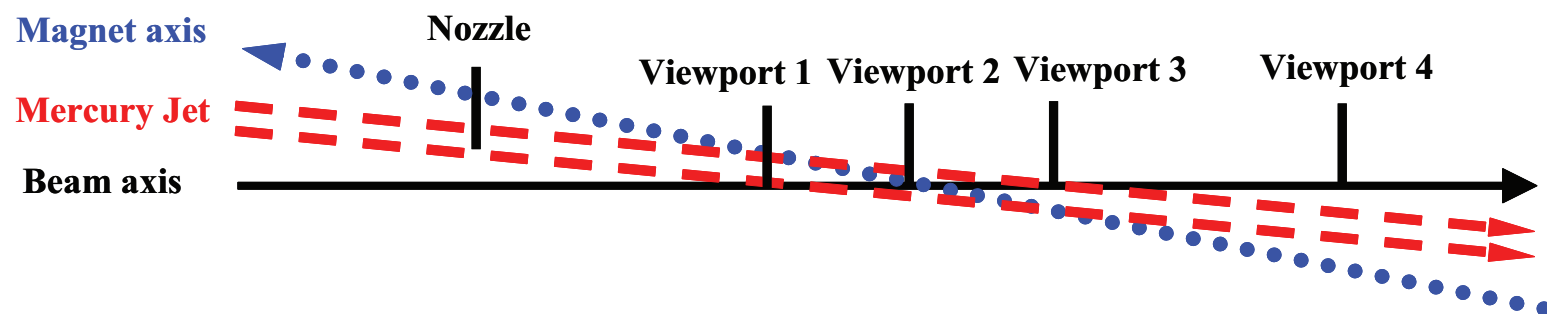


Figure 1.4: Schematics of the relative overlap between proton beam axis, Hg jet axis , and solenoid magnet axis.

## Chapter 2

# Magnetohydrodynamic Issues of Mercury Flow in Magnetic Field

In this chapter, the issues of electrically conducting fluid in a pipe and jet flow in a magnetic field are presented. The governing equations for magnetohydrodynamics, based on electrodynamic relations of Maxwell's equation and hydrodynamic Navier-Stokes equation, are given and the effects of Lorentz force induced by magnetic field are discussed. The review of previous work provides a basis for these studies. Hartmann (1937) considered the flow between two parallel, infinite, non-conducting walls, with magnetic field applied normal to the walls. An exact solution was obtained for this case by Hartmann (1937). Shercliff (1953) solved the more general problem of three dimensional flow in a rectangular duct. Exact solutions demonstrated the fact that for large Hartmann number, the velocity distribution consists of a uniform core with a boundary layer near the walls. This result enabled the solution of the corresponding problem for a circular pipe in an approximate manner for large Hartmann numbers, assuming walls of zero conductivities (Shercliff, 1956).

Chang and Lundgren (1961) considered the effects of wall conductivity for the same problem. Gold (1962) considered a steady one-dimensional flow of an incompressible, viscous, electrically conducting fluid through a circular pipe in the presence of a uniform transverse field. A no-slip condition on the velocity is assumed at the electrically non-conducting wall because if the walls are conducting, there is an electromagnetic force on the wall and a corresponding force on the fluid. The flow is along the  $z$ -axis, which coincides with the axis of the cylinder, and the uniform applied magnetic field is along the  $x$ -axis, which is normal to the flow direction. The solution is exact and valid for all values of the Hartmann number. The conducting liquid jet inside a strong magnetic field raises several magnetohydrodynamic (MHD) issues, such as the possible deformation of the jet's shape and trajectory, as well as the effect of the magnetic field on the beam-induced dispersal of the jet. The electrically conducting flow moving in a magnetic field experiences induced currents (Gallardo, 2002). These induced currents cause the jet to experience anisotropic pressure distribution with respect to the major and minor axis of jet cross section normal to the jet flowing axis while the jet penetrates the nonuniform magnetic field (Gallardo, 2002). In addition, axial currents are induced if the jet axis does not coincide with the magnetic field axis. These currents in turn produce transverse elliptical distortions of the mercury jet. Finally, the liquid jet can develop surface instabilities such as surface wavelength growing and jet breakup during both liquid motion in an inhomogeneous magnetic field and after the interaction of an intense proton beam, because of the Rayleigh instabilities

in a magnetic field and the sudden energy deposition leading to jet breakup. These instabilities can change the jet shape into a significantly less efficient target for pion production. The analytical approach to describe the behaviors of MHD conducting flow in a magnetic field is provided in this chapter.

## 2.1 Governing Equations for MHD Flow

### 2.1.1 Electromagnetic equations

In this section, we describe the electromagnetic relations that have been used in the derivation of the MHD governing equations. The following properties are defined as follows:

- polarization density  $\mathbf{P}$ : the vector field that expresses the density of permanent or induced electric dipole moments in a dielectric material. It is defined as the dipole moment per unit volume.
- magnetization density  $\mathbf{M}$ : the magnetic dipole moment per unit volume.
- electrical susceptibility  $\chi_e$ : a measure of how easily a dielectric material polarizes in response to an electric field. This determines the electric permittivity of the material. It is defined as the constant of proportionality when relating an electric field  $\mathbf{E}$  to the induced dielectric polarization density  $\mathbf{P}$ .
- magnetic susceptibility  $\chi_m$ : the degree of magnetization of a material in response to an applied magnetic field.

- electric displacement field **D**: It accounts for the effects of bound charges within materials. It is the macroscopic field average of electric fields from charged particles that make up otherwise electrically neutral material. It can be considered the field after taking into account the response of a medium to an external field such as reorientation of electric dipoles.
- magnetic field strength **H**: A vector field that permeates space and which can exert a magnetic force on moving electric charge and on magnetic dipoles such as permanent magnets.
- electric field **E**: the electric force per unit charge. The direction of the field is taken to be the direction of the force it would exert on a positive test charge.

#### 2.1.1.1 *electromagnetic relation in a linear material*

In a linear material, the polarization density **P** and magnetization density **M** are given by

$$\mathbf{P} = \chi_e \varepsilon_0 \mathbf{E} , \quad (2.1)$$

$$\mathbf{M} = \chi_m \mathbf{H} , \quad (2.2)$$

where  $\chi_e$  is the electrical susceptibility and  $\chi_m$  is the magnetic susceptibility of the material. Electric displacement field, **D**, and magnetic induction field, **B**, are related to electric field, **E**, and magnetic field **H** by

$$\mathbf{D} = \varepsilon_0 \mathbf{E} + \mathbf{P} = \varepsilon \mathbf{E} , \quad (2.3)$$



$$\mathbf{B} = \mu_o(\mathbf{H} + \mathbf{M}) = \mu\mathbf{H} , \quad (2.4)$$

where  $\varepsilon$  is the electrical permittivity and  $\mu$  is the magnetic permeability of the material.

### 2.1.1.2 *Maxwell's equations*

The solenoidal condition for the magnetic induction, indicating that there are no magnetic monopoles, is given by

$$\nabla \cdot \mathbf{B} = 0 , \quad (2.5)$$

That is there are no sources and sinks for magnetic field lines.

Faraday's law of magnetic induction is given by

$$\nabla \times \mathbf{E} = -\partial\mathbf{B}/\partial t \quad (2.6)$$

showing that a spatially varying electric field can induce a magnetic field.

Charge conservation gives

$$\nabla \cdot \mathbf{E} = \rho^*/\varepsilon_o , \quad (2.7)$$

where  $\rho^* = \varepsilon_o(n^+ - n^-)$  is the charge density,  $n^+$  is the number of ions, and  $n^-$  is the number of electrons.

Ampère's law is given by

$$\nabla \times \mathbf{B} = \mu\mathbf{j} + \mu\varepsilon\partial\mathbf{E}/\partial t , \quad (2.8)$$

where the last term on the right hand side is the displacement current. Introducing the fundamental units of mass M, length L, velocity  $v$ , and time t,

we consider the dimensions of the displacement current in Eqn. (2.8). The dimensions of the magnetic field  $B$ , electric field  $E$ , and the speed of light  $c$  itself respectively are considered for simplicity.  $\nabla \times \mathbf{E} \sim \frac{E}{L}$ ,  $\frac{\partial \mathbf{B}}{\partial t} \sim \frac{B}{t}$  gives  $E = vB$ . From the speed of light,  $c = \frac{1}{\sqrt{\mu\varepsilon}}$ ,  $\mu\varepsilon\partial\mathbf{E}/\partial t = \frac{1}{c^2}\partial\mathbf{E}/\partial t \sim \frac{1}{c^2}\frac{E}{t} = \frac{v}{c^2}\frac{B}{t} = \frac{B}{L}\frac{v^2}{c^2}$ . Therefore, The displacement current in Ampère's law can be neglected if the flow velocity is much less than the speed of light.

By assuming the flow obeys charge neutrality,  $n^+ - n^- \ll n$ , where  $n$  is the total number density, the charge density in Eqn. (2.7) can be neglected.

Finally, Ohm's law without Hall effect is given by

$$\mathbf{j} = \sigma(\mathbf{E} + \mathbf{v} \times \mathbf{B}) . \quad (2.9)$$

This is the generalization of the relation between voltage and current in a moving conductor. It provides the link between the electromagnetic equations and the fluid equations.

The electric charge is conserved, which is given by Kirchhoff's law:

$$\nabla \cdot \mathbf{j} = 0 \quad (2.10)$$

### 2.1.2 The Navier Stokes and magnetic induction equations in a conducting liquid flow

The motion of an electrically conducting fluid in the presence of magnetic field obeys the equations of magnetohydrodynamics. The fluid is treated as a continuum and the classical results of fluid dynamics and electro-dynamics are combined in the derivation of the equations. The first equation is from mass

conservation:

$$\frac{\partial \rho}{\partial t} + \nabla \cdot (\rho \mathbf{v}) = 0 . \quad (2.11)$$

Next, Newton's second law of motion gives

$$\rho \frac{D\mathbf{v}}{Dt} = -\nabla p + \mathbf{F} , \quad (2.12)$$

where the external force  $\mathbf{F}$  consists of several terms, such as the Lorentz force, given by  $\mathbf{j} \times \mathbf{B}$ , the gravitational force  $\rho \mathbf{g}$ , and the viscous force. The viscous term is given by a kinematic viscosity of the form  $\rho \nu \nabla^2 \mathbf{v}$  for an incompressible flow. Thus, Eqns. (2.12) become

$$\rho \frac{\partial \mathbf{v}}{\partial t} + \rho (\mathbf{v} \cdot \nabla) \mathbf{v} = -\nabla p + \rho \mathbf{g} + \eta \nabla^2 \mathbf{v} + \mathbf{j} \times \mathbf{B} . \quad (2.13)$$

Note that the Lorentz force couples the fluid equations to the electromagnetic equations. Eqn. (2.13) can be reduced to a dimensionless form.

$$\frac{\partial \mathbf{v}}{\partial t} + \mathbf{v} \cdot \nabla \mathbf{v} = -\nabla p + \frac{\mathbf{g}}{\text{Fr}^2} + \frac{1}{\text{Re}} \nabla^2 \mathbf{v} + \text{Al} (\mathbf{j} \times \mathbf{B}) , \quad (2.14)$$

where  $\text{Fr} = v/\sqrt{gL}$ ,  $\text{Re} = \rho v L/\eta$ ,  $\text{Re}_m = \mu \sigma v L$ , and  $\text{Al} = B_o^2/\mu \rho v^2$  denote the Froude, Reynolds, magnetic Reynolds, and *Alfvén* numbers, respectively. The Hartmann number gives the ratio of magnetic forces to viscous forces. Thus, this number is the important parameter in cases where the inertial effects are small. On the other hand, the Stuart number gives the ratio of magnetic forces to inertial forces, Thus, this number is the important parameter where dealing with inviscid or turbulence. The Hartmann number  $\text{Ha}$  and Stuart number  $\text{N}$  are related through  $\text{Ha}^2 = \text{Re} \text{Re}_m \text{Al}$  and  $\text{N} = \text{Re}_m \text{Al}$ . Note that the ratio

of Hartmann number and Reynolds number represents a mixture parameters and involving viscous, magnetic, and inertial forces and can be thought of the square root of the product of the viscous and magnetic forces divided by the inertial forces.

We consider components of the magnetic induction field  $B_x, B_y, B_z$ . Note that the longitudinal magnetic field along the jet axis  $x$  and the transverse magnetic field normal to the jet axis are given by  $B_x = B_X \cos\theta - B_Y \sin\theta$ ,  $B_y = -B_X \sin\theta + B_Y \cos\theta$  respectively, where  $B_X$  is axial magnetic field and  $B_Y$  is radial magnetic field. Also note that the  $(x, y, z)$  coordinate system is related with the dynamics of jet dynamics and the  $(X, Y, Z)$  coordinate system is related with the magnetic field direction in solenoid. The nondimensionalized momentum equations in the  $(x, y, z)$  coordinate system in Fig. 2.1 is represented as Eqn. (2.15) using Ohm's equation.

$$\begin{aligned} \frac{\partial v_x}{\partial t} + v_x \cdot \nabla v_x &= -\nabla p + \frac{1}{\text{Re}} \nabla^2 v_x - \frac{\text{Ha}_y^2}{\text{Re}} v_x + \frac{\text{Ha}_x \text{Ha}_y}{\text{Re}} v_y, \\ \frac{\partial v_y}{\partial t} + v_y \cdot \nabla v_y &= -\nabla p + \frac{1}{\text{Re}} \nabla^2 v_y - \frac{\text{Ha}_x^2}{\text{Re}} v_y + \frac{\text{Ha}_x \text{Ha}_y}{\text{Re}} v_x, \\ \frac{\partial v_z}{\partial t} + v_z \cdot \nabla v_z &= -\nabla p + \frac{1}{\text{Re}} \nabla^2 v_z - \frac{\text{Ha}_x^2}{\text{Re}} v_z - \frac{\text{Ha}_y^2}{\text{Re}} v_z. \end{aligned} \quad (2.15)$$

In MHD, to eliminate the electric field  $\mathbf{E}$  and the electric current density  $\mathbf{j}$ , we use the Ampere's law and Ohm's law. Then, the Faraday's law gives the magnetic induction equation:

$$\frac{\partial \mathbf{B}}{\partial t} = \nabla \times (\mathbf{v} \times \mathbf{B}) - \frac{1}{\mu\sigma} \nabla \times \nabla \times \mathbf{B} = \nabla \times (\mathbf{v} \times \mathbf{B}) + \frac{1}{\mu\sigma} \nabla^2 \mathbf{B} \quad (2.16)$$

### 2.1.2.1 *magnetic Reynolds number*

In Eqn. (2.16), the dimension of the term on the left hand side is  $\frac{B}{t}$  and the second term on the right hand side is  $\frac{B}{\sigma\mu L^2}$ . Therefore,  $\sigma\mu \sim \frac{t}{L^2}$ . The magnetic induction equation can be reduced to a dimensionless form.

$$\frac{\partial \mathbf{B}}{\partial t} = \nabla \times (\mathbf{v} \times \mathbf{B}) + \sigma\mu Lv \nabla^2 \mathbf{B} , \quad (2.17)$$

where the quantity  $\sigma\mu Lv$  is a dimensionless number,  $\text{Re}_m$ , called the magnetic Reynolds number.  $\text{Re}_m$  is a measure of the size of the advection term,  $\nabla \times (\mathbf{v} \times \mathbf{B})$ , relative to the diffusion term,  $\sigma\mu Lv \nabla^2 \mathbf{B}$ . Reynolds number  $\text{Re}$  measures the extent to which a convective process prevails over a diffusive one. In viscous flow, the viscosity causes vorticity to diffuse in the face of convection and the Reynolds number measures the power of convection over diffusion of vorticity. In MHD, the conductivity causes convection to overcome diffusion of the magnetic field to a degree measured by the magnetic Reynolds number  $\text{Re}_m$ . If  $\text{Re}_m$  is large, convection dominates over diffusion and magnetic boundary layer near the fields are to be expected. The magnetic Prandtl number measures the ratio of viscous diffusivity and magnetic diffusivity and is defined as  $\text{Re}_m/\text{Re}$ . When it is small, magnetic fields diffuse much more rapidly than vorticity and magnetic boundary layers are much thicker than viscous layers. This makes for simplifications such as the neglect of viscosity in the magnetic boundary layer.

In any region of length scale  $\delta$  where convection and diffusion are equally important,  $\delta$  must be of order  $1/\mu\sigma v$ . Only within limited regions where  $B$

changes significantly in a distance  $\delta$  can the gradients be high enough for diffusion and dissipation to matter. The characteristic time in the flow is the transit time  $L/v$ , during which a field disturbance diffuses a distance of order  $(L/\mu\sigma v)^{1/2}$ . This is much less than  $L$  if  $\text{Re}_m \gg 1$ , in which case diffusion is negligible. It will diffuse a distance of order  $(t/\mu\sigma)^{1/2}$ , which is negligible in comparison with the length scale  $L$  if  $L^2\mu\sigma/t \gg 1$ . This is the required criterion for the perfect conductivity approximation to be valid. At the other extreme case where diffusion is dominant is that the medium diffuses to the form it would be in stationary fluid, where no induced magnetic field would occur. The ratio of the induced magnetic field and the imposed magnetic field is of order  $\mu\sigma vL$ , which is  $\text{Re}_m$ . The low  $\text{Re}_m$  approximation is to ignore the induced field, to replace  $\mathbf{B}$  by the known field  $\mathbf{B}_o$  in all MHD equations.

### 2.1.2.2 *frozen-in theorem in magnetic induction equation*

If  $\text{Re}_m \gg 1$ , the induction equation Eqn. (2.16) is approximated by

$$\frac{\partial \mathbf{B}}{\partial t} = \nabla \times (\mathbf{v} \times \mathbf{B}) \quad (2.18)$$

The timescale with changes due to the fluid motion from Eqn. (2.18) is given by  $t_{\text{motion}} \sim \frac{L}{v}$ . In the case  $t_{\text{motion}} \ll t_{\text{diffusion}}$ , which corresponds to  $\text{Re}_m \gg 1$ , the diffusion term is negligible. According to the frozen-flux theorem of Alfvén, in a perfectly conducting fluid, where  $\text{Re}_m \rightarrow \infty$ , the magnetic field lines move with the fluid: the field lines are ‘frozen’ into the fluid. This theorem states that motions along the field lines do not change the field but motions transverse to the field carry the field with them. If the area of the flux tube

is small, the field strength will be approximately constant across the area of the tube. Thus, the  $|\mathbf{B}| \times \text{cross sectional area}$  is constant so that the field strength becomes stronger if the cross sectional area is reduced by the fluid motion. The vorticity flux through any loop moving with the fluid is constant and the particles which initially lied on a vorticity line continue to do so. All the fluid particles which initially lie on a magnetic field line continue to do so in a perfect conductor.

### 2.1.2.3 *the diffusion limit in induction equation*

If  $\text{Re}_m \ll 1$ , the induction equation Eqn. (2.16) is approximated by

$$\frac{\partial \mathbf{B}}{\partial t} = \frac{1}{\mu\sigma} \nabla^2 \mathbf{B} \quad (2.19)$$

The timescale with changes due to field diffusion from Eqn. (2.19) is given by  $t_{diffusion} \approx \sigma \mu L^2$ . The diffusion equation indicates that any irregularities in an initial magnetic field will diffuse away and be smoothed out. The field will tend to be a simpler uniform field. This process of smoothing out will occur on the given diffusion timescale.

## 2.2 The Energy Equation in MHD

In general, the energy equation can be written in the form

$$\frac{\rho^\gamma}{\gamma - 1} \frac{D}{Dt} \left( \frac{p}{\rho^\gamma} \right) = -\mathbf{D} \ , \quad (2.20)$$

where  $\mathbf{D}$  is the total energy loss function,  $\gamma$  is the ratio of specific heats,  $c_p/c_v$ . The energy loss function consists of thermal conduction, radiation, and

heating. The heating consists of several terms, such as small scale magnetic wave heating, ohmic heating, and viscous heating. However, such losses (gains) can be neglected if the medium is either isentropic or adiabatic. There are cases where no energy is added to the flow and no energy losses occur. The adiabatic term can be represented as follows, using Eqn. (2.11):

$$\rho^\gamma \frac{D}{Dt} \left( \frac{p}{\rho^\gamma} \right) = \frac{\partial p}{\partial t} + \mathbf{v} \cdot \nabla p + \gamma p \nabla \cdot \mathbf{v} = -(\gamma - 1) \mathbf{D} \quad (2.21)$$

To close the system of equations, an equation of state is needed, which is taken as ideal gas law:

$$p = \frac{\rho}{M} RT, \quad (2.22)$$

where  $M$  is molar mass and  $R$  is the gas constant ( $8.3 \text{ J} \cdot \text{mol}^{-1} \text{K}^{-1}$ ).

### 2.2.1 Energetics and effects of Lorentz force

The energy equation that contains all the various types of energy, including kinetic energy, gravitational energy, the internal energy, and the magnetic energy is obtained using the MHD governing equations. The gravitational potential  $\Phi$  is defined by  $-\nabla\Phi = \mathbf{g}$ . The kinetic energy is obtained by multiplying Eqn. (2.11) by  $v^2/2$  and dotting Eqn. (2.12) with  $\mathbf{v}$ . The energy equation can then be written as

$$\frac{\partial}{\partial t} \left( \frac{1}{2} \rho v^2 \right) + \nabla \cdot \left( \frac{1}{2} \rho v^2 \mathbf{v} \right) = -\mathbf{v} \cdot \nabla p + \mathbf{v} \cdot (\mathbf{j} \times \mathbf{B}) - \mathbf{v} \cdot \rho \nabla \Phi + \mathbf{v} \cdot \eta \nabla^2 \mathbf{v}. \quad (2.23)$$

The gravitational term can be expressed as follows using Eqn. (2.11) and the fact that  $\partial\Phi/\partial t = 0$ .

$$\mathbf{v} \cdot \rho \nabla \Phi = \nabla \cdot (\rho \Phi \mathbf{v}) + \frac{\partial}{\partial t} (\rho \Phi). \quad (2.24)$$



Eqn. (2.24) gives the flux of the gravitational potential energy and the rate of change of gravitational potential energy in time. The Lorentz force term can be expressed as follows using Eqn. (2.9):

$$\mathbf{v} \cdot (\mathbf{j} \times \mathbf{B}) = -\mathbf{j} \cdot (\mathbf{v} \times \mathbf{B}) = -\frac{j^2}{\sigma} + \mathbf{j} \cdot \mathbf{E} . \quad (2.25)$$

Eqn. (2.25) is rearranged using Eqn. (2.6):

$$\mathbf{v} \cdot (\mathbf{j} \times \mathbf{B}) = -\frac{j^2}{\sigma} - \nabla \cdot \left( \frac{\mathbf{E} \times \mathbf{B}}{\mu} \right) - \frac{\partial}{\partial t} \left( \frac{B^2}{2\mu} \right) . \quad (2.26)$$

The pressure gradient term gives

$$-\mathbf{v} \cdot \nabla p = -\nabla \cdot (p\mathbf{v}) + p\nabla \cdot \mathbf{v} . \quad (2.27)$$

Eqn. (2.27) can also be expressed as follows using Eqn. (2.21):

$$p\nabla \cdot \mathbf{v} = -\frac{\partial}{\partial t} \left( \frac{p}{\gamma - 1} \right) - \nabla \cdot \left( \frac{p}{\gamma - 1} \mathbf{v} \right) - \mathbf{D} . \quad (2.28)$$

Substituting the foregoing relations, the full energy equation can be expressed as

$$\frac{\partial}{\partial t} \left[ \frac{1}{2} \rho v^2 + \rho \Phi + \frac{p}{\gamma - 1} + \frac{B^2}{2\mu} \right] + \nabla \cdot \left\{ \left[ \frac{1}{2} \rho v^2 + \rho \Phi + \gamma \frac{p}{\gamma - 1} \right] \mathbf{v} + \frac{\mathbf{E} \times \mathbf{B}}{\mu} \right\} = -\frac{j^2}{\sigma} - \mathbf{D} . \quad (2.29)$$

This equation will be used later in this thesis.

## 2.2.2 Magnetic damping with joule dissipation

It is known that a static magnetic field can suppress motion of an electrically conducting liquid. If a conducting liquid moves through an imposed

static magnetic field, electric currents are generated. These, in turn, lead to ohmic heating such as Joule dissipation. As the thermal energy of the fluid rises, there is a corresponding drop in its kinetic energy, and so the fluid decelerates. This is to suppress the motion of liquid jets. In many applications, it is believed that the imposition of a static magnetic field is used as one means of suppressing unwanted motion. Considering the uniform perpendicularly imposed magnetic field to the flow direction for simplicity, the damping effect of Lorentz force can be quantified. If the magnetic field is uniform, the Faraday' law requires that  $\nabla \times \mathbf{E} = 0$ . Using Ohm's law and the fact that the current density is solenoidal, the current relationship is given by

$$\nabla \cdot \mathbf{J} = 0 \quad , \quad \nabla \times \mathbf{J} = \sigma \mathbf{B} \cdot \nabla \mathbf{v} . \quad (2.30)$$

Thus,  $\mathbf{J}$  is zero if  $\mathbf{v}$  is independent of the magnetic field direction. By doing cross product of  $\mathbf{J}$  and  $\mathbf{B}$  and using the vector identity, Lorentz force per unit mass is given by

$$\mathbf{F} = -\frac{\mathbf{v}}{\tau} + \frac{\sigma(\mathbf{B} \times \nabla \phi_E)}{\rho} , \quad (2.31)$$

where  $\tau = \rho/\sigma B^2$  is Joule damping term and  $\phi_E$  is electrical potential, which is given by the divergence of Ohm's law:  $\phi_E = \nabla^{-2}(B \cdot \omega)$ . The Lorentz force then simplifies to  $-\mathbf{v}/\tau$  when the magnetic field and the vorticity field are mutually perpendicular. Thus, the perpendicular  $\mathbf{v}$  to magnetic field declines on a time scale of  $\tau$ , which clearly explains the mechanism of magnetic damping. The ratio of the damping time  $\tau$  to the characteristic time  $L/v$  gives the interaction parameter  $N = \sigma B^2 L / \rho v$ , which is also used for the indication of the ratio of the magnetic and inertial forces.

To investigate the role of Joule dissipation, consider the fully derived energy equation in inviscid flow.

$$\frac{dE}{dt} = -\frac{1}{\sigma\rho} \int \mathbf{J}^2 dV = -\mathbf{D} , \quad (2.32)$$

where  $\mathbf{D}$  is joule dissipation and  $E$  is global kinetic energy.

$\mathbf{J}^2$  from Eqn. (2.30) was estimated (Davidson, 1999) and is given.

$$\frac{dE}{dt} \sim -\left(\frac{L_{min}}{L_{\parallel}}\right)^2 \frac{E}{\tau} , \quad (2.33)$$

from which

$$E \sim E_o \exp\left(-\tau^{-1} \int_0^t (L_{min}/L_{\parallel})^2 dt\right) , \quad (2.34)$$

where  $L_{\parallel}$  is the characteristic length for the flow, parallel to the magnetic field. It indicates that the flow decays on a time scale of  $\tau$  provided that  $L_{min}$  and  $L_{\parallel}$  are of the same order. However, the Lorentz force can not create or destroy linear (angular) momentum despite the Joule dissipation. This indicates that the flow can not be decayed on a time scale of  $\tau$  and the Eqn. (2.33) and (2.34) infer that  $L_{min}/L_{\parallel}$  must increase with time. Therefore, it is expected that these flow will experience anisotropy, with  $L_{\parallel}$  increasing as the flow evolves.

## 2.3 Vorticity Equations in MHD flow

The possibility of using an electromagnetic field for vortices control in conducting fluids needs to be investigated. Electromagnetic force can influence the stability of a flow, thus prevents its transition to turbulence by suppressing disturbances or changing mean velocity profiles. A significant drag reduction

is possible when the surface boundary condition is modified to suppress the vortices. Transverse magnetic field does not reduce drag because the magnetic field increases the skin friction drag by directly altering the mean flow, so called Hartmann flow, even though turbulent fluctuations are significantly reduced. The longitudinal magnetic field does not directly interact with the mean flow although it can reduce turbulent fluctuations. Thus it is possible that the longitudinal magnetic field can result in drag reduction.

### 2.3.1 Governing equations for vorticity

It is useful to transform the governing equations in terms of vorticity transport. The equation for the vorticity  $\omega$  of an incompressible conducting fluid in MHD is

$$\begin{aligned} \frac{\partial \omega}{\partial t} + (\mathbf{v} \cdot \nabla) \omega - (\omega \cdot \nabla) \mathbf{v} \\ = \nu \nabla^2 \omega + \frac{1}{\rho} \nabla \times (\mathbf{j} \times \mathbf{B}) \\ = \nu \nabla^2 \omega + \frac{1}{\rho} \{ (\mathbf{B} \cdot \nabla) \mathbf{j} - (\mathbf{j} \cdot \nabla) \mathbf{B} \} . \end{aligned} \quad (2.35)$$

The term  $(\omega \cdot \nabla) \mathbf{v}$  in Eqn. (2.35) expresses the effect of stretching and turning vorticity lines. From the Faraday's law and  $\partial \mathbf{B} / \partial t = 0$ , the electric field in terms of an electric potential,  $\phi_E$ , is

$$\mathbf{E} = -\nabla \phi_E . \quad (2.36)$$

From the Ohm's law, Kirchhoff's law, and Eqn. (2.36), the electromagnetic equation can be simplified as Eqn. (2.38) using nondimensionalized Ohm's law

Eqn. (2.37).

$$\mathbf{j} = \text{Re}_m(-\nabla\phi_E + \mathbf{v} \times \mathbf{B}) . \quad (2.37)$$

$$\nabla^2\phi_E = \nabla \cdot (\mathbf{v} \times \mathbf{B}) . \quad (2.38)$$

The important parameter in vortices dynamics is the Stuart number  $N$  ( $= \text{Re}_m \text{Al} = \sigma \mathbf{B}^2 L / \rho v$ ), which is the ratio of the electromagnetic force to the inertial force. Therefore, one can fix the Reynolds number and change the Stuart number to see the effect of magnetic field over the vortices strength. The Hartmann numbers,  $\text{Ha} = \sqrt{\text{Re}N}$ , can be determined correspondingly. The Stuart number gives the ratio of  $\text{Ha}$  to  $\text{Re}$ . Thus, the Stuart number will indicate the stabilizing effect of magnetic field to the unique characteristic of transition to turbulence.

### 2.3.2 Vorticity suppression

The vorticity is suppressed by the magnetic field, transverse to the vorticity. The result is altered if the conductivity  $\sigma$  is nonuniform and varies with coordinates, in which case vorticity will be created. When a conducting liquid flows along a pipe with an axial magnetic field, there will be no magnetic effect if the motion is laminar, though the vorticity is perpendicular to the magnetic field, but if the flow is turbulent, adding the field damps the turbulence and reduces the Reynolds stresses and the frictional drag. Adding the field also raises the critical Reynolds number for instability of flow (Shercliff, 1965).

### 2.3.2.1 *spanwise magnetic field effect to vorticity suppression*

For a spanwise magnetic field,  $\mathbf{B} = (0, 0, B_z)$ , the corresponding Lorentz force,  $\mathbf{f} = (f_x, f_y, f_z)$  can be represented as follows.

$$\begin{aligned} f_x &= N\left(-\frac{\partial\phi_E}{\partial y}B_z - B_z^2v_x\right) , \\ f_y &= N\left(\frac{\partial\phi_E}{\partial x}B_z - B_z^2v_y\right) , \\ f_z &= 0 . \end{aligned} \tag{2.39}$$

Introducing the stream function  $\psi$ ,

$$\frac{\partial^2\psi}{\partial x^2} + \frac{\partial^2\psi}{\partial y^2} = -\omega_z , \tag{2.40}$$

where the spanwise vortex  $\omega_z = \partial v_y/\partial x - \partial v_x/\partial y$ . The Ohm's law Eqn. (2.38) yields

$$\frac{\partial^2\phi_E}{\partial x^2} + \frac{\partial^2\phi_E}{\partial y^2} = \omega_z , \tag{2.41}$$

where unity quantity of  $B_z$  is assumed.

From Eqn. (2.38) and (2.41),  $\phi_E = \psi + \text{const.}$  Correspondingly this relation yields  $\mathbf{f} = 0$ . Therefore, the spanwise vortex flow is not affected by the spanwise magnetic field (Lim, 1998). However, it can reduce turbulent fluctuations without directly interacting with the mean flow.

### 2.3.2.2 *longitudinal and transverse magnetic field effect to vorticity suppression*

For longitudinal and transverse magnetic field  $\mathbf{B} = (B_x, B_y, 0)$  in a two dimensional flow, Eqn. (2.38) yields  $\nabla^2\phi_E^2 = 0$  assuming that there is no

velocity ( $v_z$ ) onto the normal to the flow direction. The corresponding forces can be represented as follows:

$$\begin{aligned} f_x &= N(B_y \frac{\partial \phi_E}{\partial z} - B_y^2 v_x + B_x B_y v_y) , \\ f_y &= N(-B_x \frac{\partial \phi_E}{\partial z} - B_x^2 v_y + B_x B_y v_x) , \\ f_z &= N(-B_y \frac{\partial \phi_E}{\partial x} + B_x \frac{\partial \phi_E}{\partial y} - B_x^2 v_z - B_y^2 v_z) . \end{aligned} \quad (2.42)$$

The effect of the longitudinal and transverse magnetic field on the strength of spanwise vortices can be shown from the vorticity equation where additional vortices term  $\omega_{Lorentz} = \nabla \times \mathbf{f}$  caused by the Lorentz force has been added.

$$\begin{aligned} \frac{\partial \omega_z}{\partial t} + (\mathbf{v} \cdot \nabla) \omega_z &= (\omega_z \cdot \nabla) \mathbf{v} + \frac{1}{\text{Re}} \nabla^2 \omega_z + N \left( -B_x \frac{\partial^2 \phi_E}{\partial x \partial z} \right. \\ &\quad \left. - B_y \frac{\partial^2 \phi_E}{\partial y \partial z} + B_x B_y \left( \frac{\partial v_x}{\partial x} - \frac{\partial v_y}{\partial y} \right) - B_x^2 \frac{\partial v_y}{\partial x} + B_y^2 \frac{\partial v_x}{\partial y} \right) . \end{aligned} \quad (2.43)$$

If we consider the longitudinal magnetic field  $\mathbf{B} = (B_x, 0, 0)$  and the transverse magnetic field  $\mathbf{B} = (0, B_y, 0)$  independently, the corresponding force can be shown in Eqn. (2.44), Eqn. (2.45) respectively.

$$\begin{aligned} f_x &= 0 , \\ f_y &= N(-B_x \frac{\partial \phi_E}{\partial z} - B_x^2 v_y) , \\ f_z &= N(B_x \frac{\partial \phi_E}{\partial y} - B_x^2 v_z) . \end{aligned} \quad (2.44)$$

$$\begin{aligned} f_x &= N(B_y \frac{\partial \phi_E}{\partial z} - B_y^2 v_x) , \\ f_y &= 0 , \\ f_z &= N(-B_y \frac{\partial \phi_E}{\partial x} - B_y^2 v_z) . \end{aligned} \quad (2.45)$$

Eqns. (2.44) and (2.45) clearly show that the Lorentz force retards the local velocity. The vorticity equation is shown as Eqn. (2.46), Eqn. (2.47).

$$\frac{\partial \omega_z}{\partial t} + (\mathbf{v} \cdot \nabla) \omega_z = (\omega_z \cdot \nabla) \mathbf{v} + \frac{1}{\text{Re}} \nabla^2 \omega_z + N(-B_x \frac{\partial^2 \phi_E}{\partial x \partial z} - B_x^2 \frac{\partial v_y}{\partial x}) . \quad (2.46)$$

$$\frac{\partial \omega_z}{\partial t} + (\mathbf{v} \cdot \nabla) \omega_z = (\omega_z \cdot \nabla) \mathbf{v} + \frac{1}{\text{Re}} \nabla^2 \omega_z + N(-B_y \frac{\partial^2 \phi_E}{\partial y \partial z} + B_y^2 \frac{\partial v_x}{\partial y}) . \quad (2.47)$$

The Lorentz force is negatively correlated with the spanwise vorticity. Therefore, the Lorentz force induced by the longitudinal and transverse magnetic field reduces the strength of the spanwise vorticity effectively.

## 2.4 One Dimensional Pipe Flow in Transverse Magnetic Field

In one-dimensional problem, the governing equations and the boundary conditions are assumed that there is only one component of the velocity,  $v_z$ , and only one component of the induced magnetic field,  $\mathbf{B}_z$ , along with the applied field  $\mathbf{B}_o$ , so that the total velocity and magnetic fields are given by

$$\begin{aligned} v_r = v_\theta = 0, \quad v_z = v_z(r, \theta), \quad B_r = B_o \cos \theta, \\ B_\theta = -B_o \sin \theta, \quad B_z = B_z(r, \theta) . \end{aligned} \quad (2.48)$$

Substituting these expressions into Eqn. (2.13) using cylindrical coordinates, we obtain

$$p(r, \theta, z) = -(1/2\mu)B_z^2 + O_1 z + O_2, \quad \partial p / \partial z = O_1 = \text{constant} , \quad (2.49)$$



$$O_1 = \eta \left[ \frac{\partial^2 v_z}{\partial r^2} + \left(\frac{1}{r}\right) \frac{\partial v_z}{\partial r} + \left(\frac{1}{r^2}\right) \frac{\partial^2 v_z}{\partial \theta^2} \right] + \left(\frac{1}{r}\right) B_\theta \frac{\partial B_z}{\partial \theta} + B_r \frac{\partial B_z}{\partial r} , \quad (2.50)$$

where  $O_2$  is a constant.

Eqn. (2.5), Eqn. (2.11), Equation (2.48) are identically satisfied and Eqns. (2.16) become

$$\frac{1}{\mu\sigma} \left[ \frac{\partial}{\partial r} \left( r \frac{\partial B_z}{\partial r} \right) + \left(\frac{1}{r}\right) \frac{\partial^2 B_z}{\partial \theta^2} \right] + \left[ B_r \frac{\partial}{\partial r} (r v_z) + \frac{\partial}{\partial \theta} (v_z B_\theta) \right] = 0 . \quad (2.51)$$

#### 2.4.1 Non-dimensional form of the governing equations using cylindrical coordinates

The modified non-dimensional form of Navier-Stokes equations and the magnetic induction equations using cylindrical coordinates is expressed as follows:

$$\nabla^2 v_z - \left(\frac{\text{Ha}^2}{\text{Re}_m}\right) \left[ \left(\frac{\sin \theta}{r}\right) \frac{\partial B_z}{\partial \theta} - \cos \theta \frac{\partial B_z}{\partial r} \right] = O , \quad (2.52)$$

$$\nabla^2 B_z - \text{Re}_m \left[ \left(\frac{\sin \theta}{r}\right) \frac{\partial v_z}{\partial \theta} - \cos \theta \frac{\partial v_z}{\partial r} \right] = 0 , \quad (2.53)$$

where  $\nabla^2 \equiv \frac{\partial^2}{\partial r^2} + \left(\frac{1}{r}\right) \frac{\partial}{\partial r} + \left(\frac{1}{r^2}\right) \frac{\partial^2}{\partial \theta^2}$ ,  $\text{Ha} = B_o a (\sigma/\eta)^{1/2}$ ,  $\text{Re}_m = \sigma \mu v a$ , and  $O = O_1 a^2 / \nu \eta$ . Eqn. (2.52) and (2.53) apply to any general incompressible, steady magnetohydrodynamic duct flow. The restriction as to geometry and the conditions at the wall enters through the boundary conditions.

#### 2.4.1.1 *boundary conditions in pipe flow*

No fluid slip at the wall is given by

$$v_z(a, \theta) = 0 , \quad (2.54)$$

where  $a$  is the radius of the cylinder, while the assumption of non-conducting walls implies that (Shercliff, 1953)

$$B_z(a, \theta) = 0 . \quad (2.55)$$

We can also obtain the current density  $\mathbf{j}$  and the electric field  $\mathbf{E}$  from Ampere's and Ohm's laws:

$$j_r = \left(\frac{1}{r}\right) \frac{\partial B_z}{\partial \theta}, \quad j_\theta = -\frac{\partial B_z}{\partial r}, \quad j_z = 0 , \quad (2.56)$$

$$E_r = (1/\sigma)j_r + v_z B_\theta, \quad E_\theta = (1/\sigma)j_\theta - v_z B_r, \quad j_z = 0 . \quad (2.57)$$

#### 2.4.2 **Exact solutions of pipe flow in magnetic field**

Shercliff (1953) uncoupled the Eqn. (2.52) and (2.53) by a linear transformation. The boundary conditions could also be reduced by the transformation. The velocity and magnetic field distribution are obtained from the uncoupled equations (Gold, 1962):

$$\begin{aligned} v_z = & \frac{-Kv}{4\alpha} \left[ e^{-\alpha \frac{r}{a} \cos \theta} \sum_{n=0}^{\infty} \epsilon_n \frac{I'_n(\alpha)}{I_n(\alpha)} I_n\left(\alpha \frac{r}{a}\right) \cos n\theta \right. \\ & \left. + e^{\alpha \frac{r}{a} \cos \theta} \sum_{n=0}^{\infty} (-1)^n \epsilon_n \frac{I'_n(\alpha)}{I_n(\alpha)} I_n\left(\alpha \frac{r}{a}\right) \cos n\theta \right] , \end{aligned} \quad (2.58)$$

$$B_z = \frac{-\text{Re}_m K B_o}{8\alpha^2} [e^{-\alpha \frac{r}{a} \cos \theta} \sum_{n=0}^{\infty} \epsilon_n \frac{I'_n(\alpha)}{I_n(\alpha)} I_n(\alpha \frac{r}{a}) \cos n\theta - e^{\alpha \frac{r}{a} \cos \theta} \sum_{n=0}^{\infty} (-1)^n \epsilon_n \frac{I'_n(\alpha)}{I_n(\alpha)} I_n(\alpha \frac{r}{a}) \cos n\theta - 2 \frac{r}{a} \cos \theta] , \quad (2.59)$$

where  $\alpha = \frac{1}{2}\text{Ha}$ ,  $I_n$  is the modified Bessel function of order  $n$ ,  $\epsilon_n = 1$  for  $n=0$ , and  $\epsilon_n = 2$  for  $n>0$ . Equation (2.56) and (2.57) are used to obtain the electric field  $\mathbf{E}$ :

$$E_r = \left( \frac{a\mu v}{\text{Re}_m r} \right) \frac{\partial B_z}{\partial \theta} - v_z B_o \sin \theta . \quad (2.60)$$

$I_n$  identities are given by

$$I_n(\alpha) = I_{-n}(\alpha) , I_n(-\alpha) = (-1)^n I_n(\alpha) , I_n(\alpha)' = \frac{1}{2}(I_{n+1}(\alpha) + I_{n-1}(\alpha)) , \quad (2.61)$$

and

$$I_n(x) = \frac{1}{\pi} \int_0^\pi e^{x \cos \theta} \cos n\theta d\theta - \frac{1}{\pi} \int_0^\infty e^{-x \cosh u - nu} du . \quad (2.62)$$

## 2.5 Stability of Conducting Flow in a Magnetic Field

The problem of the flow of liquid metal jets in magnetic field arises in certain applications of magnetohydrodynamics. The stability of the flow of a conducting film in the presence of two components of the magnetic field (in the direction of the flow and normal to the surface) was investigated by B.A. Kolovadin (1965) using the approximation of small Reynolds numbers: The ratio of transverse magnetic field to longitudinal magnetic field changes due

to the finite inclination of jet axis to the magnetic field axis. The magnitude of the inclination angle affects the stability of the liquid jets.

These instabilities can change the jet shape into one that makes the jet a significantly less efficient target for particle production. As described in Chapter 1, the particle production depends on several parameters such as jet size and jet angle. Thus, the unstable behaviors of jet in a magnetic field yields less or unexpected production of particle. In addition, the larger inclination of jet axis makes the jet size become bigger than the nominal jet size due to the increased magnetic field. Thus, the mercury jet interacting with beam will have different energy deposition leading to different particle production. Therefore, the stable motion of mercury jet is required for stable particle production and it then needs to be investigated.

### **2.5.1 Propagation of waves at an interface separating two flows in magnetic field**

To investigate the surface wave motion of free jet in magnetic field, we followed the procedure of a direct extension of Currie (1993) to the case with a magnetic field. The detailed procedures and derivations are described in Appendix B.2.

We consider the  $(x, y, z)$  coordinate system in Fig. 2.1. The magnetic field along and normal to the Hg jet axis can be derived from the solenoid magnetic field map. From trigonometry, the longitudinal magnetic field along the jet axis and the transverse magnetic field normal to the jet axis are given by

$B_x = B_X \cos \theta - B_Y \sin \theta$ ,  $B_y = -B_X \sin \theta + B_Y \cos \theta$ , respectively, where  $B_X$  is the axial component of the magnetic field and  $B_Y$  is the radial component. To investigate the effect of sinusoidal wave perturbation at the interface, the equation of the interface is chosen to be  $\xi(x, t) = \epsilon e^{i(2\pi/\lambda)(x-ct)} + a$ , where  $\epsilon$  is the wave amplitude,  $\lambda$  is the wavelength, and  $c$  is the wave propagation speed. Small perturbations from the basic flow in the form  $v_{xi} = U_i + v'_{xi}$ ,  $v_{yi} = v'_{yi}$ ,  $p_i = P_i + p'_i$ ,  $v'_{xi} = \frac{\partial \phi_i}{\partial x}$ ,  $v'_{yi} = \frac{\partial \phi_i}{\partial y}$  are assumed, where  $\phi_i$  is the velocity potential for the perturbation to the uniform wavy flows at the interface. Substituting the perturbed expressions into the equations of motion, neglecting second order terms in the perturbed quantities, and making use of the fact that  $U$ ,  $P$  satisfy the flow equations and the current density in Lorentz force term can be represented using Ohm's law, we have the linearized equations governing the motion of disturbance, which yields the Rayleigh's stability equation of conducting flow in a magnetic field by replacing the perturbed quantities with the equation of motion. The Rayleigh's equation must be solved subject to the boundary conditions. The dynamic boundary condition at interface yields the effect of a magnetic field and the conditions of interfacing flows such as flow velocity and density to the wave velocity and wave number. Without a magnetic field, the quantity  $c$  has an imaginary part that results in the interfacial wave growing exponentially with time. Thus, the interface at the shear layer is unstable. However, the magnetic effects to the wave propagation velocity to reduce the wave amplitude and correspondingly the wavelength increases due to the magnetic field.

Several investigations have suggested that magnetic field suppresses turbulent fluctuations in conducting liquid by stabilizing the flow (Shercliff 1956, Gold 1962, Kozyrev 1981, Bernshtam 1982) and the stabilizing action of the longitudinal component of a magnetic field is considerably weaker than that of the transverse component, where stabilization is judged by an increase in the characteristic wavelength of the flow and  $\text{Re}_{cr}$ .

### 2.5.2 Magnetic pressure and tension

Once the jet surface is stabilized and flattened by a magnetic field, the magnetic pressure caused by the Lorentz force is contributing to the hydrodynamic pressure. It gives rise to deflect the jet in directions perpendicular to the magnetic field. Considering that the continuity condition has to be satisfied, the Lorentz force makes the jet shape change elliptically. Therefore, the contributions of each magnetic pressure components to the isotropic hydrodynamic pressure needs to be investigated.

Lorentz force is  $\mathbf{F} = \mathbf{J} \times \mathbf{B} = \frac{1}{\mu}(\nabla \times \mathbf{B}) \times \mathbf{B} = \frac{1}{\mu}(\mathbf{B} \cdot \nabla)\mathbf{B} - \frac{1}{2\mu}\nabla\mathbf{B}^2$ . Suppose the Maxwell stress tensor  $T_{ij} = \frac{1}{\mu}(B_{ij} - \frac{1}{2}\delta_{ij}B^2)$ , which represents the deviatoric stress tensor of magnetic field. The divergence of the Maxwell stress tensor is represented as follows, which gives the same expression with Lorentz force.

$$\begin{aligned} \nabla \cdot T &= \frac{1}{\mu} \begin{bmatrix} \frac{\partial}{\partial x} & \frac{\partial}{\partial y} & \frac{\partial}{\partial z} \end{bmatrix} \begin{bmatrix} \frac{B_x^2 - B_y^2 - B_z^2}{2} & B_x B_y & B_x B_z \\ B_y B_x & \frac{B_y^2 - B_x^2 - B_z^2}{2} & B_y B_z \\ B_z B_x & B_z B_y & \frac{B_z^2 - B_x^2 - B_y^2}{2} \end{bmatrix} \\ &= \frac{1}{\mu}((\mathbf{B} \cdot \nabla)\mathbf{B} + (\nabla \cdot \mathbf{B})\mathbf{B} - \nabla(\frac{\mathbf{B}^2}{2})) \end{aligned} \quad (2.63)$$

T has units of pressure. The shear is given by the off-diagonal elements of T and the diagonal elements of T correspond to the pressure acting on a differential area element. Total force on a volume is represented as follow.

$$F = \int \int \int_V \nabla \cdot T dV = \oint_S T \cdot dS \quad (2.64)$$

The conservation of momentum in inviscid flow is represented as follow.

$$\begin{aligned} & \frac{d}{dt} \int \int \int_V \rho \mathbf{v} dV + \oint_S \rho \mathbf{v} (\mathbf{v} \cdot \hat{n}) dS \\ &= - \oint_S p \hat{n} dS + \int \int \int_V \rho \mathbf{g} dV + \int \int \int_V \nabla \cdot T dV \end{aligned} \quad (2.65)$$

$$\frac{d\mathbf{v}}{dt} + (\mathbf{v} \cdot \nabla) \mathbf{v} = -\frac{1}{\rho} \nabla p + \mathbf{g} + \frac{1}{\rho} \nabla \cdot T = -\frac{1}{\rho} \nabla \mathbb{P} + \mathbf{g} \quad (2.66)$$

,where

$$\mathbb{P} = \begin{bmatrix} p - \frac{B_x^2 - B_y^2 - B_z^2}{2\mu} & -B_x B_y & -B_x B_z \\ -B_y B_x & p - \frac{B_y^2 - B_x^2 - B_z^2}{2\mu} & -B_y B_z \\ -B_z B_x & -B_z B_y & p - \frac{B_z^2 - B_x^2 - B_y^2}{2\mu} \end{bmatrix} \quad (2.67)$$

Note that the magnetic field increases the pressure by an amount  $\mathbf{B}^2/2\mu$ , in directions perpendicular to the magnetic field and decreases the pressure by the same amount in the parallel direction. Thus, the magnetic field gives rise to a magnetic pressure  $\mathbf{B}^2/2\mu$ , acting perpendicular to field lines, and a magnetic tension  $\mathbf{B}^2/2\mu$ , acting along field lines.

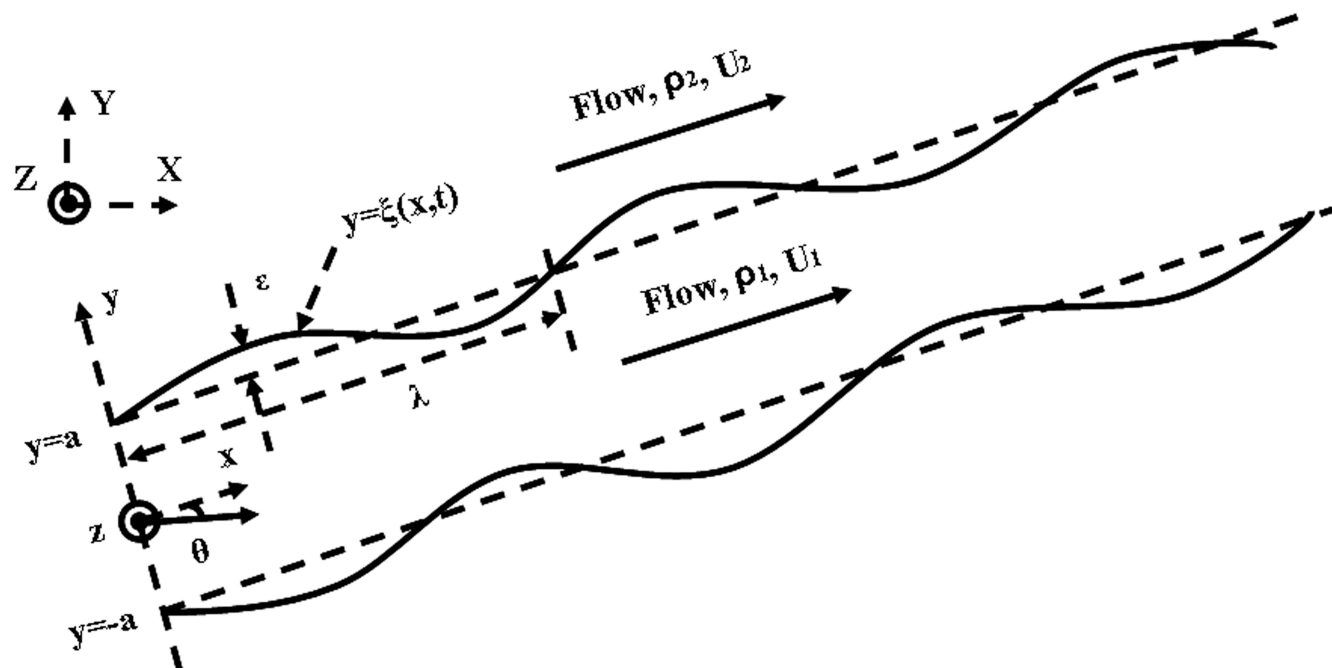


Figure 2.1: Wave-shaped interface separating two different fluids traveling at different average speeds.



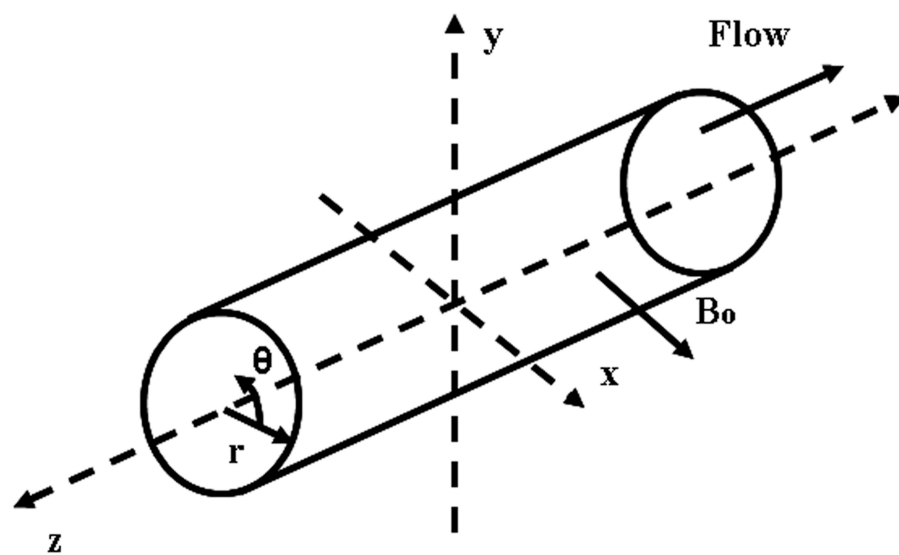


Figure 2.2: Axes and electrodes of circular duct.

## Chapter 3

# Experimental Method for Investigation of Magnetohydrodynamic Mercury Jet Flow

The optical method is considered to investigate MHD processes. Optical methods have considerable advantages over other measurement techniques: they do not introduce any perturbations into the medium being investigated, they possess high sensitivity and accuracy, their response is practically instantaneous, which enables them to be used to investigate turbulent flows and transition states, since they provide the possibility of visually following the phenomenon being investigated, and they enable one to obtain the physical characteristics for the whole space being investigated at the same instant of time. Unlike other probeless methods, optical methods possess high spatial resolution. All these features enable optical methods to be widely employed in MHD experiments and underlie the need to search for new ways of using modern optical methods which have not yet been employed.

Direct visualization techniques for hydrodynamic examination have often been employed to investigate the dynamics of MHD flows. In this method, one measures the time taken for the particles to traverse a given path. Because no quantitative results can be deduced from direct visualization methods and difficulties often arise when investigating thin boundary layers in liquids, attention has turned to the use of optical techniques for the investigations of fluid dynamics and MHD (Fedin, 1973).

It should be noted that visualization is usually employed for qualitative investigations, but this method can also be used to measure the average flow velocity and a change in the velocity profile. To do this one measures merely the time taken for the particles to traverse a given path or the path traversed in a given time.

## **3.1 Optical Diagnostics as a Principal Diagnostics of High Power Target Experiment**

### **3.1.1 Working principle of shadowgraph for optical diagnostics**

Optical measurements have many advantages over other techniques. The major one is the absence of an instrument probe that could influence the flow field. The light beam can also be considered as essentially inertialess, so that very rapid transient effects can be studied.

Shadowgraph is often employed in studying shock and flame phenomena,

in which very large density gradients are present. It integrates the quantity measured over the length of the light beam. For this reason they are well suited to measurements in two dimensional fields, where there is no index of refraction or density variation in the field along the light beam.

In a shadowgraph system the linear displacement of the perturbed light is measured. Consider the illumination at the exit of the test section. Figure 3.1 shows the displacement of a light beam for shadowgraph. If the illumination is uniform entering the test section, it should still be closely uniform there. The beam is deflected by an angle  $\alpha$ , which is a function of  $y$ . The illumination within the region defined by  $\Delta y$  at this position is within the region defined by  $\Delta y_{sc}$  at the screen. If the initial intensity of light is  $I_T$ , then at screen,

$$I_o = \frac{\Delta y}{\Delta y_{sc}} I_T . \quad (3.1)$$

If  $Z_{sc}$  is the distance to the screen, then the contrast is

$$\frac{\Delta I}{I_T} = \frac{I_o - I_T}{I_T} = \frac{\Delta y}{\Delta y_{sc}} - 1 \simeq -z_{sc} \frac{\partial \alpha}{\partial y} , \quad (3.2)$$

$$\frac{\Delta I}{I_T} = -\frac{z_{sc}}{n_a} \int \frac{\partial^2 n}{\partial y^2} dz = -\frac{z_{sc}}{n_a} \int \frac{\partial^2 \rho}{\partial y^2} \cdot \frac{\partial n}{\partial \rho} dz , \quad (3.3)$$

where  $n$  is the index of refraction of a homogeneous transparent medium and  $n_a \simeq 1$  for the ambient air.

For gas, Eqn. (3.4) could be substituted into Eqn. (3.3). Eqn. (3.3) is

integrated twice to determine the density distribution. (Goldstein, 1991)

$$\frac{\partial^2 n}{\partial y^2} = C \left[ -\frac{\rho}{T} \frac{\partial^2 T}{\partial y^2} + \frac{2\rho}{T^2} \left( \frac{\partial T}{\partial y} \right)^2 \right], \quad (3.4)$$

where the constant C, called the Gladstone-Dale constant, is a function of the particular gas and T is temperature of medium on Kelvin scale.

Shadowgraph is used principally for qualitative descriptions of a density field. Because it yields information on the first and second derivatives of density, its application can be found in systems with steep gradients of density and temperature, such as flame fronts and shock waves.

Optical techniques are non-invasive and do not cause any perturbation of the subject being investigated. Furthermore, their sensitivity increases with photon intensity and the resolution of the subject can reach the diffraction-limited resolution. The optical response of fluid dynamics and MHD are practically instantaneous, enabling the optical technique to study details of turbulent flows and transition states. Coupled to a state-of-the art high-speed camera and the long interaction path length of a light beam with a field of view adjustable to arbitrary dimensions, the optical technique enables one to obtain the physical characteristics for the entire subject being investigated in a short period of time.

### **3.1.2 Development of optical diagnostic system**

An optical diagnostic system is designed and constructed for imaging a free mercury jet interacting with a high intensity proton beam in a pulsed high-field solenoid magnet. The optical imaging system employs a back-illuminated,

laser shadow photography technique. Object illumination and image capture are transmitted through radiation-hard multi-mode optical fibers and flexible coherent imaging fibers. A retro-reflected illumination design allows the entire passive imaging system to fit inside the bore of the solenoid magnet. A sequence of synchronized short laser light pulses are used to freeze the transient events and the images are recorded by several high speed charge coupled devices.

#### **3.1.2.1 *the optical imaging system and viewports design***

Laser back-illuminated shadow photography technique is employed in experiment to capture the dynamics of the interaction of the proton beam with a moving free mercury jet. The design of the optical imaging system is based on a few essential criteria which are described below. The entire optical imaging head has to fit inside a small portion of a 1 meter long, 150 mm diameter bore magnet. Fig. 3.2(a), Fig. 3.2(b), and Fig. 3.2(c) show the conceptual back illuminated optics design, the installation of 4 viewports on the primary containment vessel, and the schematic layout of optical components, respectively.

Note that all optics placed inside the interaction beam tunnel are required to be radiation-hard because of high radiation levels in the beam tunnel and the activation of the mercury after proton beam interactions. In our setup, all cameras, lasers, and all other associated electronics are placed in an adjacent beam tunnel controlled locally by several desktop computers. Remote control of the entire system is achieved through designated control desktops located in the control room via MS Window XP remote desktop connections from the

ethernet network (see Fig. 3.6).

A viewport is located at the beam interaction center and two additional viewports are located at  $\pm 152.4$  mm up/down stream locations. Viewport 4 is positioned at  $+457.2$  mm and is designed to capture the residual dynamics of the proton interaction. Because of limited space inside the magnet bore, object illumination and image capture are transmitted through multi-mode optical fibers and coherent imaging fibers, respectively, all positioned on one side exterior to the primary containment vessel. Fig. 3.3 shows the fabricated and assembled optical head containing the integration of ball lens, imaging lens, illumination fiber, and imaging fiber.

The arrangement resembles a compact endoscope design but with a different illumination scheme. Illumination light pulses are coupled into a 15 meter long multi-mode fiber (ThorLabs BFL22-200). It has a numerical aperture of 0.22,  $25^\circ$  cone angle, with a core diameter of  $200\text{ }\mu\text{m}$  that matches that of the fiber-coupled lasers. To provide a  $\sim 55$  mm illumination area at the center of the primary containment vessel over a limited short working distance of  $< 100$  mm, the illumination cone angle has to be opened up to a  $43^\circ$  full cone angle. This is achieved by placing a tiny  $\sim 0.5$  mm diameter sapphire ball lens (Edmund Optics M46-117) at the tip of the illumination fiber and secured by a thin stainless steel plate. At the heart of the illumination arrangement is a 76 mm diameter Au-coated concave spherical retro-reflector that has a short radius of curvature of 124 mm (Rainbow Research Optics). When the much diverged illumination fiber is placed at the radius of curvature and shined

onto the optical axis of the reflector, a retro-reflected beam returns back to the illumination fiber providing the back-illumination scheme. Again, because of the tight environment inside the primary, a Au-coated  $90^\circ$  prism mirror turns the optical path from longitudinal to transverse onto the center of the primary. Two anti-reflection coated sapphire windows (Swiss Jewel Company) are mounted on the primary with airtight seals tested up to 1.4 bar pressure. The diameter and the thickness of the window is 100 mm and 6 mm respectively, sufficiently large enough for the observation of a 1 cm diameter jet and mechanically strong enough to withstand the momentum of a direct impact from mercury jet with a mean velocity of 20 m/s (Simos, 2005).

Based on this optical arrangement, a mercury jet in front of the reflector naturally makes a shadow on the retro-reflected beam. The shadow is collected by a 1 mm diameter AR-coated cylindrical grin objective lens (GrinTech, GT-IFRL-100-inf-50-CC) which has an optical path length of 2.43 mm. The grin lens is coupled onto a coherent image fiber. This flexible coherent imaging fiber is the key optical element of the imaging system. It is a 10 meter long Sumitomo IGN-08/30 fiber with 30,000 picture elements (pixels). Each individual fiber has a core diameter of  $\sim 4 \mu\text{m}$  with a total fiber diameter of merely 0.96 mm including coating. It has a bending radius of 40 mm, sufficiently small to allow curving and arching inside the primary containment vessel. All imaging fiber ends are hand polished in-house to optical finished quality to allow high quality images with maximum light intensity transmission. Fig. 3.4 shows the final finished end of an imaging fiber after polishing with  $0.3 \mu\text{m}$  lapping



film (ThorLabs, LFG03P). The surface quality and the flatness of the imaging fibers are inspected under a microscope. The imaging fibers are jacketed in-house with reinforced furcation tubing (ThorLab FT030-BK). One end of the imaging fiber is finished with an SMA 905 fiber-optics connector to facilitate coupling to a CCD camera. The other ends of the illumination and imaging fibers are positioned next to each other with  $\sim 2$  mm separation inserted inside a specially fabricated plastic ferrule. The integrated optical head is shown in Fig. 3.3, where a red laser diode is used to illuminate the optical head. The integrated all-in-one ferrule (ball lens, illumination fiber, objective lens, and imaging fiber bundle) is placed at the radius of curvature as well as on the optical axis of the reflector so that it allows both the illumination and the imaging collection to work on one side of the primary. The liquid mercury target is enclosed in a stainless steel primary containment vessel which is placed in the primary beam tunnel (TT2A). A total of four optical imaging heads for each viewport are mounted on the exterior of the primary, designated as channels 1 to 4. All fibers are routed through a  $\sim 150$  mm diameter, 2 meter long concrete passage to an adjacent beam tunnel (TT2), where radiation is much reduced. All electronics control for the optical diagnostic as well as all other electronics control for the solenoid magnet operation and hydraulic power unit used to generate the mercury jet are also placed in the adjacent tunnel. The exit end of each imaging fiber is coupled to an SMA fiber adaptor (ThorLabs SM1SMA) mounted on an x-y translator (ThorLab LM1XY). Four  $40\times$  infinitely corrected microscope objective (Newport M-40x) relay the  $\sim$

0.96 mm image outputs of each imaging fiber onto each corresponding CCD with appropriate lens tubes to fully expand the images onto a typical  $10 \times 10$  mm CCD array. A non-rotating adjustable lens tube zoom housing (ThorLabs SM1ZM) provides fine and accurate adjustment of image focus on CCD.

### **3.1.2.2 *the consideration for focusing and tilting alignment of optics***

A retro-reflective mirror captures the output beam of the laser diode and focuses it through the field of view at the target onto the lens of the telescope. The CCD camera views the target through the telescope. Tilting alignment by using fine adjustments on the side of the retro-reflecting mirror can be made and the field of view can be adjusted by moving the imaging lens forwards or backwards. The system is designed to make 6 possible alignment adjustments. After the retro-reflecting mirror is moved forward or backward, the field of view can also be adjusted. The maximum field of view that we can obtain is  $\sim 5.0$  cm diagonally. The distance  $d$  from the objective lens to the imaging lens is related to the field of view at the target. For target to be in focus, one must obey the lens formula,

$$\frac{1}{f} = \frac{1}{c} + \frac{1}{d} , \quad (3.5)$$

where  $c$  is the distance from the target to the objective lens and  $d$  is the distance from the objective lens to the camera.

### 3.1.2.3 *high speed cameras and light sources*

Table 3.1 gives the specifications of high speed cameras in terms of some selected attributes. Two FastVision cameras with CCD size of  $15.4 \times 12.3$  mm run with a full  $1280 \times 1000$  pixel resolution at a 0.5 kHz frame rate. One Olympus Encore PCI 8000S camera with 1/3 inch CCD size runs with a  $480 \times 420$  pixel resolution at a 4 kHz recording rate. A high speed "Silica Mountain Devices (SMD)" 64KIM camera with a CCD size of  $13.4 \times 13.4$  mm runs with a reduced single frame size of  $(960 \times 960)/4$  pixel resolution at up to 1 MHz frame rate. For the three slower cameras, images collected by each individual imaging fiber overfill the CCD pixels by a factor of  $\sim 6$  and  $\sim 3$ , respectively, i.e. one fiber projected onto  $6 \times 6$  and  $3 \times 3$  CCD pixel area, respectively. However, for the SMD camera, each imaging fiber slightly underfills the CCD pixels by a factor of 0.83, i.e. one fiber projected onto nearly a single CCD pixel area. Due to the nature of spatial superposition, an array of imaging fibers imaged by an array of CCD pixels, some images might compose of a honeycomb pattern caused by this pixelation artifact. However, the artifact can be minimized by slightly defocusing the image on the CCD. However, the FastVision and Olympus CCDs are capable of recording at a frame rate higher than 500 Hz, the architecture for binning at reduced resolution requires a change of the zoom ratio on the image head doom. The SMD camera has a different but fixed binning architecture so that the full field of view is taken at a high speed frame rate with reduced resolution. Except for the SMD camera where images are frozen by the short 150 ns illumination laser pulses, all other

images are arrested by the short adjustable electronic exposure time of  $10 \sim 50 \mu\text{s}$  set on the CCDs.

Synchronized short laser light pulses are used to illuminate the target and freeze the motion of the jet after the impact of the proton beam. For SMD camera, the mask reduces the photosensitive area to 0.03 of the nominal pixel area. The quantum efficiency of the photo-resistive area is 0.18 at 800 nm, and the pixel fill is 200000 electrons. Therefore, a full exposure of a frame of the CCD therefore requires  $(960)^2 \times 200000 / 0.03 / 0.18 \approx 3.4 \times 10^{13}$  photons or 10 Watts for 800 nm photons. For FastVision camera, the sensor is  $1280 \times 1024$  pixel (1.03 megapixel) of CCD of total area  $15.36 \times 12.29 \text{ mm}^2$  in 8 bits at 500 frames per second (10 bits at 400 frames per second). Maximum frame rate is 500,000 at  $1 \times 1280$ . The mask reduces the photosensitive area to 0.4 of the nominal pixel area. Based on the estimation of required photons, a full exposure of a frame of the CCD therefore requires  $1280 \times 1024 \times 200000 / 0.4 / 0.18 \approx 3 \times 10^{12}$  photons or 1 Watts for 800 nm photons.

Optical light pulses are sent through 15 meters of multi-mode illumination fibers. The light sources used in the experiment are all Class 4 lasers, emitting at wavelengths of 808 to 850 nm. Three lasers are capable of emitting a peak optical power of 1 Watt (JDS Uniphase SDL-2300-L2) driven by three independent current drivers (ThorLabs LDC220C). These 1 Watt lasers can be operated from CW to a minimum programmable pulse width of  $1 \mu\text{s}$  limited by the trigger logic pulse. The 4<sup>th</sup> laser emits at a peak optical power of 25 Watt (Bright Solution BDL20-808-F6) limited by the pulsed current driver (Avtech

AXOZ-A1A-B). It provides a current pulse of 150 ns and is capable of running at the maximum 1 MHz repetition rate, i.e. a frame rate of 1  $\mu$ s/frame.

The complete transmission of the imaging system is  $\sim 0.2$  per viewport channel, including 0.85 for the 15 meter long illumination fiber, 0.86 for the sapphire ball lens, 0.86 for each pass of the sapphire viewport, 0.91 for the retro-reflector, 0.67 for the 10 meter long imaging fiber, and 0.86 for the grin lens and the relay lens. For the SMD camera, the imaging circle filled  $\pi/4$  of the CCD array. A measured output energy of 3.5  $\mu$ J/pulse is obtained from the Bright Solution (BDL20-808-F6) laser illumination light source for viewport 2. Therefore the calculated number of photons impinging on the SMD camera reaches  $4.2 \times 10^6$  photons/pixel. After taking into account the 18% quantum efficiency of the CCD,  $7.5 \times 10^5$  photoelectrons are generated at the full illumination intensity. Since the SMD camera has full well capacity of  $2.2 \times 10^5 e^-$ , there is a factor of  $\sim 3$  on the optical power budget reserved for unanticipated optical power loss and for overcoming the possible attenuation due to ionization radiation. Similar calculations for viewport channels 1 and 3 give a factor of  $\sim 10$  on the optical power budget. This larger factor is mostly due to the long, 10  $\mu$ s, exposure time set on the FastVision cameras. Overall, the imaging system is designed to have sufficient optical power budget for the illumination of each viewport throughout the entire experiment.

#### 3.1.2.4 *radiation-hardness*

Because of the high radiation level in the beam tunnel and the activation of the mercury after the proton beam interactions, all optics placed inside the interaction beam tunnel are required to be radiation-hard. One complete set of optics was selected for radiation resistance test done at CERN. This complete set of optics included an Au-coated reflector, sapphire window, illumination fiber, imaging fiber, and Grin objective lens. The experiment has anticipated a total of 200 proton pulses at 14 and 24 GeV with a total of  $\sim 3 \times 10^{15}$  protons. The calculated total radiation reaches  $\sim 1$  Mrad equivalent radiation dose. Therefore, all optics except the grin objective lens were irradiated at CERN to a lower energy 1.4 GeV proton beam but up to an equivalent radiation dose of  $5 \times 10^{15}$  protons. Because we missed an opportunity to deliver the grin lens to the CERN irradiation facility, the grin objective lens was instead irradiated at BNL using a Co-60 source up to a total dose of  $\sim 3$  Mrad.

The reflectance of the Au-coated reflector and the transmittance of all other optics are measured at the wavelength of 830 nm before and after irradiation. Table 3.2 shows the effects of irradiation up to an equivalent radiation dose of 1 Mrad on the reflectance and transmittance of the components of the optical diagnostic system. No noticeable change in the reflectance was observed on the Au-coated reflector even though the substrate of the reflector has turned nearly opaque. The sapphire, 5 meter long of illumination fiber, and 0.3 meter long of imaging fiber do not show any additional insertion loss. They are all radiation hard up to a 1 Mrad dose. However, the small grin objective lens did suffer

radiation damage resulting in a 0.73 transmission. This tiny grin objective lens is made of silver-ion exchanged index modification internal to a glass substrate. Therefore it was not anticipated to have a high radiation resistance. However, it is well known that although glass (and silica fibers) lose its transmission in the visible wavelengths, near infrared (NIR) light can still has adequate light throughput for some applications (Kakuta, 1999). This is one of the reason we select NIR rather than visible laser light for back-illumination of the mercury jet. Since the back-illuminated NIR light passes the grin objective only once, the 0.27 transmission loss over the entire experiment is tolerable and can be recovered with the present designed laser capability. We should note that the integrity of the imaging properties of the grin lens was unchanged, i.e. no image distortion was observed after the 1 Mrad radiation resistance test.

### **3.1.2.5 *scintillating fiber channel***

A jacketed 2 meter long 1 mm diameter blue emitting scintillating fiber is attached along with the imaging head to register gamma emission during the proton beam and mercury jet interaction. A 12 meter long 1 mm diameter fiber patch-cord (ThorLabs BFH37-1000) carries the blue scintillated light signal and is fiber-coupled to an Avalanche photodiode (ThorLabs APD210), designated as channel 0. The overall transmission at the center wavelength of 480 nm of the fiber patch-cord is measured to be 0.77. The scintillating signal trace is displayed on an oscilloscope and data can be retrieved remotely from the control room. This scintillating signal serves to confirm the arrival of the

proton beam and has the potential to extract the proton intensity from the scintillating signal pulse level.

### **3.1.3 Schematic of electronic trigger and high speed camera control**

Because we are using several high speed cameras from different vendors, we must use separate camera control software for each camera. The limitation on their exposure time also requires two different set of illumination laser pulse trains. A master trigger pulse, synchronized to the arrival of the proton bunch, is delivered to trigger the mercury loop system, the solenoid magnet system, and the optical diagnostic system together. The mercury jet reaches its steady state for 1 second when the solenoid magnet reaches the highest magnetic induction field of 15 T. However, there is a significantly long time lag of  $\sim 10$  seconds for the solenoid system to power up to its full capacity. Therefore, the master trigger signal is first sent to a digital delay generator (Stanford Research DG535) to provide a sufficient long delay to synchronize with all other electronic components. These relative and absolute delays are measured by an oscilloscope. By adjusting each independent delay channel, complete synchronization of all cameras with the pulsing of the laser light sources can be achieved and verified by comparing the bright/dark image intensities of each frame of each CCD.

Fig. 3.5 shows the two sets of pulse sequences used to simultaneously trigger all cameras. The 25W infrared laser consisted of a 17 pulse sequence with a



pulse width of 150ns. This determines the exposure time of the SMD camera on the viewport 2. The laser pulse period is set to match the frame rate of the images. The SMD camera collects 16 frames of image.

Three 1 Watt lasers pulsed to a 0.5 second duration are used to independently illuminate viewport 1, viewport 3, and viewport 4, respectively. Typically the FastVision and Olympus cameras continuously collect 260 frames of images. The exposure times on the cameras are set at  $10 \sim 50 \mu s$  respectively to give a sharp image quality. Although the sharpness of images increases with reduced exposure time, much more light is required for illumination. Therefore, a trade off between exposure time and laser intensity is made. On the contrary, the exposure time for SMD camera is determined by the laser pulse width. As the pulse width of the laser decreases, the laser intensity also decreases. In order to utilize the maximum allowable intensity of the 25W laser, the maximum pulse width of  $0.15 \mu s$  is used. This pulse width should not seriously jeopardize the image quality even running at its highest frame rate of  $1 \mu s/\text{frame}$ . A schematic diagram linking all cameras, triggering electronics, and controlling computers is shown in Fig. 3.6. 2 desktops reside in the control room to master the optical diagnostics system. All other electronics and desktops are placed in the TT2 tunnel adjacent to the interaction beam tunnel TT2A.

## **3.2 Windows Consideration as Viewports for Observation**

The mercury jet target is observed through four windows. These windows must contain any possible spray of mercury due to intense beam energy deposition, and remain transparent after a radiation dose from the interaction of beam and mercury.

### **3.2.1 Fiducial mark on windows**

We put fiducial mark on each sapphire window to use the magnitude of the referenced length. The size of fiducial on the back and front windows is varying on images according to the changing field of view. i.e, the back fiducial looks smaller than the front fiducial. Fig. 3.7 shows the artificially marked fiducial on the sapphire window. It gives referencing length scale when we measure the size of jet, velocity, rotation of windows, and the location of magnetic axis on images.

### **3.2.2 Impact resistance test**

We used sapphire windows to obtain enough strength and did surface coating on both sides for anti-reflection at 800nm wavelength. In order to check the survival from mercury droplet impact, we tested sapphire window using a paint ball gun. A paint ball is a 2.75 gram sphere of radius 8.6 mm containing a colored gel that readily “splats” on impact. The velocity of a paint ball was 95m/s. The ratio of the force from a paint ball to that due to the dispersal of

the entire mercury jet by the proton beam is

$$\frac{F_{\text{paintball}}}{F_{\text{mercury}}} = \frac{m_{\text{paintball}} v_{\text{paintball}}^2 r_{\text{mercury}}}{m_{\text{mercury}} v_{\text{mercury}}^2 r_{\text{paintball}}} . \quad (3.6)$$

The momentum of the paint ball is the same as that of a 7 mm diameter mercury drop at 95 m/s. The sapphire window survived in the test.

### 3.2.3 Pressure leaking test of sapphire windows

The primary containment is mostly welded and the window ports are sealed with rubber gaskets (BUNA-N). Each window is sealed with two sheets of rubber gaskets per port. 21 psi is loaded inside the primary containment to check the sealing of the primary containment. To locate leaks, a Metheson 8850 flammable gas sniffer, which has a 5ppm sensitivity, and Ar/Methane (90 % / 10 % ) was used. All of 8 windows survived the 21 psi pressure for over 17 hours.

## 3.3 Integrated Experimental Setup for High Power Target

### 3.3.1 Mercury loop system in solenoid magnet

The cross-section and actual equipment for the mercury system with high field solenoid magnet is shown in Fig. 3.8. The horizontal line in Fig. 3.8(a) represents the proton beam. The Hg jet, which is ejected from right to left in Fig. 3.8(a), co-propagates with the proton beam. Four viewports are shown within the solenoid bore, which represent viewing locations for observation of

the Hg jet within its primary containment vessel (see Fig. 1.3). Viewport 2 is positioned at the center of the solenoid and is the location where the center of the proton beam interacts with the Hg jet. The Hg system provides for double containment vessel of the hazardous liquid metal, and can be inserted or removed from the solenoid bore without disassembly. A hydraulic syringe pump, with a piston velocity of 3 cm/s was used to pulse the mercury jet. This pump minimizes the heat added to the Hg as opposed to a centrifugal pump. The syringe pump also reduces the discharge pressure which is the limitation of a centrifugal pump. The Hg system provides a jet duration of a  $\sim 3$  seconds of constant velocity profile. A total of 180 kg of Hg is loaded in the system. A 30 KW, 200 bar hydraulic power unit drives the syringe pump.

The pulsed solenoid incorporates a magnetic induction field ramp up of 10 seconds and is capable of sustaining its peak field for a duration of approximately 1 second. A 5.5 MW, 700 V power supply delivers 7500 A of current to pulse the solenoid. The magnet is cryogenically cooled to 77 K prior to operation and warms up by 30 K during pulsing due to 30 MJ coil heating. Therefore, a 30 minute cooling time is needed for each single shot. The magnetic axis is positioned at an angle of 67 milliradian to the proton beam, with the tilt provided by a common baseplate supporting all the equipment (see Fig. 3.8(a)). The applied magnetic induction field has been measured with a gaussmeter placed both perpendicular and parallel to the magnetic induction field. The relationship between the measured magnetic induction field and the applied solenoid current was mapped to deduce the maximum magnetic

induction field at the center of the solenoid. It was found that the maximum magnetic induction field reached 15 T at Plasma Science and Fusion Center in Massachusetts Institute of Technology.

### **3.3.1.1 *the considerations in nozzle design***

Better yields of low energy pions are obtained from the mercury jet target when the proton beam and target are tilted with respect to the axis of the capture solenoid magnet. Monte Carlo simulations have indicated that a tilt angle of about 100 milliradian between the mercury jet and the proton beam is optimal (Mokhov, 2000). However, jet motion in a magnetic induction field behaves differently, depending on the angle between the axis of the magnet and that of the jet, as a result of the differences in the magnitude of the components of the magnetic induction field (Samulyak, 2006). As the crossing angle increases, the transverse component of the magnetic induction field increases, but with no significant change in the longitudinal component. The increase in the transverse component of the magnetic induction field raises the induced current on the Hg jet. Therefore, the angle of the Hg jet is launched at 33 milliradian with respect to the axis of the magnet, resulting in an interaction region about 30 cm long in case of a 1 cm diameter mercury jet with a 1.5 mm RMS diameter of proton beam. Since the proton beam in TT2A beamline at CERN is horizontal, the mercury jet should make a 34 milliradian angle with respect to the proton beam axis, and the magnetic axis should make an angle of 67 milliradian with respect to the proton beam. The mercury will flow from

the upstream end of the magnet to the downstream end of the magnet. The jet velocity is designed to be 20 m/s and the center of the jet to intersect the center of the proton beam at center of magnet.

### **3.3.2 Water jet observation for nozzle performance test**

Prior to mercury injection in the primary at Oak Ridge National Laboratory(ORNL), extensive optical diagnostics were carried out by pulsing water jets in the system using 4 different types of nozzle configurations. One nozzle showed the most stable shape of jet motion with fairly uniform velocity,  $\sim 10$  mm diameter and 20m/s respectively.

Due to the spray and wetting of water on the interior of windows, only ambiguous shadow of the water jet was observed. A clear surface motion is required in order to obtain accurate velocity measurement. Therefore, only qualitative diagnostics was made on the water jet. The field of view of each viewport is  $\sim 50$  mm. The diameter of the jet is measured by overlaying a grid of referenced field of view onto the images. The time lapse of each frame is read from the camera frame rates. The trajectory of the jet between several frames can then be measured and the velocity of the jet surface motion is estimated.

These measurements of the water jet tests were done at ORNL. The observations led us to select the design of the final nozzle for the subsequent jet runs. It was fabricated from Titanium and the assembly was anodized for electrical insulation.

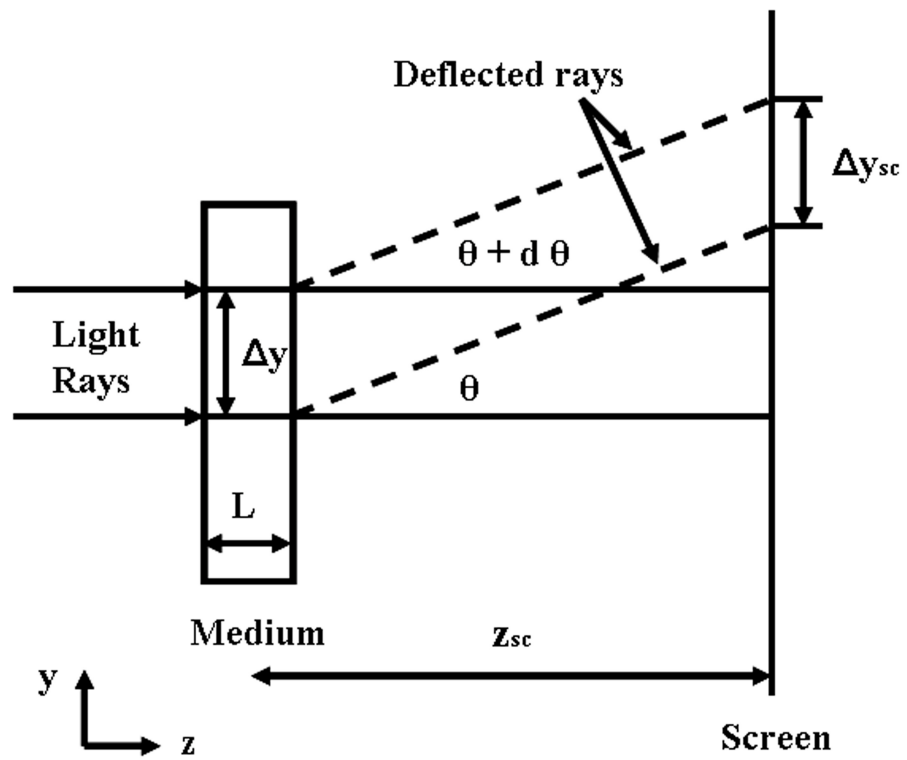


Figure 3.1: Displacement of light beam for shadowgraph.

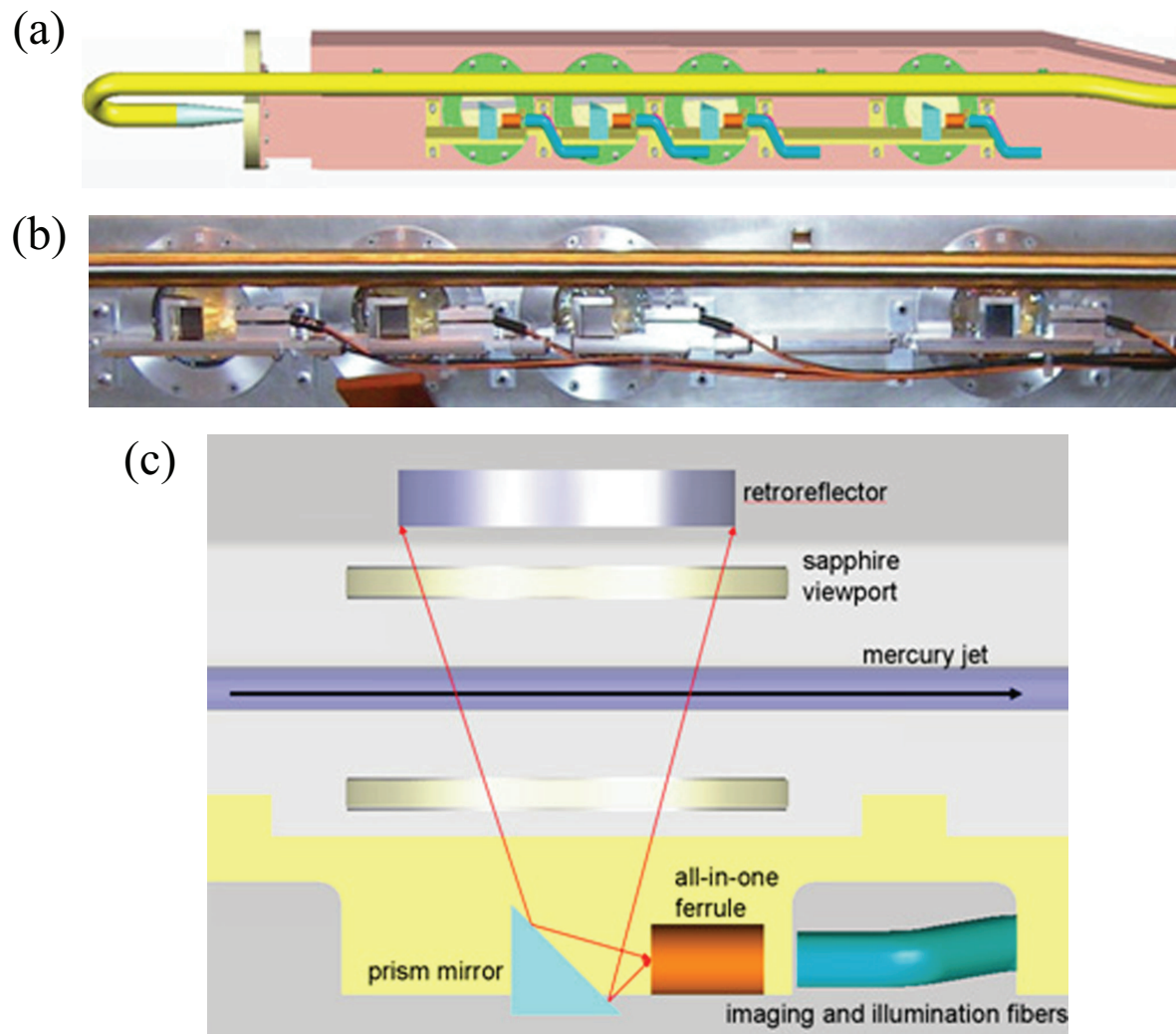


Figure 3.2: Design of optical layout and installation of 4 Viewports of primary containment vessel. a.) Conceptual integration of optics to primary containment vessel. b.) Photograph of installation of optics to primary containment vessel. c.) Schematic layout of optical components.



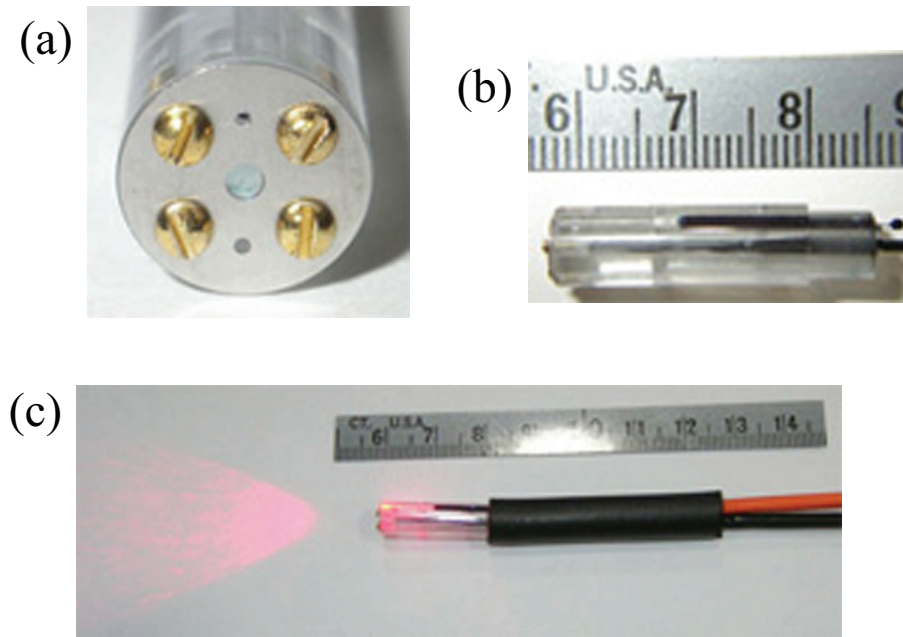


Figure 3.3: Photograph of optical head assembly and its illumination of laser. a.) Front view of optical head assembly. b.) Side view of optical head assembly. c.) Illumination of fiber-optics head assembly.

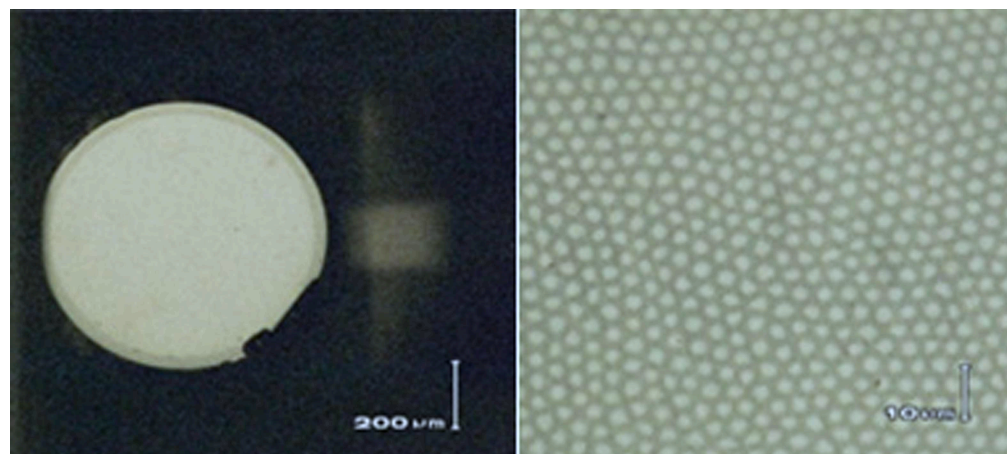


Figure 3.4: Polished fiber end, 50X and 800X magnifications, respectively

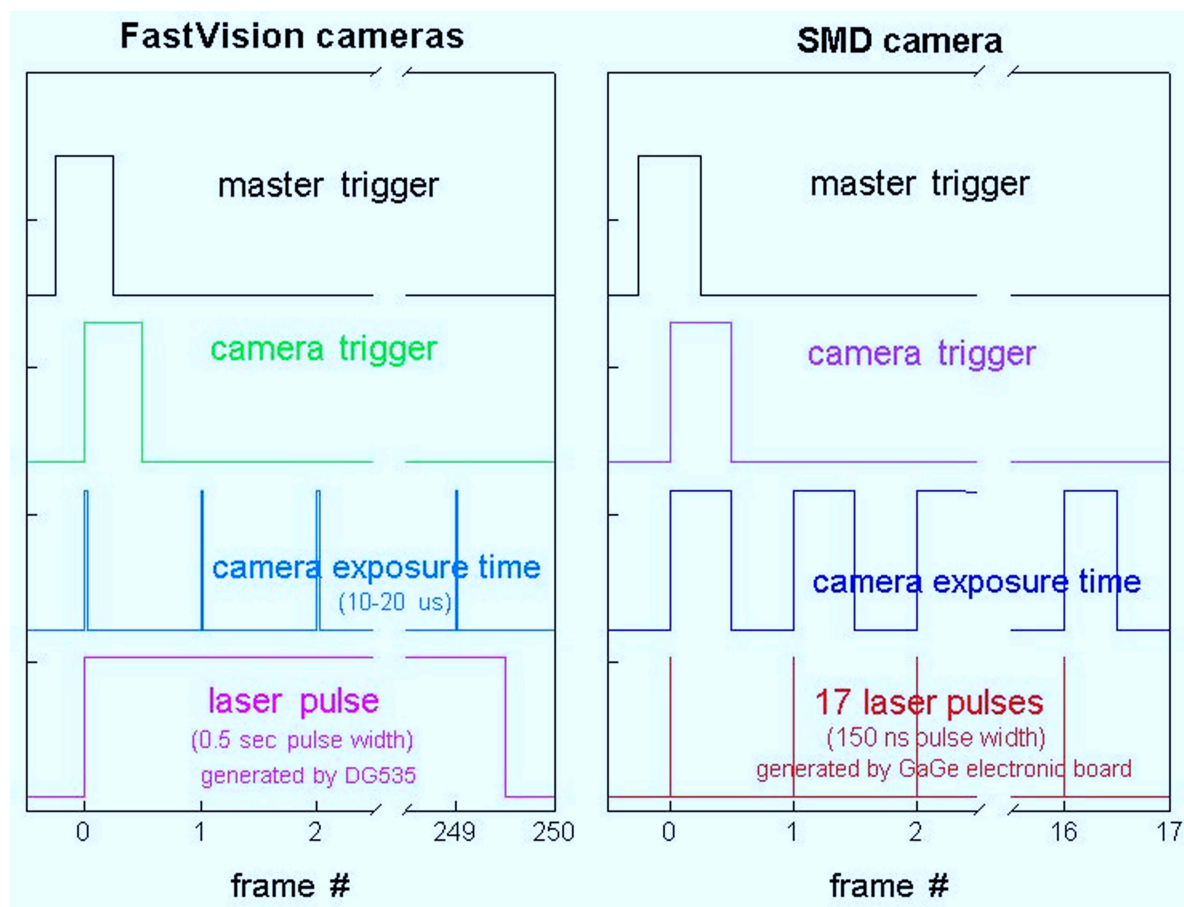


Figure 3.5: Schematic of synchronized signal of high speed camera and laser pulse.

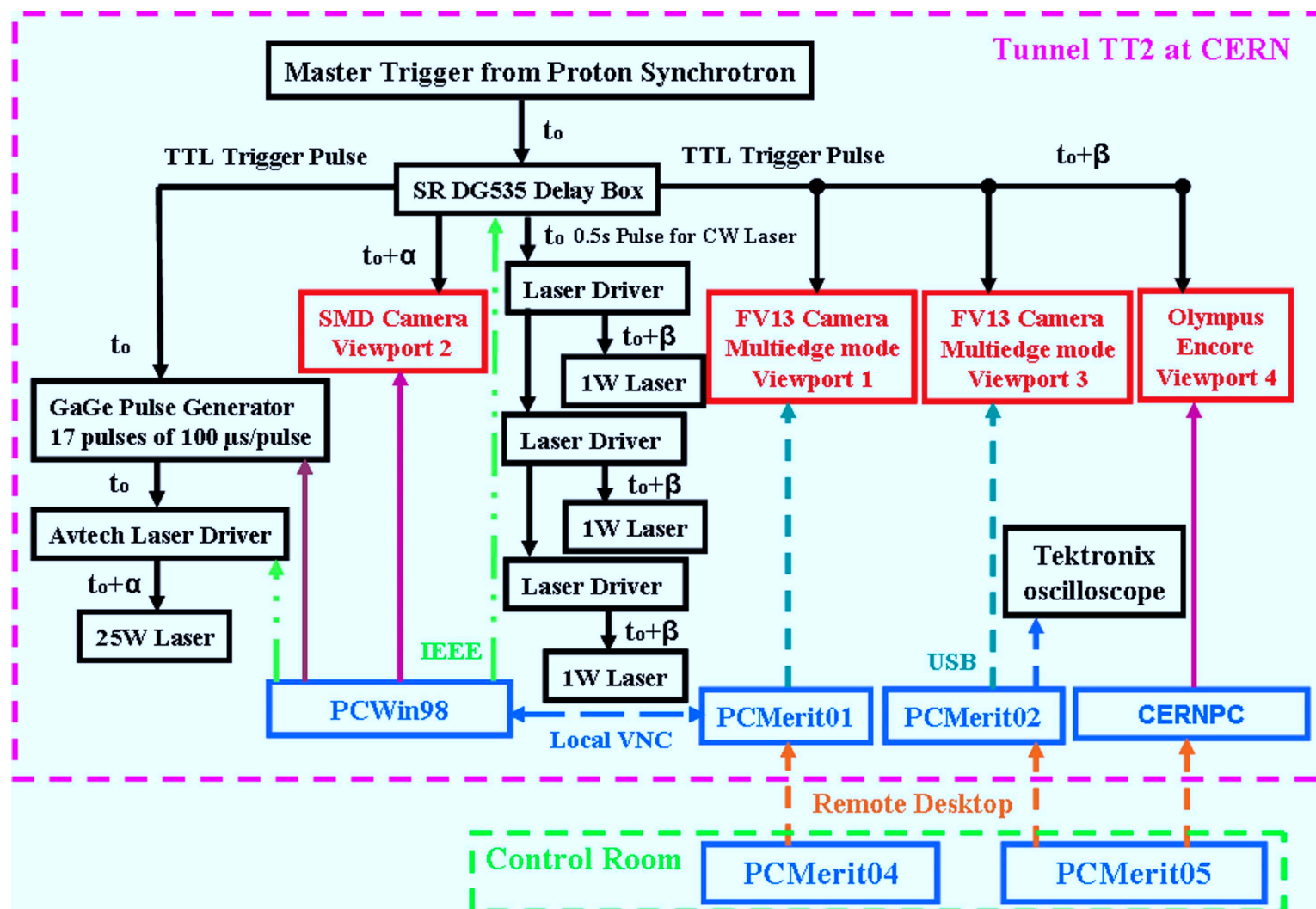


Figure 3.6: Schematic of electrical triggering and high speed camera control in tunnel for experiment.

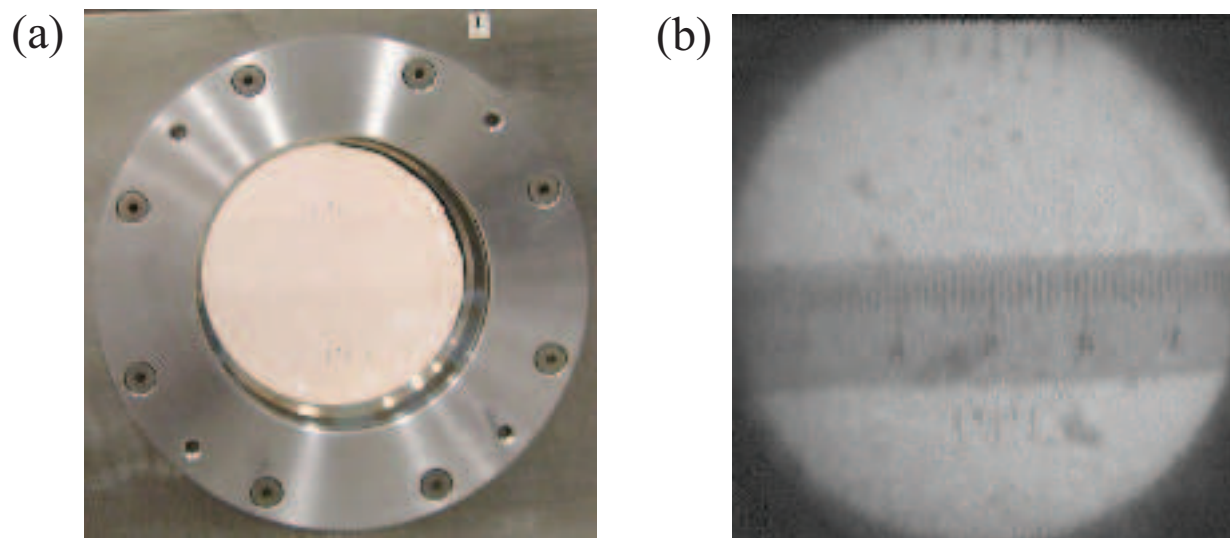


Figure 3.7: Top fiducial on the front window and bottom fiducial on the rear window. a.) Photo of fiducial on the sapphire window assembled in Viewport. b.) Image of fiducial captured by camera.

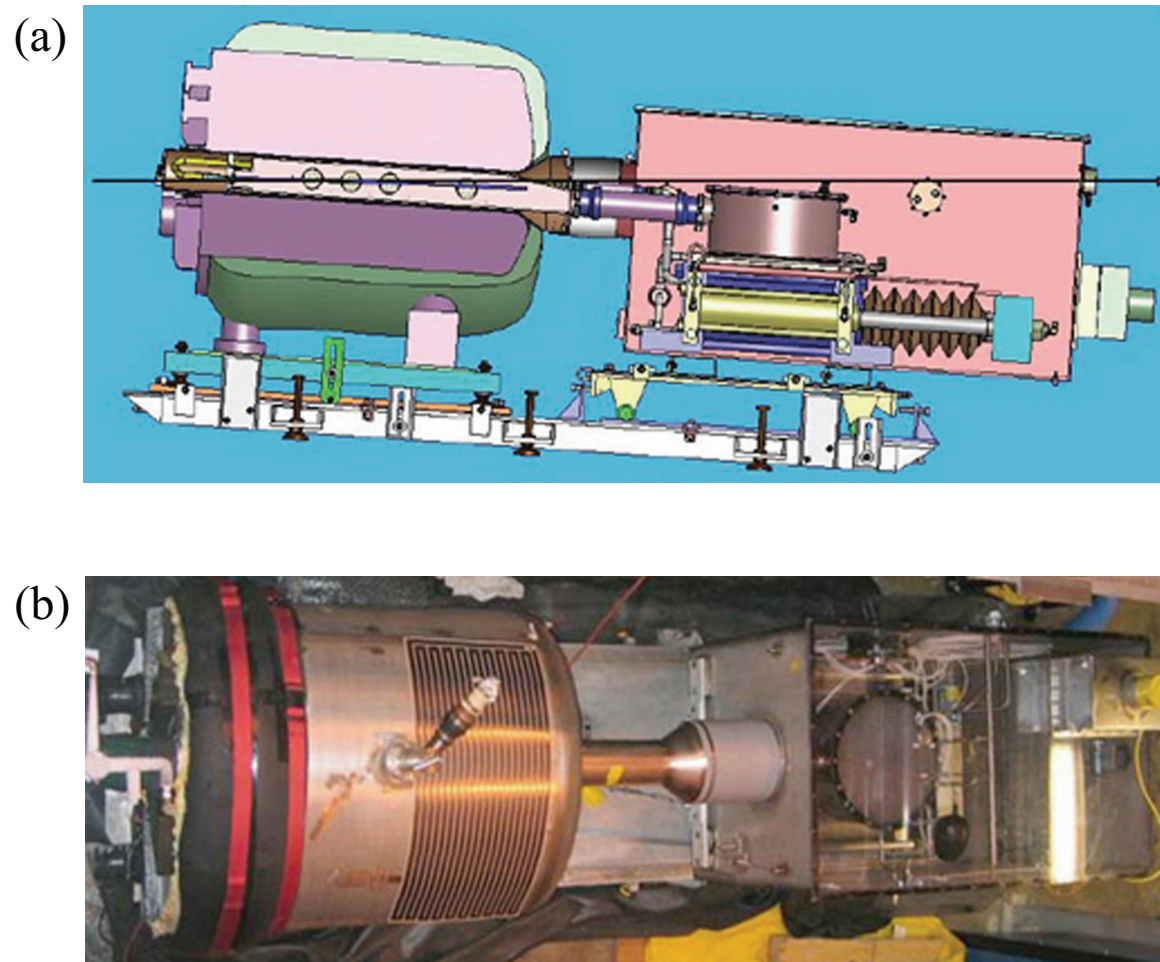


Figure 3.8: Photographs of the entire MERIT experiment. a.) Sectional side view of mercury loop system integrated with 15 T solenoid magnet. b.) Fabricated mercury loop system assembled with 15 T solenoid magnet (Top view).

Table 3.1: Specifications of high speed cameras.

Attributes	SMD 64KIM	FastVision	Olympus Encore PCI 8000S
CCD chip size	13.4 mm $\times$ 13.4 mm	15.4 mm $\times$ 12.3 mm	1/3 inch
Pixels	960 $\times$ 960	1280 $\times$ 1024	480 $\times$ 420
Pixel size	14 $\mu$ m	12 $\mu$ m	13 $\mu$ m
Single frame	240 $\times$ 240	1280 $\times$ 1000	480 $\times$ 420
Maximum frame rate	1 MHz <sup>1</sup>	0.5 kHz <sup>2</sup>	4 kHz <sup>3</sup>
Full well Capacity	220,000 $e^-$	$\sim$ 1000 LSB/lux-sec	-
ADC	12 bit	8 bit	8 bit

---

<sup>1</sup> 16 frames.

<sup>2</sup> at full resolution.

<sup>3</sup> 12.5  $\mu$ s electronic shutter, with reduced frame size.

Table 3.2: Effects of irradiation up to an equivalent radiation dose of 1 Mrad on the reflectance and transmittance of the components of the optical diagnostic system. Reflectance is inferred on the Au-coated mirror and transmittance is inferred on all other components.

Optical component	Before radiation	After radiation	% difference
Large Au-coated mirror	0.91	0.92	no change
Sapphire window(1-mm)	0.86	0.87	no change
Illumination fiber(5m)	1	1.02	no change
Imaging fiber (30 cm)	0.67	0.71	no change
Grin lens	0.90	0.66	73 %



## Chapter 4

# Results of Experimental Investigation of MHD Flow for an Intense Proton Target

In this chapter, the jet behavior in magnetic field and its interaction characteristics are investigated. To do this, the collected images are read digitally and the characteristic jet parameters are evaluated based on the probability approach. It effectively diagnoses the jet condition on each collected image. Jet deformation such as the free jet surface deformation and surface stabilization is investigated by measuring the pixels on the collected images based on 2-D shadow photography. As a result, we will discuss the magnetic field effect to the dynamic behavior of freely moving jet in a solenoid. The driving pressure of mercury flow entering inlet pipe is measured to monitor the effect of the magnetic field and assure if the input condition for driving the jet is affected. The disruption of the jet interacting with different beam intensities and beam energy is observed and the magnetic suppression to it is discussed. The captured images show the mechanism of the beam-jet interaction and

the consistency with the calculated energy deposition is discussed. The energy deposition induced by the proton beam generates filaments on the Hg jet surface due to thermal stresses. The filamentation velocity and its reduction by magnetic field are discussed. It explains that the joule damping dissipates the kinetic energy on a time scale of joule damping term.

## 4.1 Image Analysis for Data Reduction

### 4.1.1 Image acquisition

$\sim 360$  complete integrated tests (i.e., with magnet, proton beam, Hg loop system, and optical diagnostic system) were conducted at CERN (European Organization for Nuclear Research) with various values of the proton beam structure (8 harmonic and 16 hamonic) and the beam intensity up to  $30 \times 10^{12}$  protons and the beam energy (14 GeV/c and 24 GeV/c) and the the magnetic field (0T, 5T, 7T, 10T, and 15T) and two Hg jet velocities (15 m/s and 20 m/s). Fig. 4.4 and 4.5 are representative optical diagnostic results collected by the 3 cameras, with and without a magnetic induction field at Plasma Science and Fusion Center in Massachusetts Institute of Technology. Note that the Olympus Encore PCI 8000S camera for Viewport 4 was integrated in the beam interacting target study done at CERN.

The current in the magnet system generates heat, which is cryogenically removed using liquid nitrogen. As the magnet cools down, all Viewports become foggy up due to condensation. It was found out that  $\sim 0.5 \ell$  of water (from nozzle performance test at Oak Ridge National Laboratory) was not

removed from the system prior to loading Hg. Flexible heater strips were installed both on the exterior of the primary containment vessel and on the snout in order to prevent the condensation of the humid air on the Viewports. Although residual Hg droplets in sizes less than 1 mm often adhere to the sapphire Viewports after every shot, jet motion with adequate image quality could still be collected.

#### **4.1.2 Image processing**

To measure the shape of the jet, 8 and 12 bit grey scaled TIF images are converted into digital forms. Background images are subtracted to reject the noise in the image digitization process. The residual data is then transformed into a 2 bit scaled image. Fig. 4.1 shows the collected image and its transformed 2 bit scaled image. Only the black and white colored pixels in the 2 bit depth images are used to differentiate the shadow of the jet and the background. Due to the image quality caused by the Hg droplet on window and the quality in fiber optic system, the noise such as black dots exists. A threshold is adjusted according to Otsu's method to highlight the interface between the mercury and background (Otsu, 1979). Otsu's method selects the threshold by minimizing the within-class variance and maximizing the between-class variance of the two groups of pixels separated by the thresholding operator. Otsu's method, which relies on the assumption that all image pixels belong to one of two classes, background or foreground, has been shown to be efficient in image segmentation for bi-level thresholding.

Fig. 4.2 show the sensitivity of 2 bit scaled image conversion to the measurement of jet height using Otsu's method. As the threshold level increases, the mean value of the jet height as well as the  $\sigma$  value of the jet height in measurement is approaching an asymptotic level. The optimally selected threshold value by the Otsu's method in this example is 0.35.

The Hg jet was observed at upstream (Viewport 1), midstream (Viewport 2), and downstream (Viewport 3) locations from the nozzle exit. 220 images are collected at each run for both the upstream and downstream locations, with an image size of  $1280 \times 1000$  pixels. The most probable transverse jet height within the longitudinal pixel range of 300 to 1000 is shown in the histogram of Fig. 4.3(a). Note that within this range, the transverse jet height probability  $P$  is obtained by counting the number of longitudinal pixel events in the jet image. If  $z$  denotes the transverse direction (in terms of pixels), the histogram in Fig. 4.3(a) can be written as (Eqn. (4.1)) using the least square curve-fairing approach:

$$P(z) = P_1 \frac{1}{\sqrt{2\pi}\sigma_1} e^{-\frac{(z-\mu_1)^2}{2\sigma_1^2}} + P_2 \frac{1}{\sqrt{2\pi}\sigma_2} e^{-\frac{(z-\mu_2)^2}{2\sigma_2^2}}, \quad (4.1)$$

where  $\mu_1, \mu_2$  are the means,  $\sigma_1, \sigma_2$  are the standard deviations, and  $P_1, P_2$  are the a-priori count of the histogram distribution. Note that, in pixel units,  $\mu_1=386$ ,  $\mu_2=401$ ,  $\sigma_1=3.8$ , and  $\sigma_2=21.6$ . The number of background events (i.e., outside of the jet) is always larger than that within the jet because the portion of bright background on each image is larger than that of the black jet shadow. The distribution on the left in Fig. 4.3(a) (i.e.,  $0 < z < 200$ )

represents the background pixels and is not included in the faired curve in Fig. 4.3(b).

On Viewport 2, 16 image files are collected at each run, with an image size of  $316 \times 316$  pixels. The images are analyzed in the same manner as described above. Viewports 1 and 3 give the same resolution for the images:  $1280 \times 1000$ . Thus, no image re-scaling is needed when comparing the pixel size for these images. However, Viewport 2 gives a resolution of  $316 \times 316$ . Based on the 1 cm scale fiducial mark on the exterior of all Viewports, all images taken on this Viewport are re-scaled to match the resolution of Viewport 1 prior to comparison.

### **4.1.3 Study on the scaling length and the location of center of window**

In order to relate the lengths on the collected images at each Viewport, the pixel length on the images has to be investigated. Since the image size corresponds to the CCD size, any discrepancy in horizontal and vertical pixel size is not considered. Viewports 1 and 3 give the same resolution for the images:  $1280 \times 1000$ . Thus, no image re-scaling is actually needed when comparing the pixel size for these images but did the scaling to see any difference on the image length of Viewport 1 and Viewport 3. The fiducial length on the top front window and the bottom back window is measured and then interpolated to get the length at the mid-span on the primary containment. The interpolated pixel length at the mid-span corresponds to 1 cm at the mi-span

of primary containment. Thus, in Viewport 3, a pixel length at the mid-span where the jet is moving is approximated  $\sim 0.05$  mm. Same scaling was done at images in Viewport 3. The ratio of the pixel length in Viewport 3 to Viewport 1 is 1.06.

Viewport 2 gives a resolution of  $245 \times 252$ . Based on the 1 cm scale fiducial mark on the exterior of all Viewports, all images taken on this Viewport are re-scaled to match the resolution of Viewport 1 prior to comparison. A pixel length at the mid-span is approximated  $\sim 0.21$  mm. Viewport 4 gives a different resolution of images depending on the frame rate setting but typically the resolutions of  $320 \times 280$  was used. A pixel length at the mid-span is approximated  $\sim 0.21$  mm, which is same with Viewport 2.

The distance of the center position between the fiducial and the window is 0.75 inch apart. In order to locate the center of the window at the mid-span, the positions where 0.75 inch is apart from the top fiducial and bottom fiducial is found on each image and then the averaged difference in the located position is considered as the center of window.

Based on these scaling study, the measurement is performed for the following investigation. The measurement is averaged for  $\sim 200$  images to give a result of the following investigation and the standard deviation is also calculated for the individual measurement respectively. Based on the standard deviation and the number of events, the error bar,  $\sigma/\sqrt{N}$ , is calculated to give error estimation for each measurement.

## 4.2 Motion of Mercury Jet and Stability in Magnetic Field

### 4.2.1 Jet deflection and surface flattening

When the jet is injected without an applied magnetic field, it is difficult to discern the jet surface because of blockage by Hg droplets on the window. Therefore, some errors in the measurement exist (see images Fig. 4.4(a) through Fig. 4.4(c) and 4.5(a) through 4.5(c)). On the contrary, when a magnetic field is applied, the measurement errors are significantly reduced, leading to significantly less intermittent jet boundaries.

The inertial forces appear to dominate the jet movement when the jet velocity is 15 m/s. The turbulent jet motion is unstable but becomes stabilized as the magnetic field approaches 5 T. It has been reported that the radial force induced by the transverse component of magnetic field caused by the axially induced current due to the tilted jet angle can significantly increase the jet height (Gallardo *et al*, 2002). The phenomena of increasing jet thickness with high magnetic induction field is observed for the first time when the magnetic field exceeds 10T.

The Fig. 4.7 (a) shows the jet height variation by the magnetic field strength. The Fig. 4.7 (b) shows the distortion ratio of jet by the magnetic field, where the nominal jet height is considered as the height at Viewport 1 with no magnetic field. Since the jet diameter is in nature diverging but relatively the jet diameter is not changing at Viewport 1, it is appropriate that

the experimentally determined height at Viewport 1 can be considered for the nominal jet height to calculate the ratio of jet height. At a jet velocity of 15 m/s, the relatively low inertial force reduces the extent of turbulent fluctuation. For this case, the magnetic field does not significantly affect the dynamics of the jet until the magnetic field strength of  $\sim 5$  T reaches. Consequently, the height of the jet decreases only slightly until 5T since the magnetic field reduces the fluctuating surfaces and the jet is more likely to elongate axially to the jet axis. The results shown in Fig. 4.4 and 4.5 clearly suggest that the magnetic field has constrained (stabilized) the Hg jet flow by smoothing out the edges of the otherwise turbulent flow. At large number of the magnetic field ( $>10$  T), stability is maintained at all Viewports. At 15 T, a larger height (cross sectional distortion) is observed on all Viewports.

The fact that the Hg jet size is relatively reduced from 0 T to 5 T but increases from 10 T to 15 T suggests that the Hg jet might encounter a different type of instability at high field, namely a quadrupole effect. The quadrupole effect would alter the jet's circular cross-section to become elliptical. From the data obtained with a 15 m/s jet, the jet height at a 10 T is smaller than that at 15 T, which is manifested in the vertical elongation of the jet. However, the height at a 10 T is smaller than that at 5 T. The issues for such a behavior have to be addressed. There are two possibilities. First, the jet is elongating axially up to 10 T. The equivalence of hydrodynamic pressure with magnetic pressure is more dominantly affecting to the axial elongation of jet than the transverse pressure. Eqn. (2.67) shows the magnetohydrodynamic



stress tensor, which indicates the ration of the axial pressure and the transverse pressure. The increasing axial pressure of jet is more elongating from 0 T to 10 T. However, the transverse magnetic pressure becomes significant once the magnetic field exceeds 10 T. Thus, the jet at 15 T is experiencing the transverse deflection as well as axial deflection, but the the role of transverse deflection plays significantly on the behavior of jet. That can explain why the reduction of jet is appearing up to 10 T and then the expansion of jet is appearing at 15 T.

Second, the optical diagnostics depends only on the side sectional view of jet movement. The reduction of jet size on the minor axis of the elliptical core has to be accompanied by the gain in jet size on the major axis in order to satisfy the continuity condition in flow. In other words, the cross-sectional are in flow should be constant. Although the two dimensional nature of the image data does not distinguish between an elliptical cross section and a circular one, occasional observation of a smaller jet thickness at 15 m/s with 10 T field as opposed to a 5 T indicates that the jet cross section might vary between the major and minor axis of an elliptical core. It is important to note that within the axial distance of interest, the jet diameter is approximately constant. Therefore, references to "larger jet height" should be interpreted to mean larger distortions of the jet cross section. Since the jet and solenoid field are cylindrically symmetric, it is hard to estimate in what direction the jet is going to be distorted but the ratio of the deflection can be determined experimentally. The ratio also can be compared with the transverse magnetic

pressure  $B^2/2\mu$  considering the reversed direction of deflection on each plot. If then, the Fig. 4.7 (a) gives the deflection ratio with magnetic field in an increasing sequence from 0 T to 15 T approximately consistent with the ratio of magnetic pressure  $B^2/2\mu$ .

As expected, jet motion in a magnetic field behaves differently, depending on the angle between the axis of magnet and the axis of jet, as a result of the differences in the magnitude of components of magnetic field (Samulyak, 2006). Fig. 4.6(a) and 4.6(b) show the axial and radial components of the magnetic field in a solenoid. Fig. 4.6(c) and 4.6(d) show the transverse and longitudinal components of the magnetic field along the jet axis at different crossing angles. As the crossing angle increases, the transverse component of the magnetic field increases, but with no significant change in the longitudinal component of the magnetic field. An increase of the transverse component of the magnetic field raises the induced axial current on the Hg jet. Therefore, the angle of the Hg jet is launched at 33 milliradian with respect to the axis of solenoid magnet.

The jet surface can readily be extracted from each collected image. The jet axis is approximated by fitting the averaged positions between top surface and bottom surface. This jet axis is moved with an offset until it interferes the top surface bottom surface. The amount of fluctuations of surface is measured by getting the difference between the fluctuation surfaces and the interfering jet axis on a RMS scale. Let  $\delta(r, t)$  denotes the probability of turbulence at  $r$ , such that  $\delta$  is 0 in the non-turbulent fluid, where the background is considered

here, and is 1 in the turbulent fluid, where the jet is considered here. Time average of  $\delta$  yields  $\zeta(r)$ , the intermittency factor at  $r$ . The turbulent fluctuations are produced by the intermittency effect and these fluctuations are significant for scalar quantities. The intermittency characteristics of the turbulence are the appropriate input to be used in defining rough surface for a scattering analysis. When the intermittency phenomenon is present, the conventional turbulent fluctuation is modified by the intermittency function and there is an additional contribution depending on the difference between the mean turbulent quantity and the non-turbulent quantity (Yen, 1967). However, the probability of the fluctuating jet surface area is introduced to define the intermittency in the following work. The pixel information along the jet axis by changing the translational offset is added to represent the intermittency of jet on the top/bottom surface. The intermittency within the jet represents 1 and it is gradually decrease to 0 at the background. The intermittency is between 0 and 1 at the jet surface depending on the surface fluctuations. Fig. 4.9 show the intermittency as a function of magnetic field and time. Total evaluated time is  $160 \mu s$ . Without magnetic field, the slope of intermittency at the jet surface is broad and it is oscillating as a function of time. With higher magnetic field, the slope of intermittency at the jet surface is more steep and it keeps same shape with respect to time. This result clearly tells that the magnetic field suppresses the fluctuation of jet surface.

The Fig. 4.10 shows the measured fluctuations on the jet surface. Surface fluctuations is monotonically decreasing and the surface is flattened approx-

imately at 5 T. The fluctuations at Viewport 3 (downstream) is larger than that at Viewport 1 (upstream) since the tendency to be more turbulent grows. The amount of fluctuations at top surface and bottom surface of jet is almost same, though the magnetic field is varied. Thus, the symmetry on the jet surface in terms of the surface variations such as fluctuations and wave amplitude is valid. The amount of difference of surface fluctuations at Viewport 1 and Viewport 3 becomes same. It indicates that the jet surface becomes flattened at 5 T in flow velocity 15 m/s. The decreased amount of surface fluctuation at Viewport 1 and Viewport 3 is  $\sim 0.5$  and 1.5 mm RMS respectively. This explains why the jet height is reducing from 0 T to 5 T in Fig. 4.7 (a). The magnetic field makes the wavelength on the jet surface increases. Correspondingly, the wave propagation speed is increasing. Thus, it causes  $Re_{cr}$  to increase and the flow becomes laminar due to the stabilization by the magnetic field. The transverse component of magnetic field prevails more over the jet stabilization. Though there is some measurement errors due to the saturation in image brightness, the measurement could show the field effect to the reduction of fluctuation on jet surfaces.

The these observations are supported by previous results. For example, several investigations have suggested that magnetic field suppresses turbulent fluctuations in conducting liquid by stabilizing the flow (Shercliff 1956, Gold 1962, Kozyrev 1981, Bernshtam 1982), where stabilization is judged by an increase in the characteristic wavelength of the flow.

### 4.2.2 Trajectory of mercury jet projectile in magnetic field

The Hg jet and the beam are launched at 33 and 67 milliradian with respect to the magnetic axis respectively. The trajectory of Hg jet projectile is acted upon by gravity, which is represented as follow:

$$t = \frac{x}{v_o \cos \theta} ,$$

$$y = -\frac{g}{2} t^2 + v_o \sin \theta t + y_{nozzle} , \quad (4.2)$$

where  $x$  is the jet traveling distance,  $y$  is the height at  $x$ ,  $y_{nozzle}$  is the vertical position of nozzle,  $v_o$  is the launched velocity, and  $\theta$  is the launched angle of Hg jet.

The distance of jet elevation is determined by measuring the distance from the magnetic axis at center of each window to the jet axis, which is approximated by fitting the averaged positions between top surface and bottom surface. The Fig. 4.11 shows the trajectory of Hg jet and it's effect by the magnetic field and gravity. Experiment shows that the trajectory of the Hg jet is parabolic. The magnetic field caused some elevation of Hg jet closer to the center of magnetic field. As the jet moves to downstream, magnetic field effect is more clearly shown up since the jet is more likely to elongate to the axial direction. The longitudinal magnetic force is more increasing as one can see the magnetic pressure term in the longitudinal direction increasing at Eqn. (2.67). Therefore, it is observed that the jet is behaving more like straight at Viewport 4 with higher magnetic field. At 15 T, the elevation of jet is observed from Viewport 1 to Viewport 4. It shows that the magnetic force is overcoming the

inertia force at 15 T similarly as there is the increase in jet height at 15 T. The overall increase of the jet elevation in upstream, midstream, and downstream at 15 T may have been caused by the change of jet height.

The jet trajectory is approximated by doing global fitting using simplex method, where multiple datasets in Fig. 4.11 are simultaneously fit while nozzle position and jet angle between datasets. For each shared global parameter, one best fit values that is estimated from all the datasets are derived. For each non-shared parameter such as jet velocity, unique best fit value for each individual dataset is derived.

Table 4.3 gives the estimated values of the nozzle position, launched jet angle, and the jet velocity in various magnetic fields. The estimated jet velocity increases as the magnetic field increases, though the effect of magnetic field to the change of jet flow velocity is within tolerance of fitting. The designed values of nozzle offset, nozzle angle, and jet velocity are 14.4 mm, 33 milliradian, and 15 m/s(20 m/s) respectively. The estimated values of jet trajectory by fitting the dataset given in Table 4.3 are consistent within tolerance of fitting.

The beam trajectory is also given to show the overlap with the Hg jet. It is shown that the overlap length is  $\sim 30$  cm when we consider the height of jet at various position with various magnetic field.

Based on the result of the jet trajectory, the angle of jet axis at Viewport 2 (midstream) is determined by the trigonometric approach using the elevation of jet and the distance along the magnetic axis between Viewport 1 and Viewport 3. Fig. 4.12 shows the estimation of jet angle at center of magnetic axis

(Viewport 2), which is approximately  $7 \sim 11$  milliradian. The jet angle is slightly decreasing with higher magnetic field, which indicates that the jet is more likely to move horizontally following the field line direction.

### **4.2.3 Pressure loss and magnetic effect to the Hg delivery pipe**

Fig. 4.13 (a) and 4.13 (b) show the pipe inlet pressure for driving jet in various magnetic field strength. The Hg jet is driven by the piston in syringe and the piston velocity is measured by position sensor. The piston velocity determines the flow rate so that the dynamic pressure head at pipe inlet is determined using the conservation of flow rate. The pressure sensor installed at the pipe wall measures the static pressure. No significant pressure drop is observed at the pipe inlet in magnetic field strength. It indicates that the driving pressure in pipe for nozzle is at same condition regardless of the magnetic field variation.

To obtain the jet velocity, the distance traveled by a fixed point on the jet surface is tracked over a given time period. Fig. 4.14 shows the jet velocity measured at Viewport 1, Viewport 2, Viewport 3, and Viewport 4 in various magnetic field strength. Note that this velocity does not change with the imposition of a magnetic field. This explains why the pressure is approximately constant in the pipe, consistent with the report (Graves, 2007).

Another interesting result is that the cross section of Hg jet is more likely to be elliptical since the longitudinal jet flow velocity is constant from upstream

to downstream. Regardless of the magnetic field, the Hg jet does not show jet velocity change. Thus, the jet is changing its shape once it leaves the nozzle from circular to elliptical. Hence, the result in Fig. 4.7 (a) should be again interpreted by the result in Fig. 4.14 in the manner that the jet height at 5 T is elongated on the minor axis followed by the reduction of jet height on the major axis of the elliptical core, and the jet is deflecting further at 10 T. However, the jet height at 15 T is elongated on the major axis, which is manifested by the comparison between the ratio of the reduction of jet height and the increased ratio of the jet height at 15 T. This approach is already mentioned in the above, but it is examined again.

Considering that the driving pressure and the jet velocity are not significantly changed in various magnetic field, it is concluded that the longitudinal magnetic field does not affect to the pressure loss or velocity degradation while Hg passes the solenoid magnet two times along with the direction of magnetic field line. It is reported that the gradient of longitudinal jet velocity depends on the integration of gradient of longitudinal magnetic field along the magnetic axis plus it's multiplication to longitudinal magnetic field itself. (Gallardo *etal*, 2002) It is expressed as follow:

$$\Delta v(x) = \frac{\kappa r_o^2}{\rho 8} \left( \int_{x_1}^{x_2} \left( \frac{dB_x}{dx} \right)^2 + \frac{d}{dx} \left( B_x \frac{dB_x}{dx} \right) dx \right), \quad (4.3)$$

where  $r_o$  is the radius of jet and  $\kappa$  is electrical conductivity. Since the gradient of magnetic field is increasing (plus) at entrance and decreasing (minus) at exit, it seems that there is an increasing velocity gradient (acceleration) at upstream and decreasing velocity gradient (deceleration) at downstream but



it is  $\leq 0.5$  m/s due to the relatively high density comparing with the electrical conductivity only if we consider the effect by the magnetic field. The experimental result shows slight effect of magnetic field but is consistent with the reported result in terms of the gradient of longitudinal velocity in magnetic field.

#### 4.2.3.1 *pressure loss in pipe flow*

Schematic pipe geometry is given in Fig. 1.3, where the pipe is connected from the syringe pump to nozzle and it is passing parallel with solenoid magnetic field line next to the primary containment. A loss coefficient is defined as follows:

$$(h_{loss}) = K_1 \frac{v_1^2}{2g} + K_2 \frac{v_2^2}{2g} + \dots + K_N \frac{v_N^2}{2g} ,$$

$$A_1 v_1 = A_2 v_2 = \dots = A_N v_N = A_R v_R , \quad (4.4)$$

where the subscript R signifies a reference location and K represents the loss coefficient.

The general thermodynamic loss, so called the head loss  $h_{loss}$  is defined as follow:

$$\int_1^2 \delta F = (h_{loss})_{1,2} = \frac{p_1 - p_2}{\rho g} + \frac{v_1^2 - v_2^2}{2g} + (z_1 - z_2) . \quad (4.5)$$

Darcy-Weisbach equation is given to express the head loss of wherever the density is constant, when the pipe diameter is constant and the pipe is horizontal.

$$\frac{\Delta p}{\rho g} = f \frac{L}{d} \frac{U^2}{2g} , \quad (4.6)$$

where  $f$ ,  $L$ ,  $d$  are friction factor, the pipe length, and the diameter of pipe respectively. Considering that the  $Re = 1800000$  and  $e/d = 0.002$  for commercial steel in terms of Nikuradse's sand grain scale, turbulent friction factor  $f$  via Moody plot or by Colebrook Eqn. (4.7) is approximated to 0.024. Colebrook simply combined the expressions for the friction factor for smooth and rough pipes into a single transition equation of the equivalent form.

$$\frac{1}{\sqrt{f}} = 1.74 - 2 \log \left( 2 \frac{e}{d} + \frac{18.7}{Re\sqrt{f}} \right) . \quad (4.7)$$

Note that Colebrook's expressions for the friction factor in the transition region reduces to Prandtl's smooth pipe equations when the relative roughness approaches zero, and reduce to von Karman's fully rough pipe equation at very high pipe Reynolds number.

The loss coefficients for elbows are presented as follows, where  $a$  and  $R$  represent the inside radius of the elbow and the radius of curvature of the centerline of the elbow respectively. For  $Re(a/R)^2 > 91$ , the loss coefficient is expressed as follow (Ito, 1960):

$$K_{elbow} = 0.00241 \alpha \theta \left( \frac{R}{a} \right)^{0.84} Re^{-0.17} , \quad (4.8)$$

where  $\theta$  is the bend angle in degrees and  $\alpha$  is an empirical factor given by Ito as,

$$\alpha_{\theta=90^\circ} = 0.95 + 17.2 \left( \frac{R}{a} \right)^{-1.96} . \quad (4.9)$$

Inputting  $R = 1.942$  and  $a = 0.442$ ,  $\alpha = 1.9$  and  $K_{elbow} = 0.1232$ .

A correction term is applied to the  $90^\circ$  elbow to determine the loss coeffi-

cient for arbitrary angle of elbow (SAE, 1960).

$$K_{\theta} = (C_{\theta})_{elbow} K_{90^{\circ}} , \quad (4.10)$$

where  $C_{elbow}$  is given in the referenced manual (SAE, 1960). The  $C_{\theta}$  is 0.28 at  $\theta = 23^{\circ}$  and  $K_{\theta} = 0.0345$ .

The loss coefficient for the reducer or well-rounded inlet loss is  $K_{reducer} = 0.05$  based on the flow area of the smaller piping section (Benedict, 1980).

The loss coefficient for the abrupt enlargement is determined by combining the momentum balance over the area of interest. Then, it yields the Carnot-Borda equation, which shows the head loss in the abrupt enlargement. By equating it to the head loss equation Eqn. (4.4), the loss coefficient is given based on the inlet velocity as follow:

$$K_{enlargement} = \left(1 - \frac{v_2}{v_1}\right)^2 = \left(1 - \frac{A_1}{A_2}\right)^2 = (1 - \beta^2)^2 ,$$

$$\frac{p_1}{p_2} = 1 + \left(\frac{1 - G_1}{G_1}\right)(2\beta^2 - 2\beta^4) , \quad (4.11)$$

where  $G_1$  is the inlet pressure ratio of static pressure to total pressure,  $p_t/p_{t1}$ . The fluid experiences pressure loss when going from a piping system to a plenum, so called exit loss. According to Eqn. (4.11), the loss coefficient for exit  $K_{exit}$  is 1, where  $\beta = 0$ . It applies regardless of whether the pipe protrudes into the exit plenum, is well rounded at exit, or is flush.

Finally, the loss coefficient for the abrupt contraction is given based on the

velocity at exit as follow (Benedict, 1980):

$$K_{contraction} = \left(\frac{1}{C_D^2} - 1\right)(1 - \beta^4) ,$$

$$C_D = \frac{Q_{acutal}}{Q_{ideal}} , \quad (4.12)$$

where the discharge coefficient  $C_D$  is given in reference (Benedict, 1980). The mean discharge coefficient is given as 0.815 based on the water tests in short pipes. According to Eqn. (4.12), this yields a maximum loss coefficient at  $\beta = 0$  of 0.506. Assuming  $\beta = A_2/A_1 = 0.9$ ,  $K_{contraction}$  yields 0.1738.

The head losses and the contribution of each geometry are given in Table 4.1. Total length of pipe is 87.1 inch. The diameter of inside pipe is 0.884 inch. The diameter of inside nozzle is 0.4 inch. Total pressure head loss is 4.5344 m., which corresponds to  $\sim 30$  % of input pressure head. The main loss is caused by the exit from nozzle, which is over  $\sim 50$  %. The following loss is caused by the friction due to the large length, which is  $\sim 27$  %. The loss from pipe bend is somewhat low comparing with others.

Based on the calculated head loss, the jet velocity at nozzle is determined assuming the pressure right after the nozzle is atmospheric. The pipe inlet pressure is given in Fig. 4.13 (a) and 4.13 (b). The elevation of the pipe inlet and the nozzle is 2.9 inch. The calculated jet velocity from nozzle including the pressure loss in pipe is 13.4 m/s, which is consistent with the measured result in Fig. 4.14 where the jet velocity is  $\sim 13.5$  m/s. According to Eqn. (2.67), the magnetic field increases the fluid pressure by an amount  $B^2/2\mu$ , in directions perpendicular to the magnetic field, and decreases the fluid pressure by the

same amount, in the parallel direction of the magnetic field. The fluid pressure including the magnetic pressure has to balance with the atmospheric pressure and surface tension of jet and satisfy the continuity condition. The fluid pressure will find equilibrium point since the fluid pressure perpendicular to the magnetic field line is mutually symmetric. Therefore, the jet is changing to be elliptical in Fig. 4.7 (a). Hence, the pressure drop is not occurred significantly and correspondingly the longitudinal jet velocity is not changed with magnetic field in Fig. 4.14.

#### 4.2.3.2 *the measurement of wall tap pressure*

Wall taps is used in order to sense static pressure, wherein small pressure taps are located at a point on such surface as cylindrical pipe so that it does not disturb the fluid. Tap size error arises because of a local disturbances of the boundary layer.

$$\begin{aligned} \text{Re}_d^* &= \frac{v^* d_{tap}}{\nu} , \\ \text{Re}_d^* &= \sqrt{\frac{f}{8}} \left( \frac{d_{tap}}{d} \right) \text{Re} , \end{aligned} \quad (4.13)$$

where  $d_{tap}$  is the tap diameter,  $\text{Re}_d^*$  is the tap Re number, and  $v^*$  is the friction velocity. The friction factor is 0.024. The tap inside diameter and pipe inside diameter are 0.5, 0.884 inch respectively, which yields  $\text{Re}_d^* = 55764$ .

At tap Re greater than 385, the error in static pressure caused by the tap size is given as follow:

$$\frac{e_{tap}}{\tau} = 0.269 (\text{Re}_d^*)^{0.353} , \quad (4.14)$$

where  $\frac{e_{tap}}{\tau} = 12.74$ .

Combining the Darcy friction factor with the wall shear stress yields

$$f = 4 \left( \frac{\tau}{\rho v^2 / 2g} \right) . \quad (4.15)$$

Therefore, the error in a static pressure can be expressed as non-dimensionalized form by the dynamic pressure  $p_{dynamic}$ .

$$\frac{e_{tap}}{p_{dynamic}} = \left( \frac{e_{tap}}{\tau} \right) \frac{f}{4} , \quad (4.16)$$

where  $\frac{e_{tap}}{p_{dynamic}} = 0.0764$ . The error of static pressure in Fig. 4.13 (a) is estimated to give 7.64 % uncertainty of the dynamic pressure in Fig. 4.13 (b).

## 4.3 Interaction of an Intense Proton Beam with the Hg Jet in a Magnetic Field

### 4.3.1 Proton Beam dynamics

Neutrino factories require a large number of muons, which are obtained from the decay of pions. Efficient production of pions can be achieved by colliding an intense proton beam with a high-Z target. An important consideration is the problem of removing the power deposited by the proton beam without interfering with the process of extracting the end-product, which is the muon beam. When the proton beam energy reaches approximately 100 kJ/pulse, the heat from the beam could melt or crack a stationary solid high-Z target. The response of a liquid target in a high-magnetic induction field will have beam energy effects, which is investigated experimentally. Experiments

on the interaction of a 14 GeV/c and 24 GeV/c proton beam with pulse structures of 4 to 16 bunches per pulse and the spot sizes in the order of 2 to 3  $mm^2$  RMS up to 30 tera-protons(TP) per pulse in magnetic field up to 15 T has been carried out at CERN. Fig. 4.15 (a) shows the infrastructures for experiment at CERN. All equipments for experiment are installed at tunnel TT2/TT2A and these are controlled remotely at control room. The proton beam is delivered from proton synchrotron ring and the beam setup is shown in Fig. 4.15 (b). The PS machine is set up in harmonic 16 bunches and the extracted protons fills the machine in bunch pairs. Each bunch has 131.25 ns time delay. The proton beam pulse structure of harmonic 8 and harmonic 16 in 14 GeV, 6 TP is shown in Fig. 4.21. A bunch in harmonic 8 mode is consisted of a bunch pair. Therefore, a bunch period in harmonic 8 mode is two times of a bunch period in harmonic 16 mode. Each bunch can fill protons up to  $2.5 \times 10^{12}$ . Therefore, the maximum beam intensity can be achieved up to  $32 \times 10^{12}$  protons.

Fig. 4.16 shows the layout of tunnel at CERN, where equipments for experiment are installed. Electronic equipments for optical diagnostics, hydraulic power unit, and cryogenic system are positioned at tunnel TT2. Hg loop system, solenoid magnet, and beam diagnostic system are positioned at tunnel TT2A. The fibers for optical diagnostics of Hg target in solenoid magnet and cables for controlling the Hg loop system and solenoid magnet are connected between TT2 and TT2A passing through an artificially drilled hole.

#### 4.3.1.1 *pulse structure*

In order to produce the design number of  $10^{21} \text{muons/year}$  in the muon storage ring, 4MW of proton beam power is desired. For our experiment, the CERN PS ran typically in a harmonic 16 mode. Hence, it is possible to fill with  $2 \times 10^{12}$  protons/bunch and therefore up to  $32 \times 10^{12}$  protons/spill. One beam pulse consists of several beam bunches. The bunch width is 50ns and the bunch-to-bunch difference is multiples of 131.25ns.

The beam spot size at the target is related to the target size to maximize the pion yield. About  $3 \sigma$  of the beam should be within the target. The spot size at the experiment is in the order of 2 to 3  $\text{mm}^2$  RMS. This allows to place up to  $32 \times 10^{12}$  protons on the mercury target, generating a peak energy deposition of 150J/g.

Power consumption is dominated by the repetition rate. Thus, the capability to replace the disrupted jet determines the ultimate beam power. The optimal interaction length for the 24 GeV beam energy is in the region of 30 cm which corresponds to approximately 2 interaction length for mercury (Kirk *et al*, 2008). For a 20 m/s jet velocity, replacing two interaction lengths will be taken in 14 ms thus allowing for operations with a repetition rate of up to 70 Hz. The beam energy per pulse is 115 kJ for a beam of  $30 \times 10^{12}$  protons with 24 GeV beam energy. The disruption length at  $30 \times 10^{12}$  protons with 24 GeV beam energy in a magnetic field of 15 T is less than 20 cm at 24 GeV beam energy in Fig. 4.24, thus preserving the 70 Hz beam repetition rate option. It yields the key result that a target system capable of supporting proton beams



with powers of up to 8 MW (Kirk *et al*, 2008).

#### **4.3.1.2 *proton beam characteristics***

Table 4.2 shows the proton beam characteristics with respect to the beam energy. The proton beam with 14 GeV and 24 GeV beam energy is employed in the experiment. As the proton beam energy increases from 14 GeV to 24 GeV, it is reported (Efthymiopoulos, 2008) that the beam spot size increases followed by the horizontal length decrease by half and the energy deposition density is 80 and 160  $J/g$  at  $30 \times 10^{12}$  protons, respectively.

### **4.3.2 Mechanism of the interaction and the Hg jet response to the energy deposition by the proton beam**

#### **4.3.2.1 *Hg jet pressurization by energy deposition of proton beam***

The target material is mercury, whose  $\rho$  is  $13.6 \text{ g/cm}^3$ . The density of the energy deposition  $E_{dep}$  due to ionization losses of the protons is  $\sim 33 \text{ J/g}$ . Additional ionization due to secondary particles from interactions of the protons in the target raises this to a peak of  $\sim 100 \text{ J/g}$  at 10 cm into the target (McDonald, 2000). The energy deposition,  $E_{dep}$ , leads to peak pressure  $P$  that can be estimated as follow:

$$P \approx \frac{\alpha_v K E_{dep}}{c_p}, \quad (4.17)$$

where  $\alpha_v$  is the thermal volumetric expansion coefficient, which corresponds to 3 times of thermal linear expansion coefficient,  $K$  is the bulk modulus,  $E_{dep}$

is the energy deposition, and  $c_p$  is the specific heat capacity. For mercury,  $\alpha_v = 180 \times 10^{-6}/K$ ,  $E_v = 25 GPa$ ,  $c_p = 138 J/(K \text{ kg})$ . A peak value of  $E_{dep}=100 J/g$  corresponds to a peak stress of  $\sim 3000$  MPa. The mercury target will be disrupted by the proton beam, leading to a breakup into droplets.

#### 4.3.2.2 *typical beam-jet interaction in magnetic field*

Fig. 4.17 is the photographs of the Hg jet interaction with a 16 TP, 14 GeV/c proton beam at 5 T captured at Viewport 3 at a 500  $\mu s$  frame rate, which shows clearly how the Hg jet is responding from the sudden energy deposition by the proton beam. The beam hits the Hg jet at the bottom surface, passing through the center of jet at Viewport 2, leaving the Hg jet on the top surface. The captured photos show the response of the Hg jet upstream, midstream, and downstream. There are filaments on the top surface of jet downstream, where the beam is leaving, and on the bottom surface of the jet upstream, where the proton beam is hitting, entering the target. The jet break up voids midstream where the beam is passing through.

Fig. 4.18 and 4.19 are representing the distribution of energy deposition density to Hg jet by 14 GeV/c and 24 GeV/c proton beam in 0 T respectively, which is calculated using MARS code (Striganov, 2008). The employed spot size is 1.6 mm RMS. The energy density distribution is plotted depending on the radial position of target from jet center. Therefore, the peak of energy density exists respectively depending on the radial position in analysis. It shows that the maximum energy deposition density is obtained at the bottom

surface of jet at  $\sim 13$  cm from the center of magnet, where is actually Viewport 1, and the peak energy deposition density moves to the center of the Hg jet followed by the larger energy deposition density is located at the top surface of the Hg jet. The peak energy deposition density is moving corresponding to the beam crossing trajectory in Hg jet. The most dense energy deposition is distributed at the center of Hg jet between upstream and midstream, where the Hg jet breaks. The collected photos in Fig. 4.17 clearly supports these simulation results.

### **4.3.3 Hg jet disruption and magnetic suppression of the disruption**

The disruption length is determined by counting the number of frames at Viewport 3 where the complete disruption of the jet is observed. The time delay between Viewport 2 and Viewport 3 is 10 ms. Thus, the disruption generated at Viewport 2 by the beam could be observed at Viewport 3 after 10 ms, where the jet is moving with a velocity of 15 m/s. Each image is separated into 10 segments vertically in order to locate the position of disruption. Thus, the accuracy of the measurement to define the location of starting(ending) disruption in measurement could be increased. The disruption length is given by multiplying the frame rate by the counted number of images and investigated with the beam energy, beam intensity, and magnetic field. 230 events out of 360 beam shots are evaluated for the disruption length. About 130 events out of 360 beam shots are evaluated for the detection of particles without Hg

jet. Thus, the images for these events are not collected. Fig. 4.20 shows the standard deviation of the evaluated disruption lengths with respect to the disruption length. The solid line represents the curve fitted approximation of the reduced data distribution, where the line asymptote logarithmic. This curve fitted line is used for estimation of the standard deviation of the disruption length at respective disruption length. Correspondingly, the error bar is determined by dividing the the estimated standard deviation by the root square of the number of events  $N$  for each data point.

#### **4.3.3.1 *characteristics of beam structure in disruption length, harmonic 8 and 16***

The proton beam pulse structure of harmonic 8 and harmonic 16 in 14 GeV, 6 TP is shown in Fig. 4.21. Fig. 4.22 shows the dependence of the disruption length of the Hg jet on the proton beam pulse structure with a 14 GeV beam in 5 T. A pulse contains same total protons. Doubled bunches shows doubled disruption length. It indicates that the energy deposition by the collision of Hg and protons is same, but the disruption of Hg jet is more likely affected by the number of protons in each bunch and time difference in a pulse due to the different bunches, i.e, 8 bunches and 16 bunches, though there are same protons in a pulse. The disruption on the Hg jet surface disappears when the beam intensity is less than  $\sim 4$  TP in Fig. 4.23. The threshold of beam intensity is  $\sim 4$  TP at 14 GeV in 5 T. Fig. 4.22 also indicates that the harmonic 8 pulse structure can increase the threshold of disruption for a bunch of beam intensity. Considering that the different beam pulse structure

results in different disruption to Hg due to the time difference of bunches in a pulse structure, we consider only harmonic 16 pulse structure for the following experiment.

#### **4.3.3.2 *disruption length with 14 GeV proton beam***

Fig. 4.23 shows the disruption length with beam intensities up to 30 TP for a 14 GeV beam. According to Fig. 4.18, the peak energy deposition to Hg with 14 GeV/c beam energy at 30 TP is  $\sim 100$  J/g by changing the energy units, where the disruption length corresponds to  $\sim 23$  cm  $\pm$  5 cm for 10 T to  $\sim 18$  cm  $\pm$  5 cm for 15 T, respectively. The results show that the magnetic field suppresses the disruption length. At high intensities of beam, the disruption length appears to be approaching an asymptotic level. The magnetic field reduces effectively weak disruption such as the generation of the filaments on the jet surface. The threshold of the disruption for beam intensity is around 4 TP at 5 T and the magnetic field can increase it, though the effect is not clear in Fig. 4.23 due to the difficulty in quantifying and measuring the small amount of the disruption length.

#### **4.3.3.3 *disruption length with 24 GeV proton beam***

Fig. 4.24 shows the disruption length with the beam intensities up to 30 TP for a 24 GeV proton beam. According to Fig. 4.19, the peak energy deposition to Hg with 24 GeV/c beam energy at 30 TP is  $\sim 150$  J/g by converting the energy unit multiplied by the number of protons, where the disruption length corresponds to  $\sim 22$  cm  $\pm$  5 cm for 10 T to  $\sim 17$  cm  $\pm$  5 cm for

15 T, respectively. The results show that the magnetic field suppresses the disruption length. Unlike the 14 GeV/c beam energy, the magnetic field suppresses the disruption length over all of beam intensity. The disruption length appears to be approaching an asymptotic level. If there is no magnetic field, the disruptions are always generated by proton beam regardless of the beam intensities, though very weak disruptions on the Hg jet surface are observed with low beam intensities. The threshold of the disruption for beam intensity is  $\sim 2$  TP at 5 T but the higher magnetic field increases it.

#### ***4.3.3.4 validation of measurements of Viewport 3 through comparison with Viewport 4***

In order to validate measurements of the disruption length at Viewport 3, measurements of disruption lengths at Viewport 4 are also performed. Fig. 4.25 (a) shows the disruption length at Viewport 3 for 19 events with a harmonic 16 beam structure, 16 TP, 14 GeV beam energy in a 5 T. Fig. 4.25 (b) shows the disruption length at Viewport 4 for the same events. Fig. 4.25 (c) shows the difference of disruption length between Viewport 3 and Viewport 4 for the same events. The solid line represents the average and distribution of the disruption length difference. The difference of disruption length is  $\sim 2$  cm. The reason for the difference of the disruption length measurement between Viewport3 and Viewport 4 is mainly caused by the fluctuation of the proton beam and the Hg jet in a magnetic field. The reduction of surface instabilities by the presence of a static magnetic field is a consequence of magnetic damping. Also, surface structure is frozen by magnetic field. Therefore, the same disrupted shape on

the jet surface at Viewport 3 is observed at Viewport 4 without variation of the disruption length.

### 4.3.4 Damping of filaments in a magnetic field

#### 4.3.4.1 *triggering timing of high speed camera considering the electronic delay*

In order to investigate the time response of filaments, we need to establish the accuracy and calibration of the measurement based on the experimental settings. Fig. 4.26 shows the traced signals on an oscilloscope when the beam and the beam triggering are delivered. After the master trigger from the synchrotron is delivered at  $t = 0$ , the proton beam comes in  $\sim 3 \mu\text{s}$ . The photodiode response from scintillating fiber has a 20 ns rise time and the level indicates the beam intensity and beam position. The scintillating fiber signal gives the beam arrival time. Therefore, it is possible to set the trigger timing for the cameras and laser driver inputs, which is  $\sim 2 \mu\text{s}$  after the master trigger from the proton synchrotron.

So, the first image of the SMD camera tells the status of jet for the time before the beam arrives since the exposure time of SMD camera is 150 ns. All of the electronic delays including the cable delays are less than  $1 \mu\text{s}$ . The maximum frame rate of SMD camera is up to 1 MHz. The accuracy of camera frame rate is checked by using laser pulses. Laser pulses with certain periods are generated and then monitored at oscilloscope through photodiode. The frame rate of camera is set at the corresponding values of laser pulse period.

The frame rate is checked by monitoring the variation of intensity of image captured from camera, which is judged as negligibly uniform.

#### **4.3.4.2 *Onset of filamentation on the jet surface***

Fig. 4.27 show photographs of filament evolution on the Hg jet surface as a function of time at a  $25\ \mu\text{s}$  frame rate, where the beam is 10 TP, 24 GeV and the magnetic field is 10 T. To obtain the vertical filaments velocity, the distance traveled by a fixed point on the jet surface is tracked over a given time period, where the maximally displaced surface position is picked for filament velocity measurements. The jet volume, where the maximal energy is deposited, results in the initial generation of the filaments. The higher jet velocity occurs when the filaments is initially protruded out of the jet surface and then the jet velocity decreases due to the magnetic damping and viscous damping. So, the velocity at steady state is obtained in order to evaluate the relationship with the beam intensity and magnetic field.

#### **4.3.4.3 *filaments velocity with 14 GeV beam in a magnetic field***

Fig. 4.28 shows the filament velocity as a function of 14 GeV beam intensity and magnetic field. The filament velocity increases with the beam intensity. However, the magnetic field suppresses the filament velocity. At relatively low magnetic field of 5 T, the jet and/or the charged beam is fluctuating depending on the initial conditions at the time of experiment. Thus, there are distributions over the resulting data points. However, the data points for 10 and 15 T have less fluctuations. The slope of the data points at higher



magnetic fields are less than that associated with lower magnetic field. All velocities are less than 30 m/s regardless of the magnetic field. The filament velocity at 14 GeV, 20 TP, 10 T is  $\sim 13$  m/s.

#### ***4.3.4.4 filaments velocity with 24 GeV beam in a magnetic field***

Fig. 4.29 shows the filament velocity as a function of 24 GeV beam intensity and magnetic field. The filament velocity increases with the beam intensity. The slope of the increase is  $\sim 5 \times$  larger than that for the 14 GeV case, which indicates that unknown parameters such as beam spot size is affecting the energy deposition density since the ration of peak energy deposition is  $\sim 1.5$  at 0 T assuming the beam spot sizes for 14 GeV and 24 GeV are  $\sim 1.6$  mm RMS. However, the magnetic field suppresses the filament velocity. At relatively low magnetic field up to 5 T as in the 14 GeV case, the jet and/or the charged beam is unstably fluctuating depending on the event condition at the moment. Thus, there are distributions of the result data points. All velocities are less than 130 m/s regardless of the magnetic field and the filament velocity for the 24 GeV, 20 TP, 10 T case is  $\sim 70$  m/s.

#### ***4.3.4.5 delay of onset of filamentation and transient time response of filament in a magnetic field***

If a conducting liquid moves through a static magnetic field, electric currents are generated. This, in turn, leads to ohmic heating such as Joule dissipation. As the thermal energy of the fluid rises, there is a corresponding drop in its kinetic energy, and so the fluid decelerates. This results in a suppression

of the motion of liquid jets. Fig. 4.30 and 4.31 represent the time response of filament velocity as a function of magnetic field with 14 GeV, 20 TP beam and 24 GeV, 10 TP beam respectively.

According to P. A. Davidson's approximation (1999), the Eqn. (2.33) shows the energy decays with respect to time depending on the magnetic field, where  $\tau = \rho/\sigma B^2$ . This implication is that the filaments decelerates on a time scale of  $\tau$ . Fig. 4.32 shows the decay of the normalized energy of flow in magnetic fields with respect to time due to the magnetic damping. Higher magnetic field dissipates energy faster. Fig. 4.33 shows the integrated energy with respect to time. Thus, it represents the total energy of flow by the certain time.

Since the joule damping dissipates the energy with an exponential factor, the energy dissipation arises rapidly in the beginning depending on the magnetic field term  $B^2$ . Thus, higher magnetic field will have higher damping effect so that it takes more rising time. Therefore, the slope of rising velocity in Fig. 4.30 and 4.31 is different depending on the magnetic field proportional to  $B^2$  in exponential function. The integration of the energy with respect to time gives the total energy at a certain time. If we assume that the time required for the interaction between beam and mercury is  $50 \mu\text{s}$  with 24 GeV, 10 TP beam since the filament is coming out at that time from experiment without magnetic field, the time to be taken to reach the same amount of energy is  $\sim 130 \mu\text{s}$  at 15 T in Fig. 4.33. It is consistent with experimental measurement in Fig. 4.31. Also the field affects the suppression of kinetic energy. The effect will be larger from 10 T but it is small up to 5 T since it is proportional to

$B^2$  in exponential function. The time required for generation of filament at 5T with 14GeV energy is  $100\ \mu s$  from experiment in Fig. 4.30. Actually it will be less than  $100\ \mu s$  because we set the camera frame rate at  $100\ \mu s$  for this experiment. In this case, the first frame of images shows the filamentation on the Hg jet surface. The same amount of energy required to generate the filament at 5T ( $100\ \mu s$ ) is  $\sim 200\ \mu s$  at 15 T in Fig. 4.33. It is consistent with experimental measurement in Fig. 4.30. In Fig. 4.30, a event at 5 T shows lower velocity and it also shows the delay of onset of filament up to  $\sim 200\ \mu s$ . It shows again the relation of the delay of the onset and the required energy for onset.

Table 4.1: Pressure head losses by geometry in pipe for mercury loop.

Geometry in pipe for mercury loop	Calculated pressure head loss	Percentage in total pressure head loss (%)
Friction by surface roughness	1.2212	26.9
Elbows in pipe bend ( $3 \times 90^\circ$ , $2 \times 23^\circ$ )	0.2265	5
Reducer, Contraction in nozzle	0.5645	12.5
Nozzle exit	2.5222	55.6

Table 4.2: Characteristics of the proton beam (Efthymiopoulos, 2008).

Beam energy (GeV)	Horizontal length (mm)	Vertical length (mm)	Spot size ( $mm^2$ )	Energy deposition density (J/g at $30 \times 10^{12}$ protons)
14	4.45	0.87	12.18	80
24	2.94	0.66	6.13	160

Table 4.3: Estimated values of jet trajectory in magnetic fields.

Magnetic field (T)	Nozzle offset (mm)	Nozzle angle (milliradian)	Jet velocity (m/s)
0 T	$-14.5 \pm 1.0$	$33.8 \pm 3.8$	$13.6 \pm 0.9$
5 T	$-14.5 \pm 1.0$	$33.8 \pm 3.8$	$13.9 \pm 0.9$
10 T	$-14.5 \pm 1.0$	$33.8 \pm 3.8$	$14.1 \pm 1.0$
15 T	$-14.5 \pm 1.0$	$33.8 \pm 3.8$	$14.5 \pm 1.0$
15 T	$-14.5 \pm 1.0$	$33.8 \pm 3.8$	$18.9 \pm 2.3$

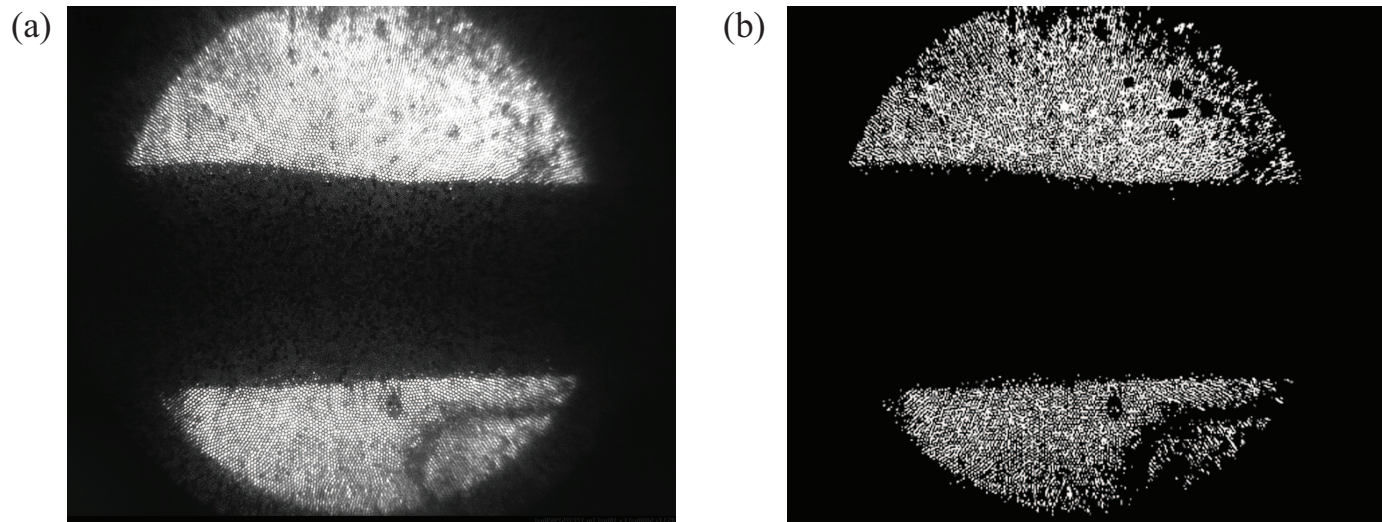


Figure 4.1: Image data conversion for image analysis. a.) Collected image data. b.) 2 bit scaled image data.

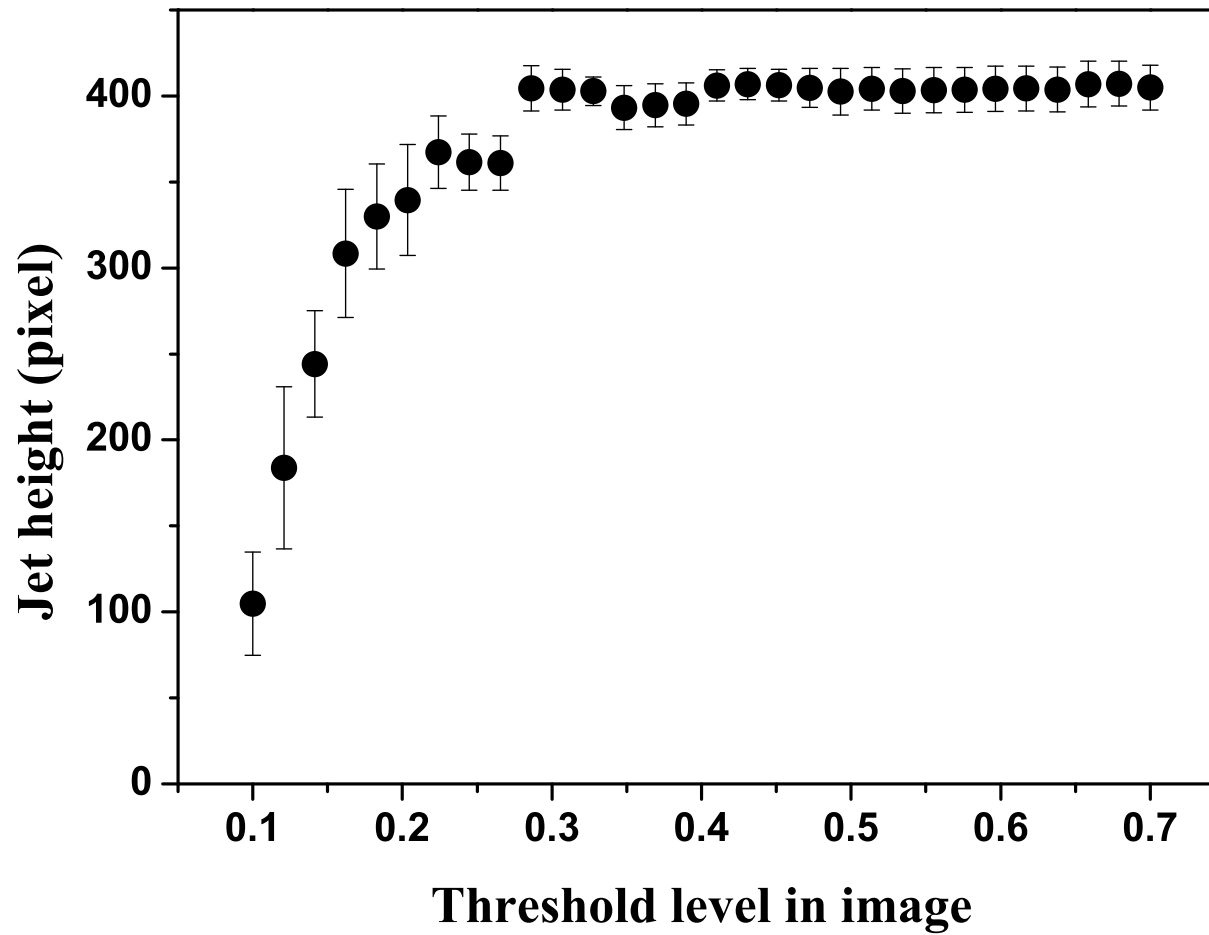


Figure 4.2: Sensitivity of threshold in a 2 bit scaled image conversion.



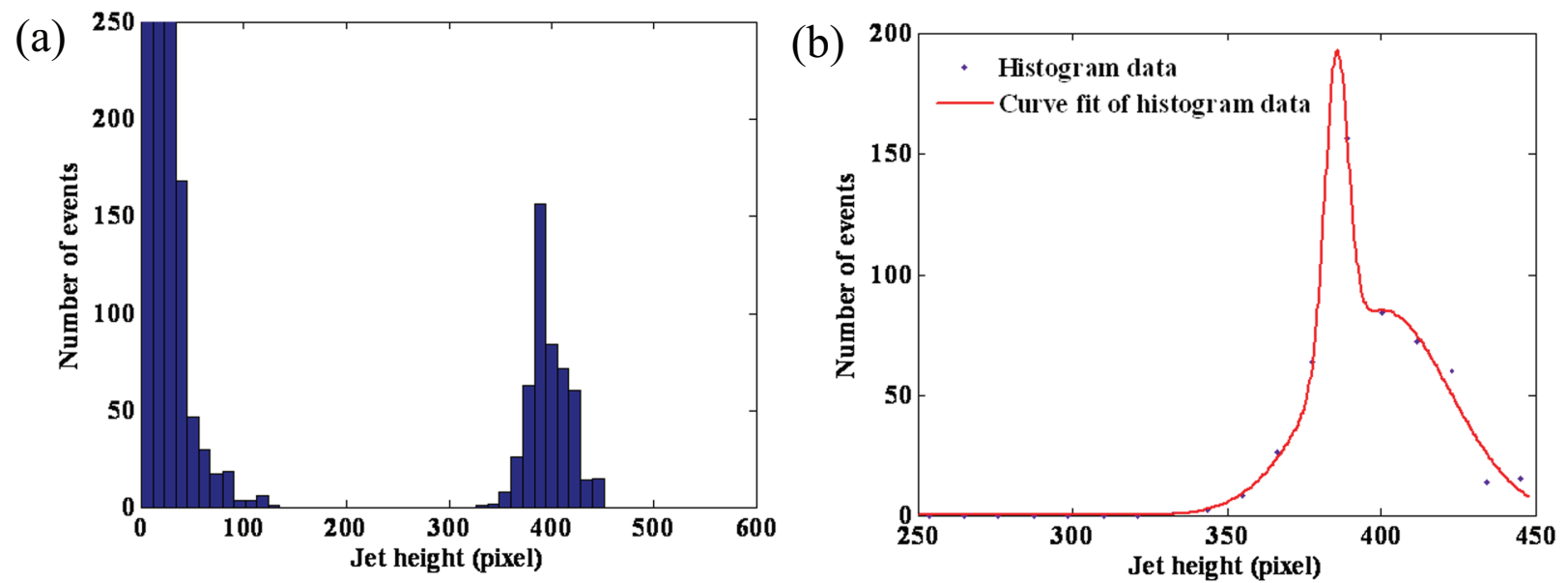


Figure 4.3: Jet height determination from image analysis. a.) Histogram of number of events in the jet height measurement. b.) Fitted histogram distribution.

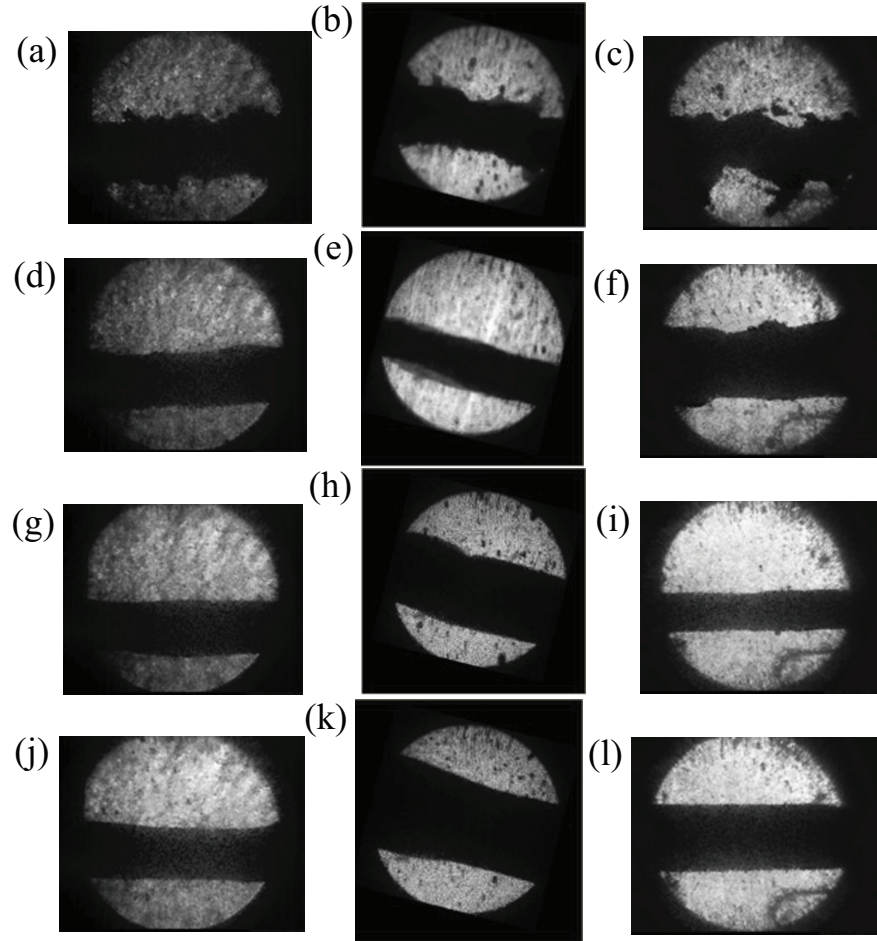


Figure 4.4: Mercury jet flows as observed from the 3 Viewports. The jet flows from left to right on each image. The first, second, and third columns represent Viewport 1, 2, and 3, respectively. The individual caption shows the applied magnetic induction field. The jet velocity is 15m/s. Images on Viewport 2 has a  $14^\circ$  clockwise rotation due to the SMD software. a.)  $B=0\text{T}$ . b.)  $B=0\text{T}$ . c.)  $B=0\text{T}$ . d.)  $B=5\text{T}$ . e.)  $B=5\text{T}$ . f.)  $B=5\text{T}$ . g.)  $B=10\text{T}$ . h.)  $B=10\text{T}$ . i.)  $B=10\text{T}$ . j.)  $B=15\text{T}$ . k.)  $B=15\text{T}$ . l.)  $B=15\text{T}$ .

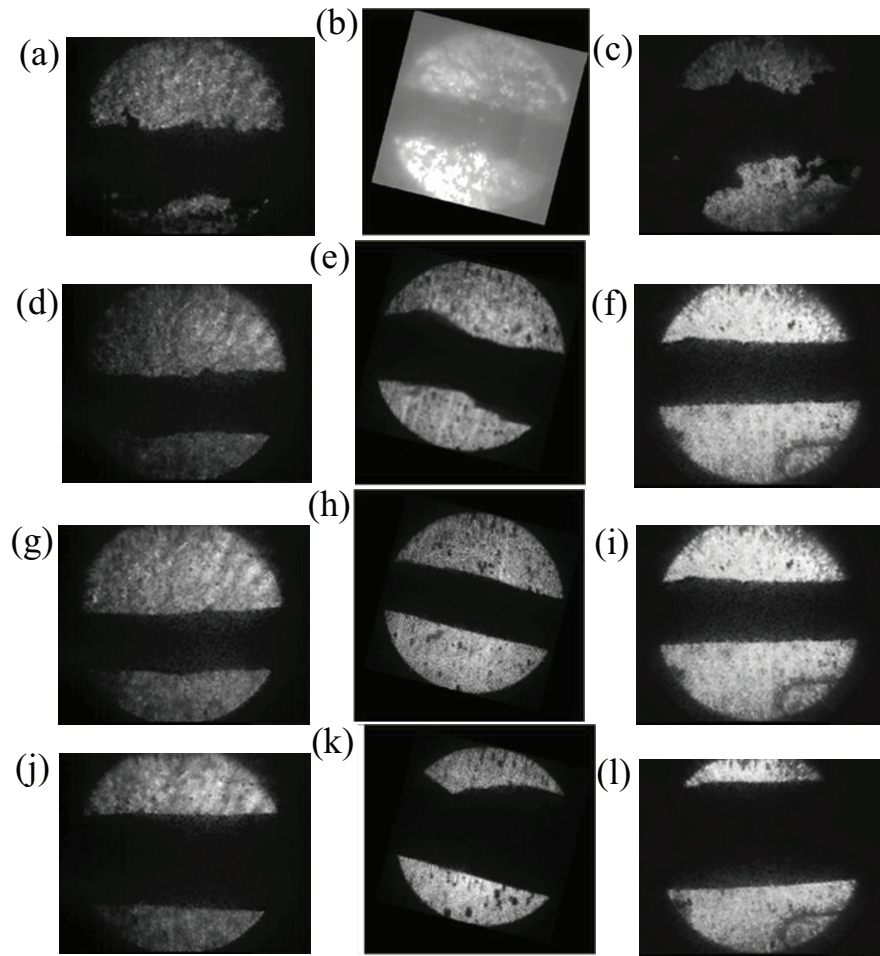


Figure 4.5: Same as Fig. 4.4 but with a jet velocity of 20 m/s. a.)  $B=0\text{T}$ . b.)  $B=0\text{T}$ . c.)  $B=0\text{T}$ . d.)  $B=5\text{T}$ . e.)  $B=5\text{T}$ . f.)  $B=5\text{T}$ . g.)  $B=10\text{T}$ . h.)  $B=10\text{T}$ . i.)  $B=10\text{T}$ . j.)  $B=15\text{T}$ . k.)  $B=15\text{T}$ . l.)  $B=15\text{T}$ .

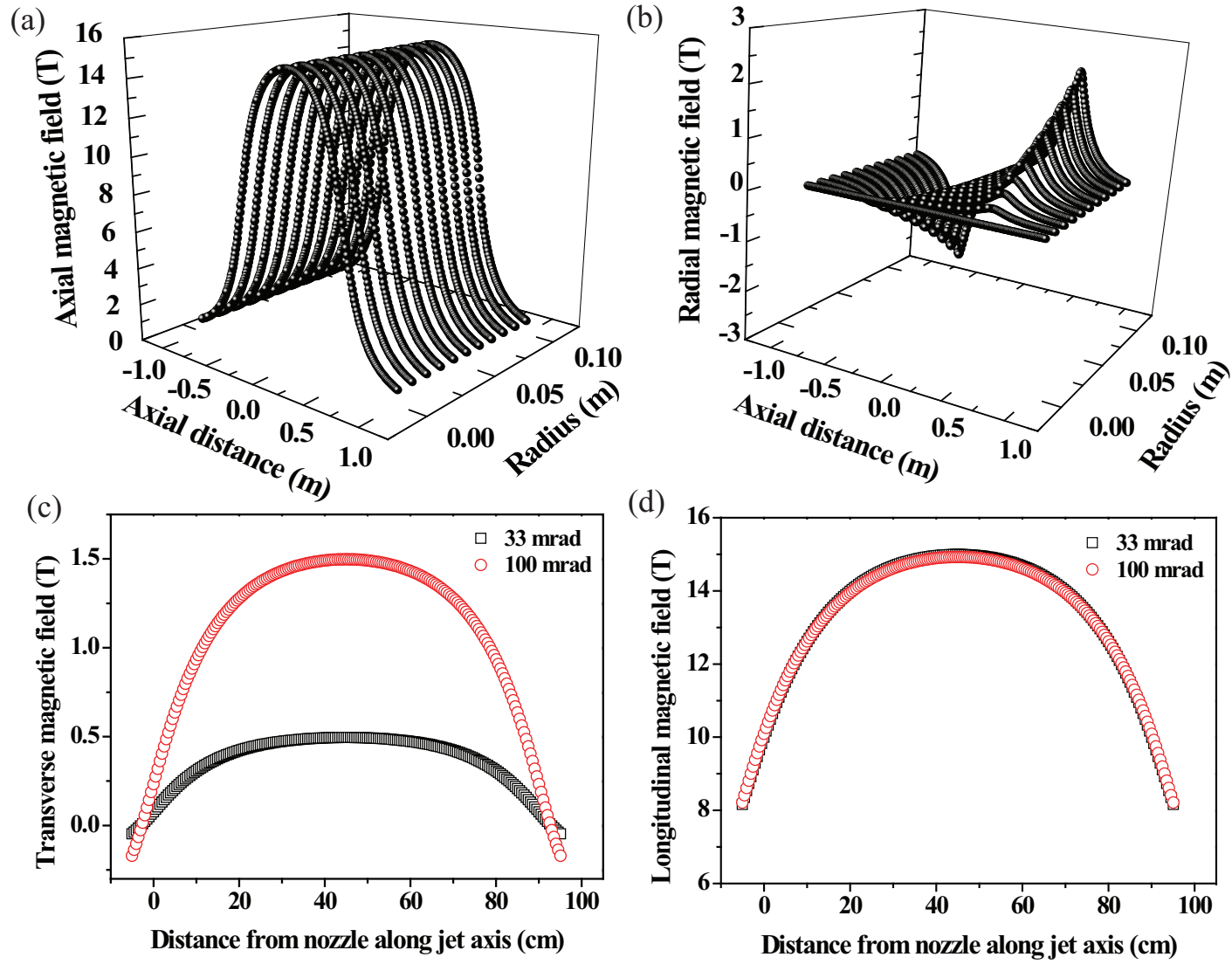


Figure 4.6: Calculated solenoid magnetic induction field map. a.) Radial field map. b.) Axial field map. c.) Transverse component of magnetic induction field along jet axis. d.) Longitudinal component of magnetic induction field along jet axis.

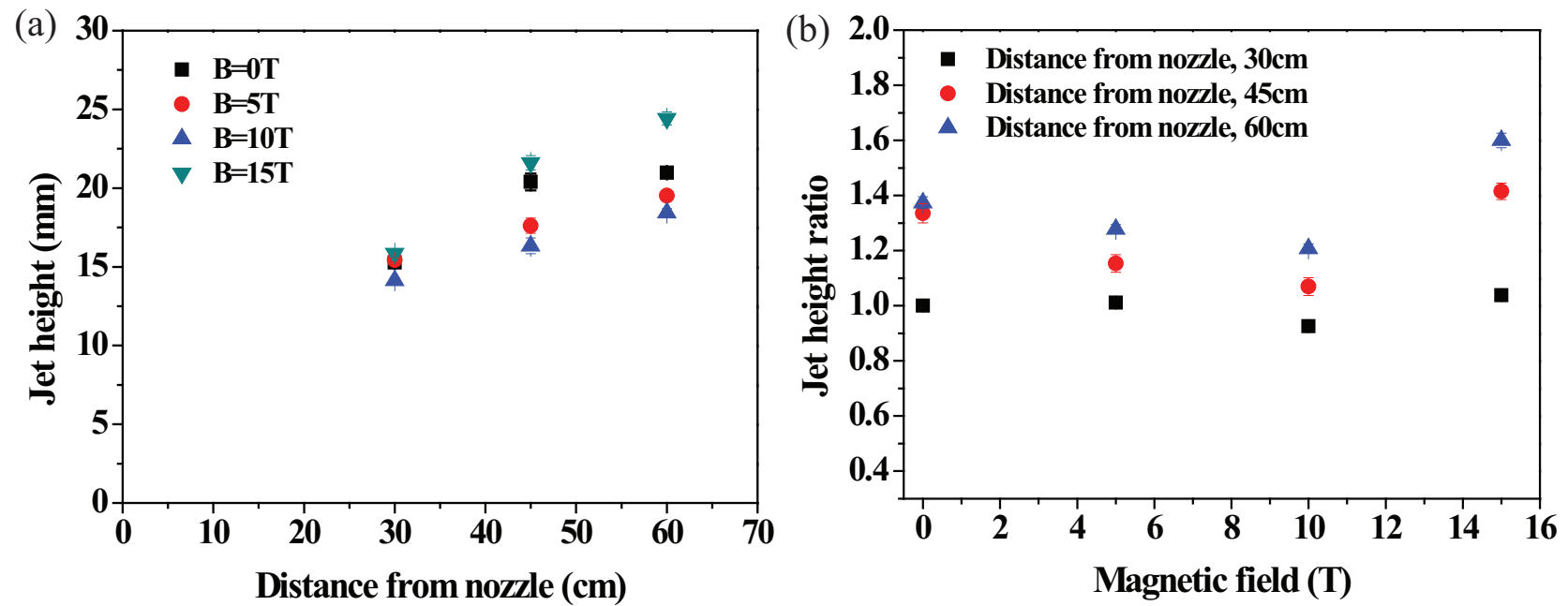


Figure 4.7: Hg jet height measurement in magnetic field by fitting estimation. a.) Jet height. b.) Jet height ratio.

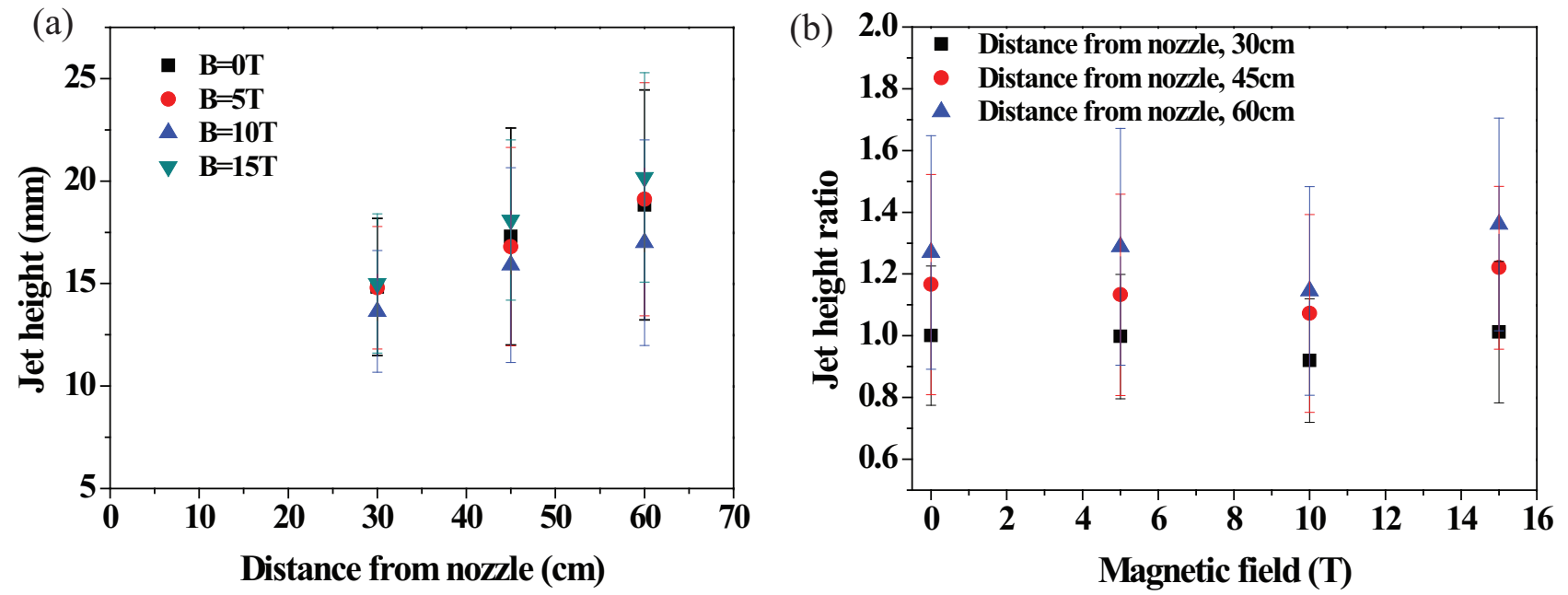


Figure 4.8: Hg jet height measurement in magnetic field by direct average. a.) Jet height. b.) Jet height ratio.



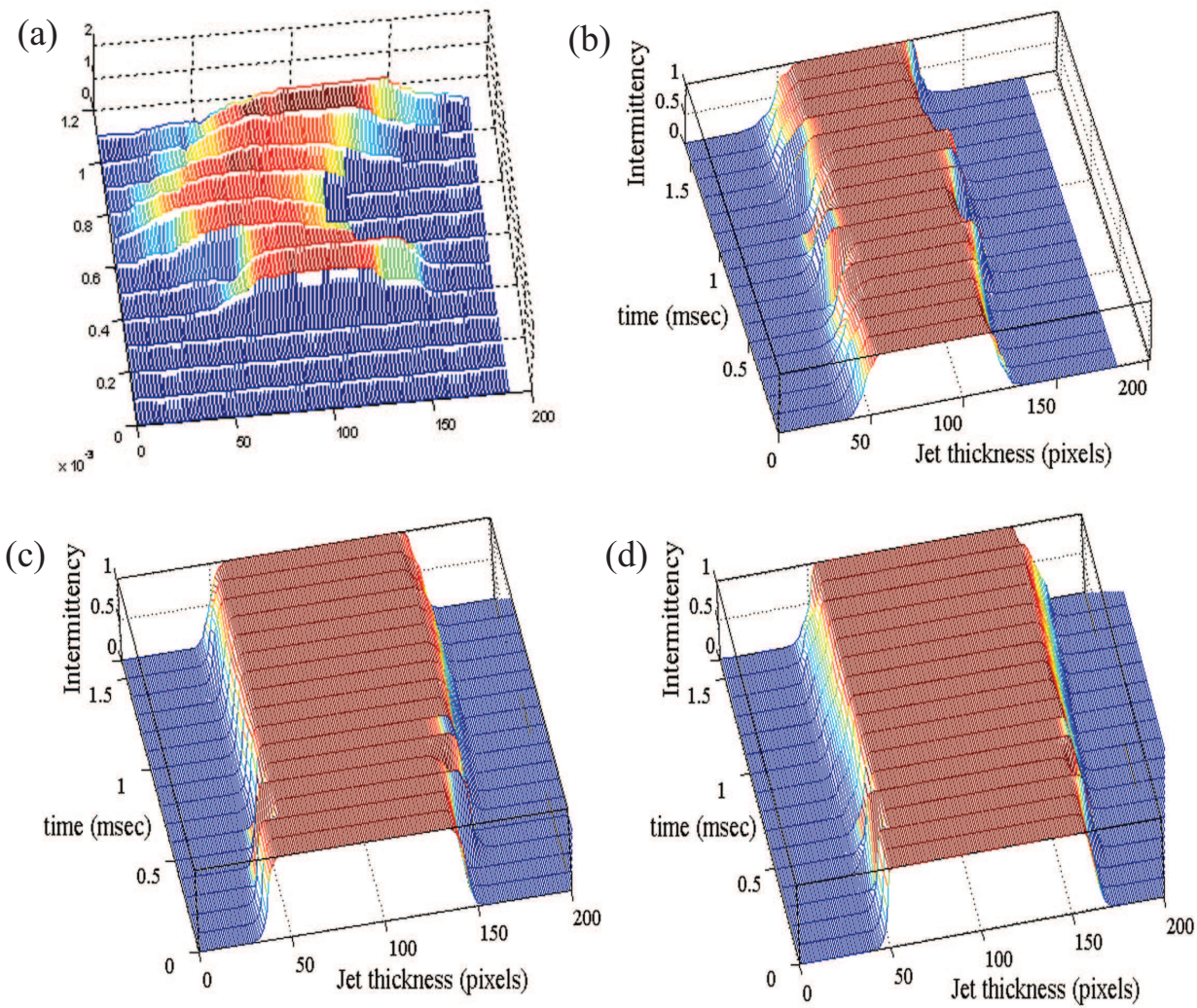


Figure 4.9: Intermittency of Hg jet at Viewport 2. The jet velocity is 15 m/s. a.)  $B=0\text{T}$ . b.)  $B=5\text{T}$ . c.)  $B=10\text{T}$ . d.)  $B=15\text{T}$  (continued).

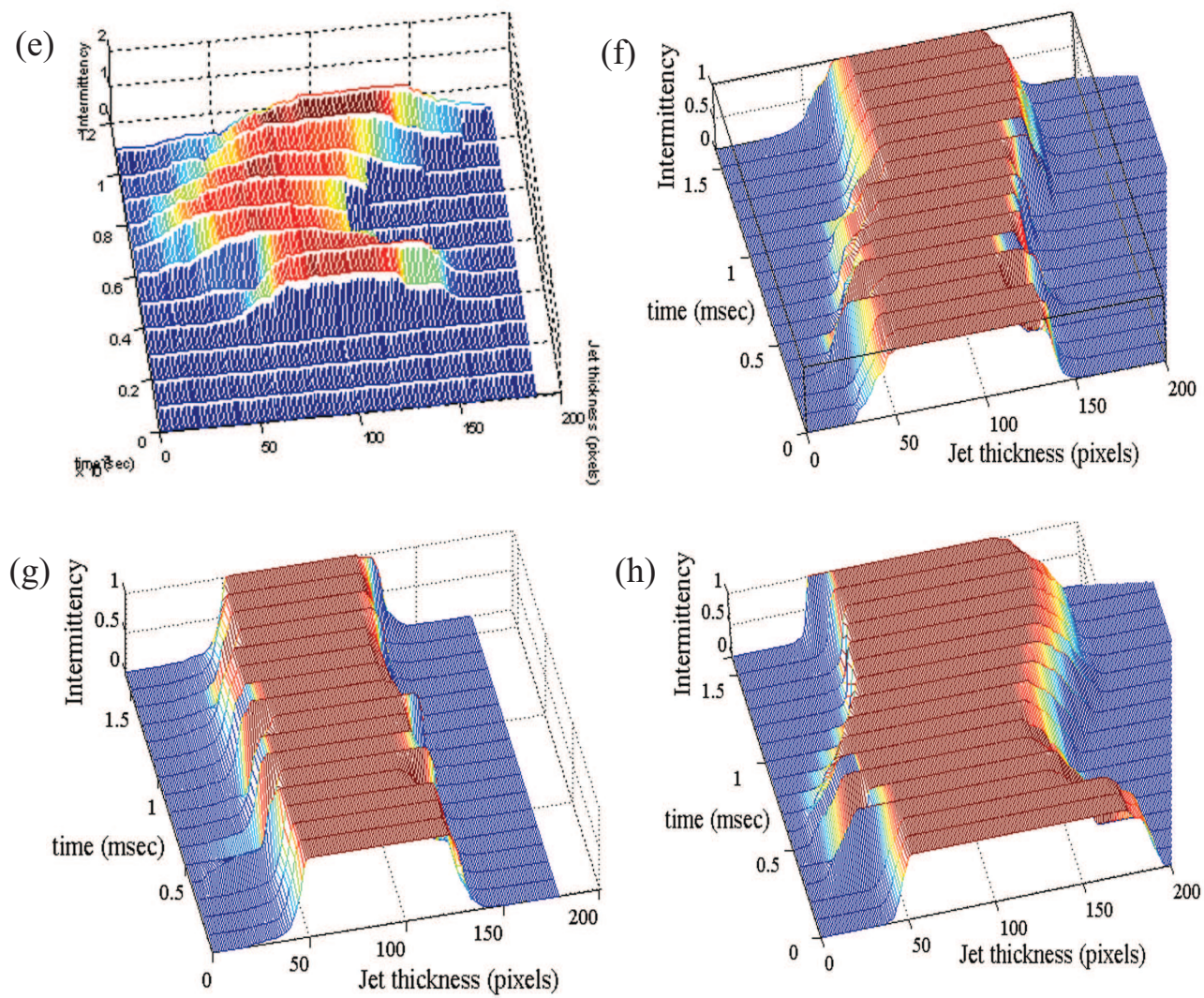


Figure 4.9: Intermittency of Hg jet at Viewport 2. The jet velocity is 20 m/s. e.)  $B=0T$ . f.)  $B=5T$ . g.)  $B=10T$ . h.)  $B=15T$ .



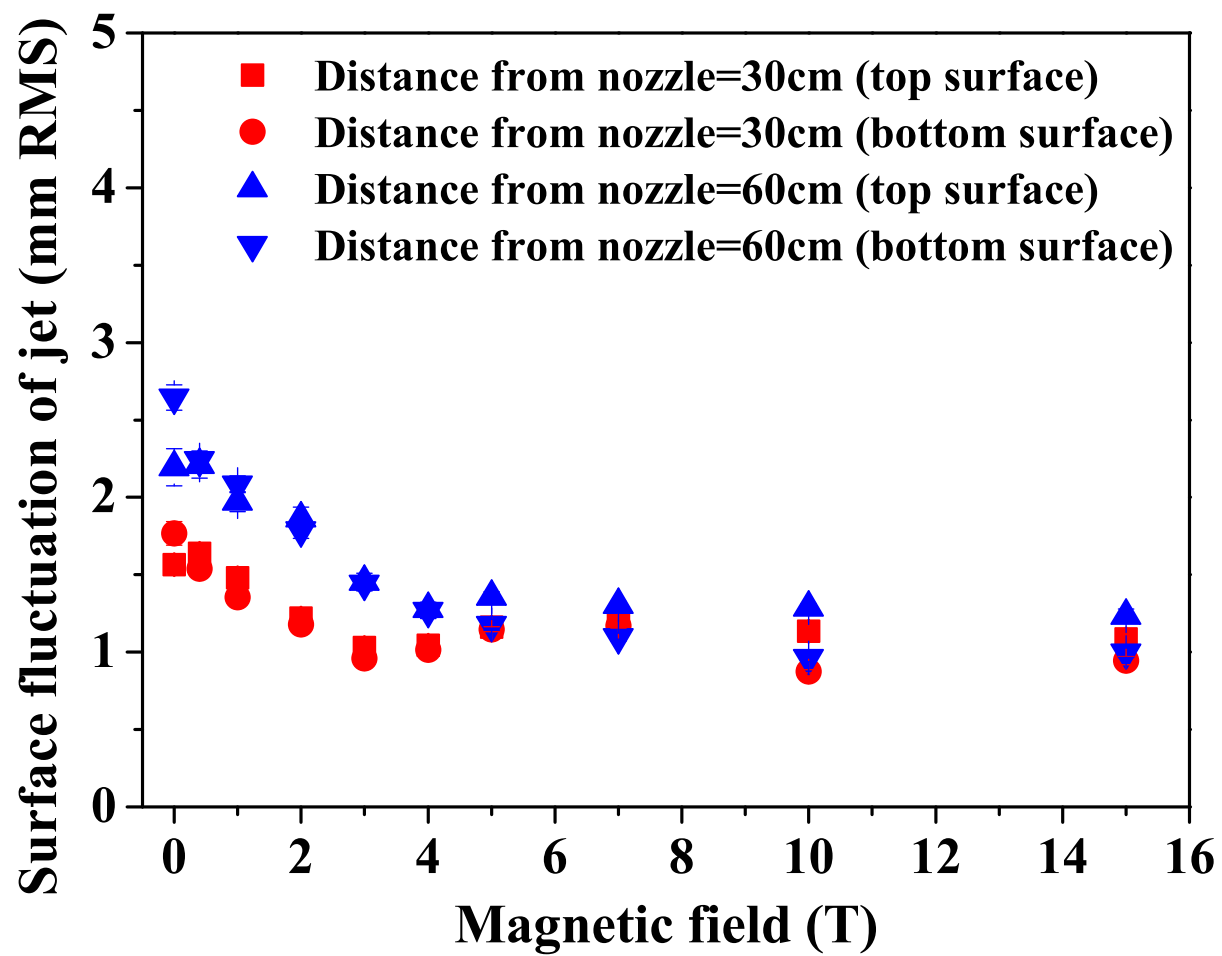


Figure 4.10: Surface fluctuations in a magnetic field.

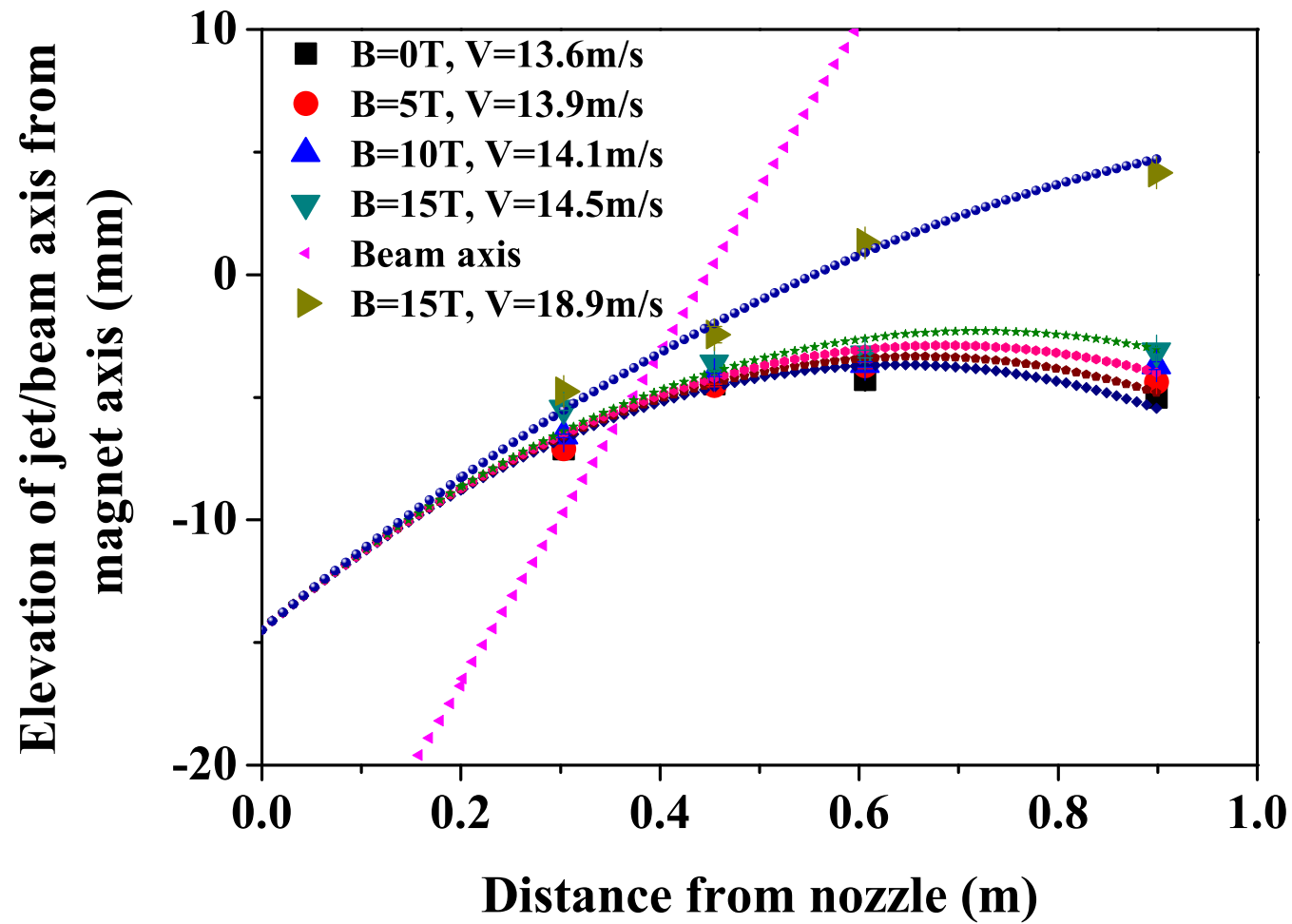


Figure 4.11: Trajectory of beam axis and Hg jet axis projectile with respect to magnetic axis in magnetic field.

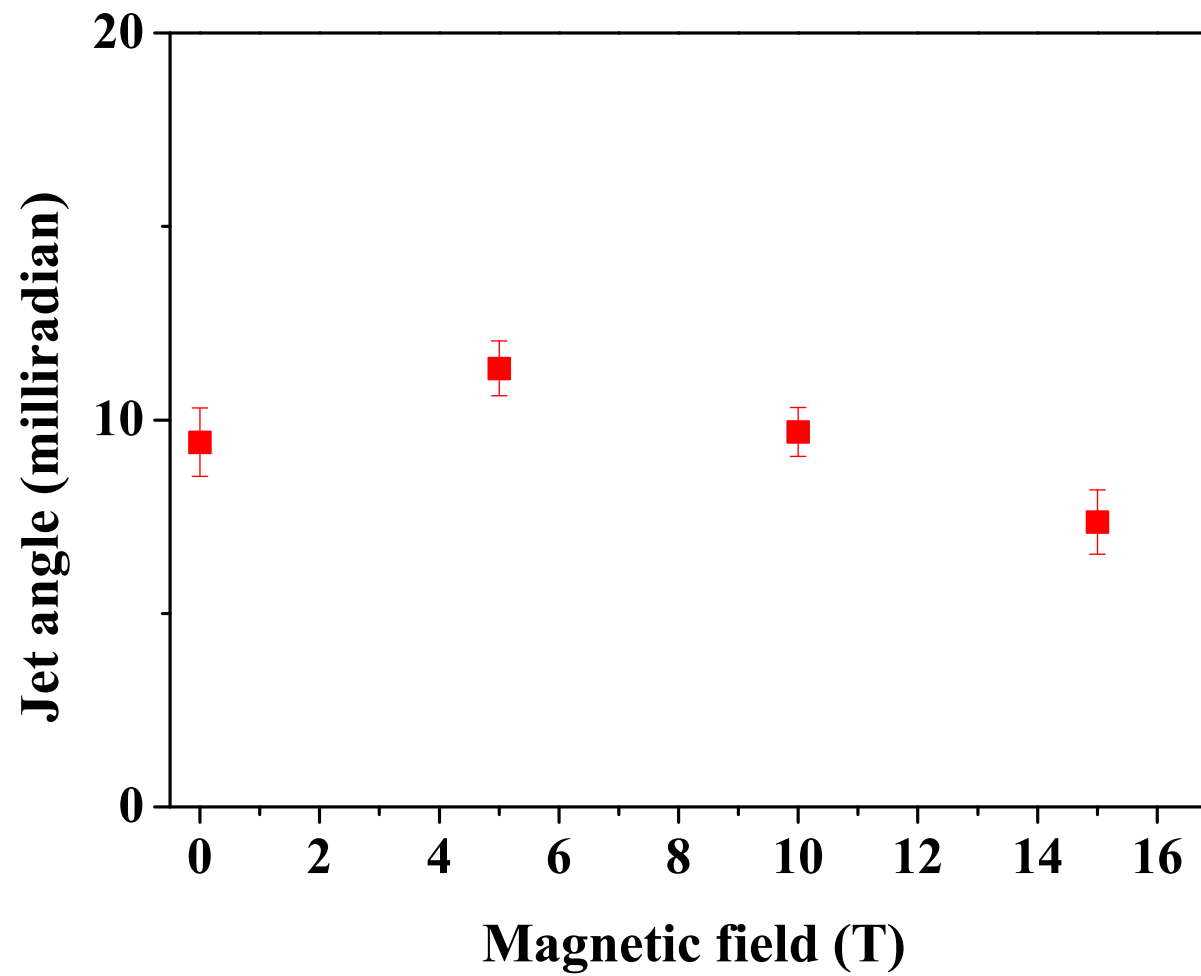


Figure 4.12: Hg jet angle at the center of magnetic axis (Viewport 2) as a function of magnetic field.

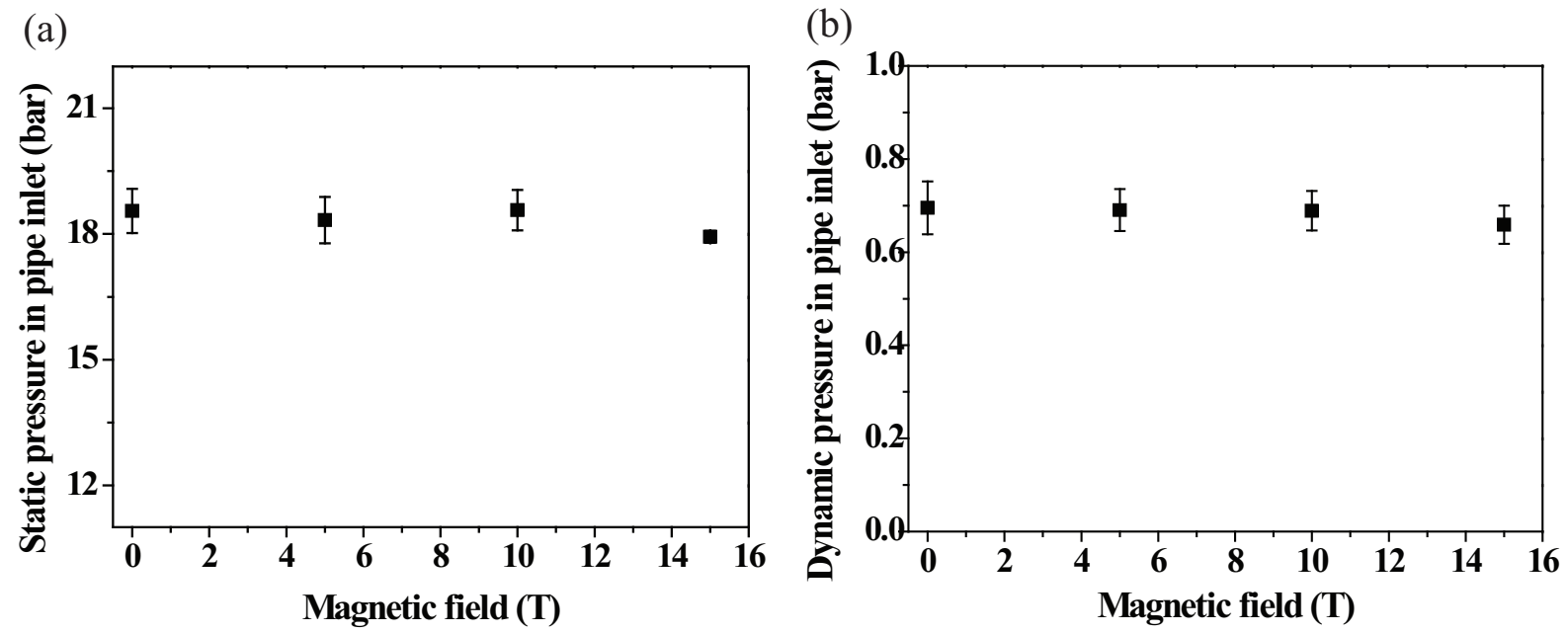


Figure 4.13: Pipe inlet pressure for the driving jet. a.) Static pressure. b.) Dynamic pressure.

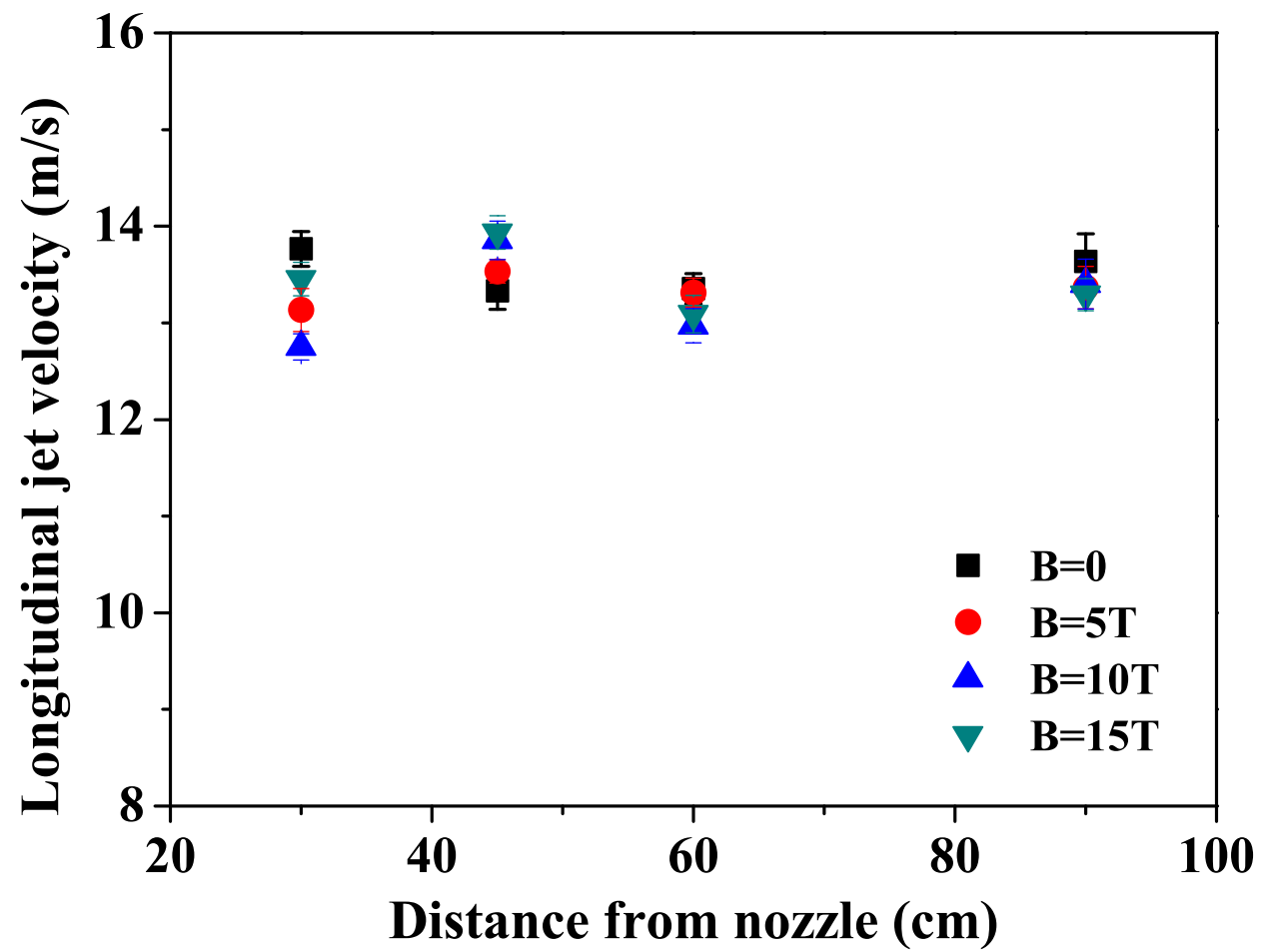


Figure 4.14: Longitudinal Hg jet flow velocity in magnetic field.

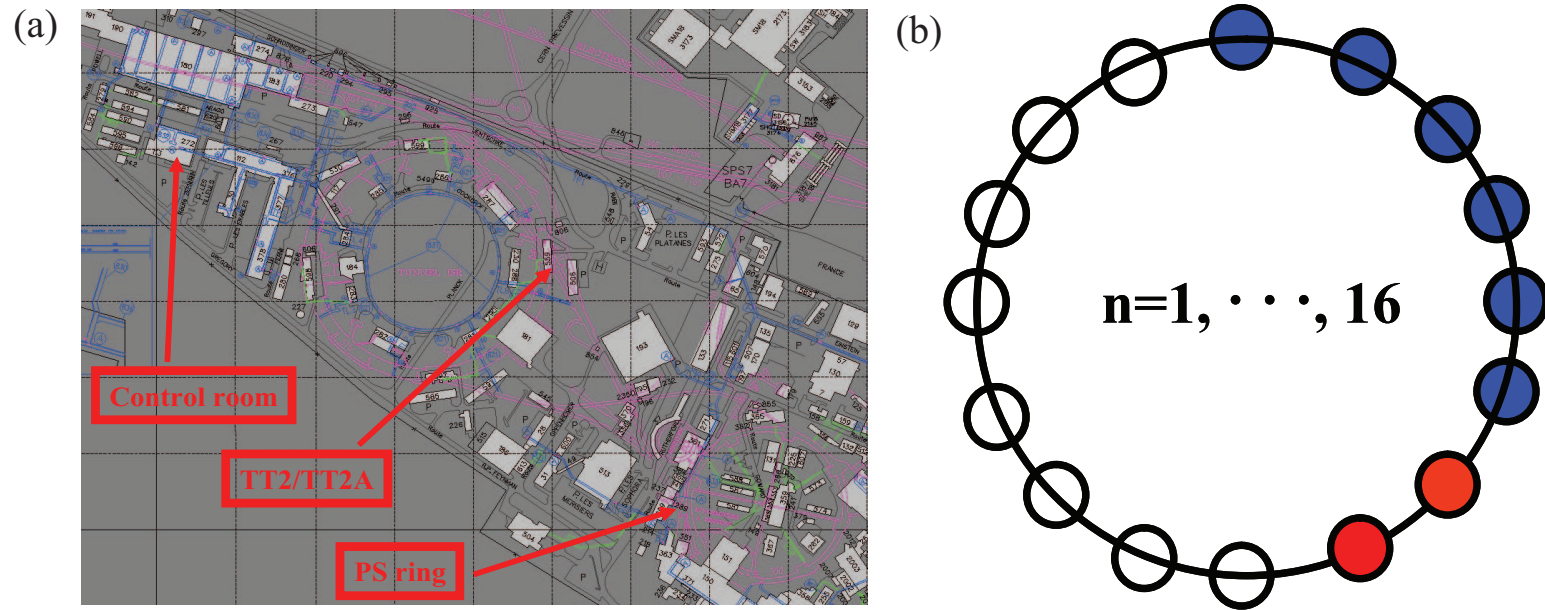


Figure 4.15: Infrastructures for experiment at CERN. a.) Proton synchrotron and TT2 tunnel for experiment. b.) 16 harmonics of beam extraction in proton synchrotron.

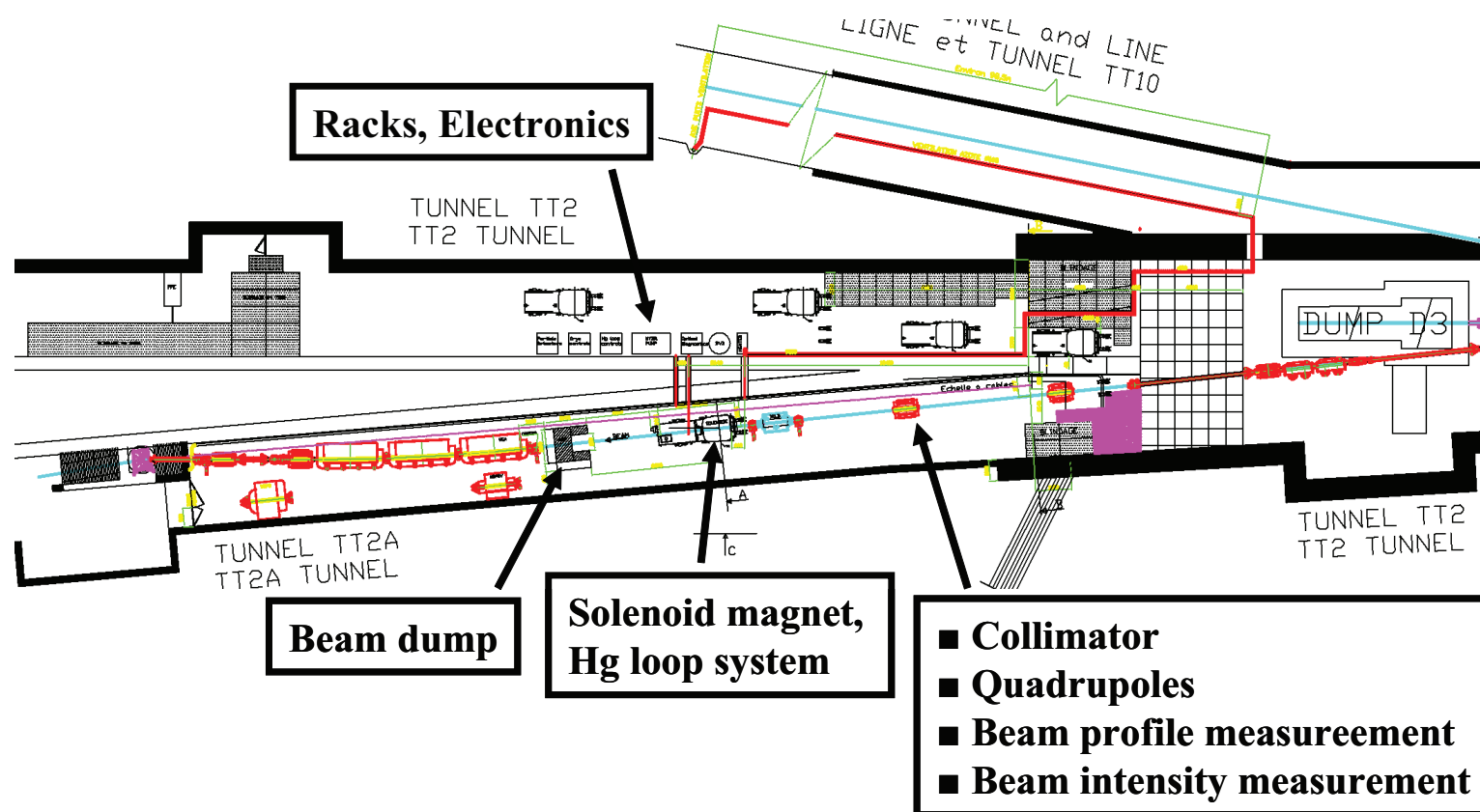


Figure 4.16: Installation of integrated experimental components in tunnel TT2/TT2A for high power target experiment.

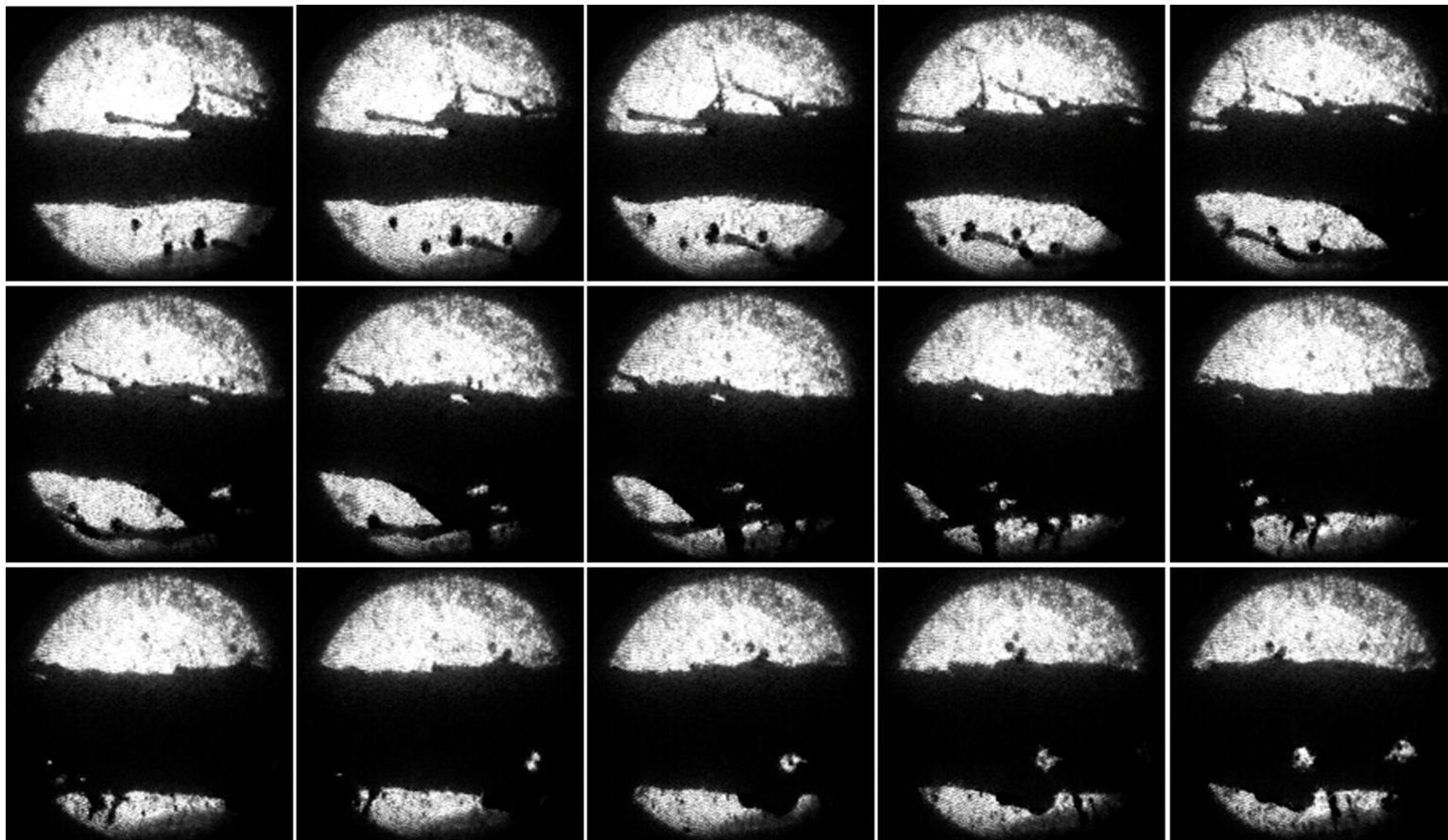


Figure 4.17: Photographs of the Hg jet interaction with 16 TP, 14 GeV/c proton beam at 5 T. Captured at Viewport 3 at  $500 \mu\text{s}$  frame rate (continued).



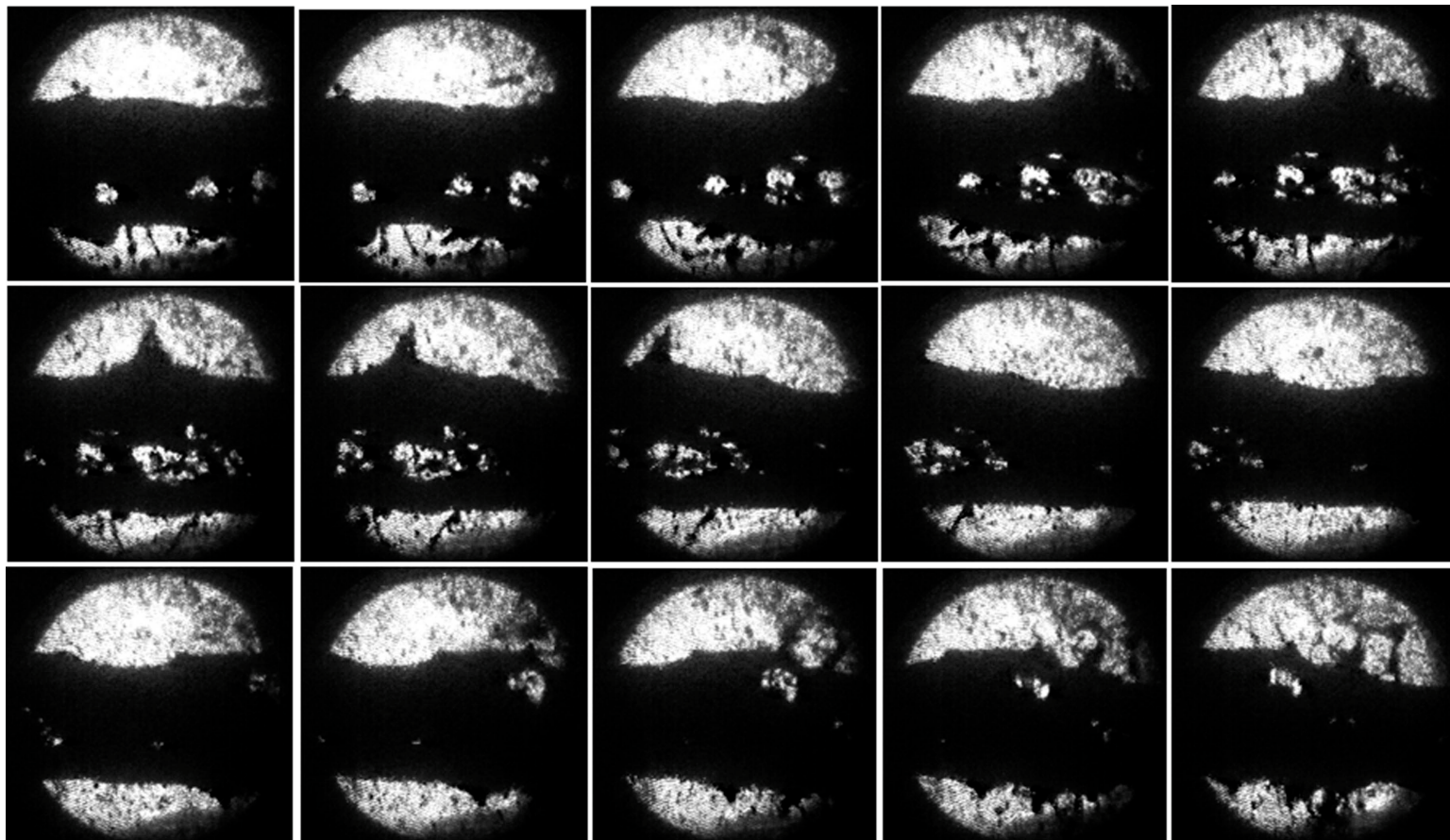


Figure 4.17: Photographs of the Hg jet interaction with 16 TP, 14 GeV/c proton beam at 5 T. Captured at Viewport 3 at  $500 \mu\text{s}$  frame rate (continued).

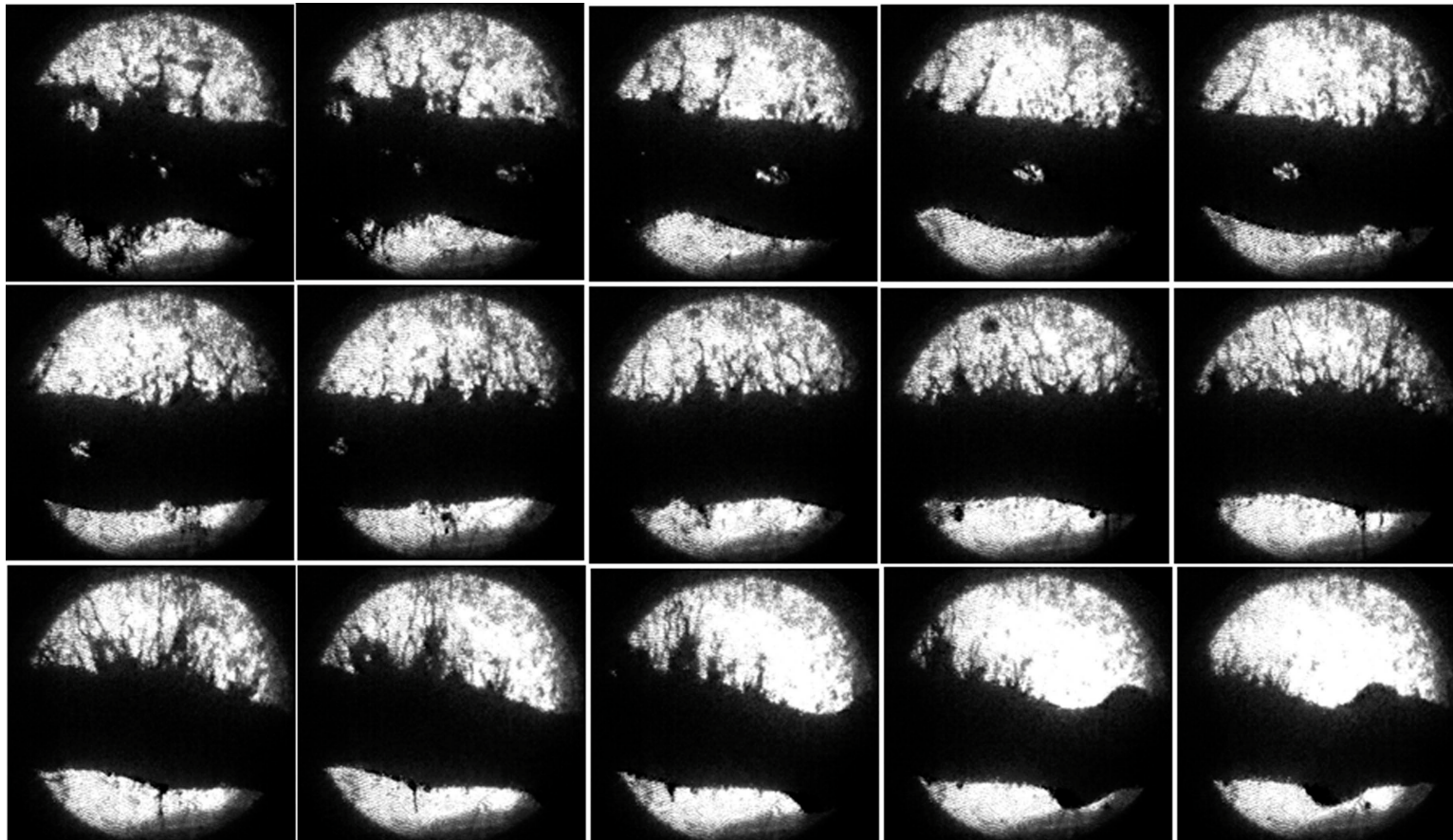


Figure 4.17: Photographs of the Hg jet interaction with 16 TP, 14 GeV/c proton beam at 5 T. Captured at Viewport 3 at  $500 \mu\text{s}$  frame rate.

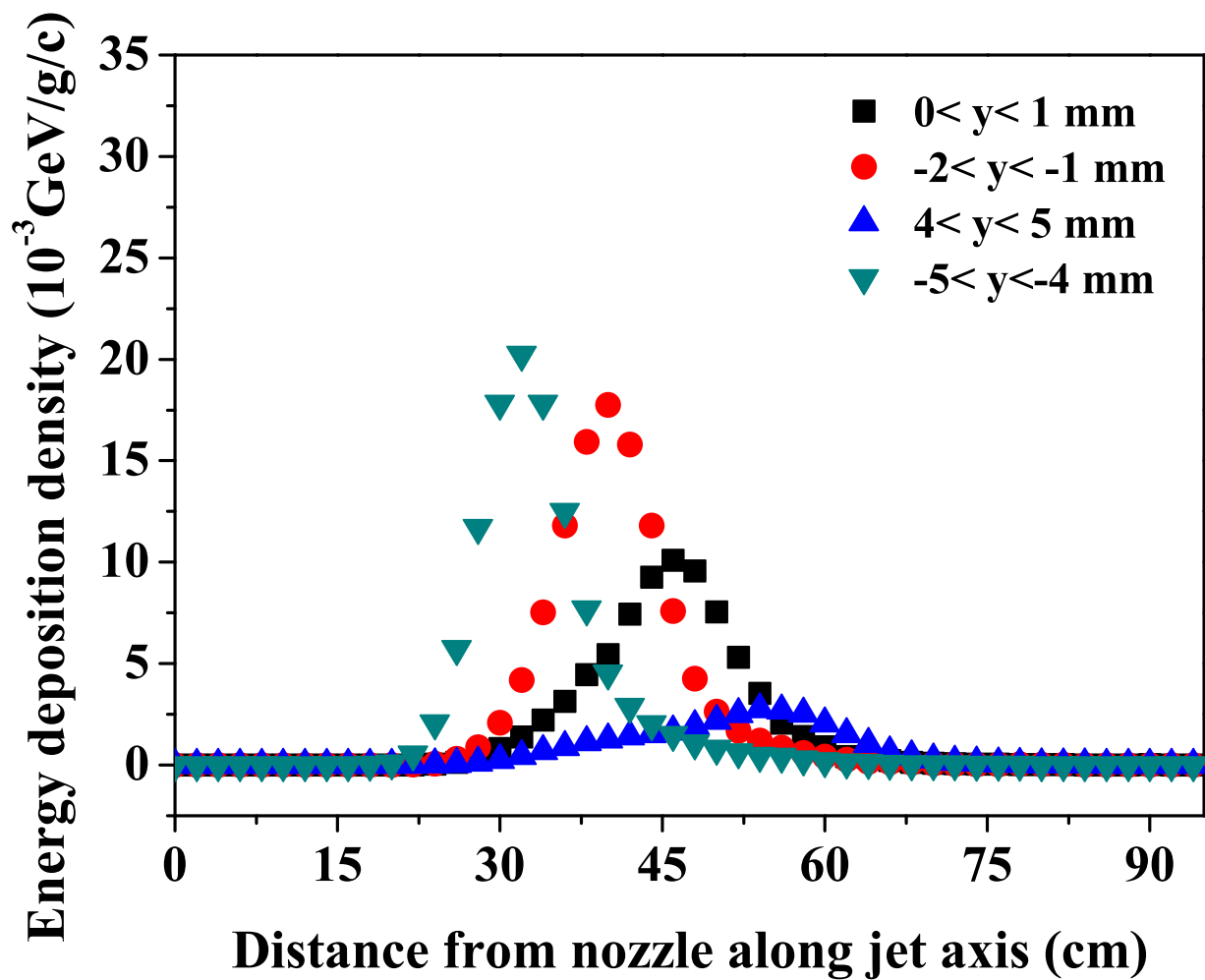


Figure 4.18: Calculated energy deposition density to cross sectional area of Hg jet with 14 GeV/c proton beam in 0 T (Striganov, 2008).

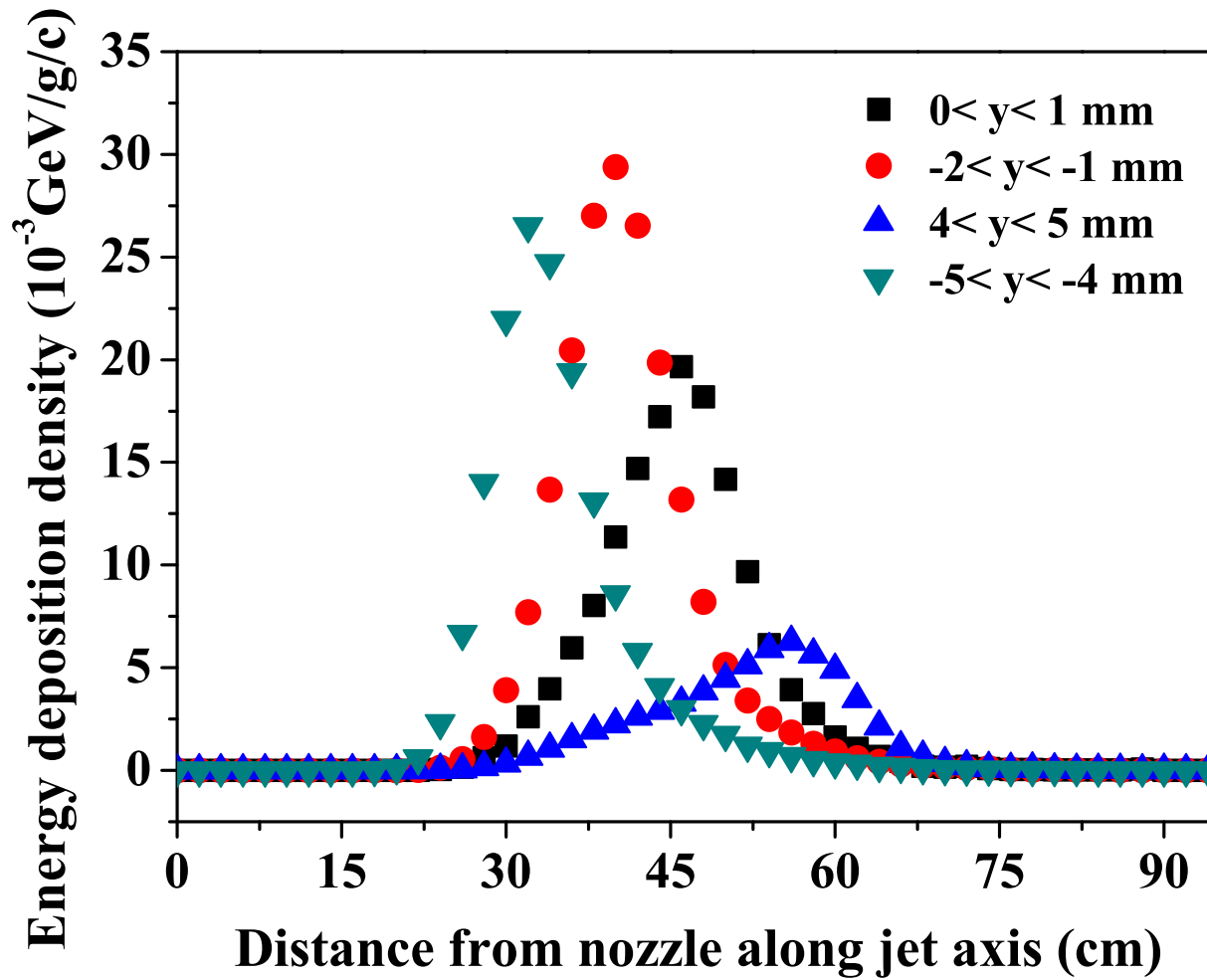


Figure 4.19: Calculated energy deposition density to cross sectional area of Hg jet with 24 GeV/c proton beam in 0 T (Striganov, 2008).

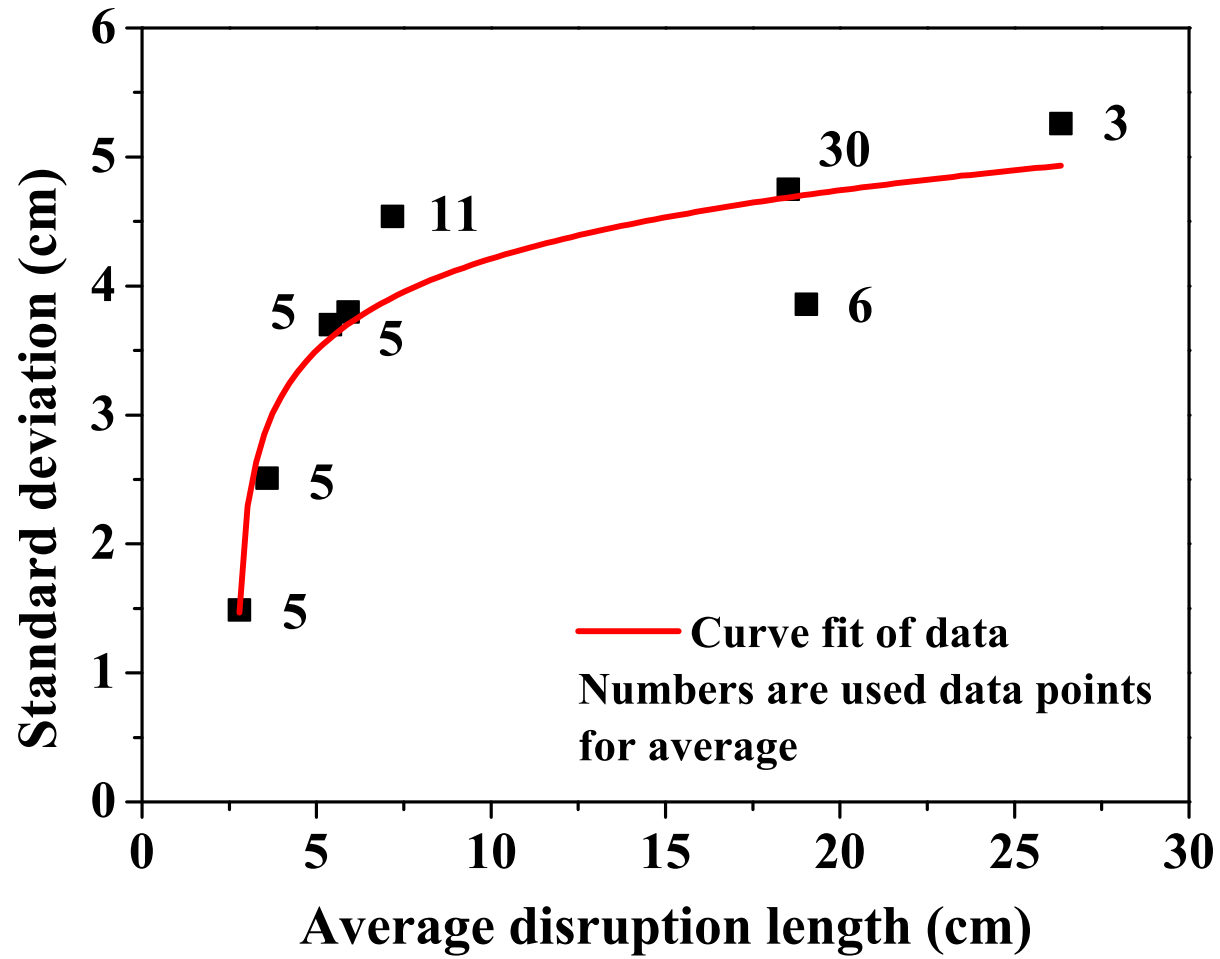


Figure 4.20: Standard deviation of disruption length as a function of disruption length and the function of fitted curve. The fitted curve is  $\sigma_{disruption} = 2.99 + 0.6144 \ln(L_{disruption} - 2.7062)$ .

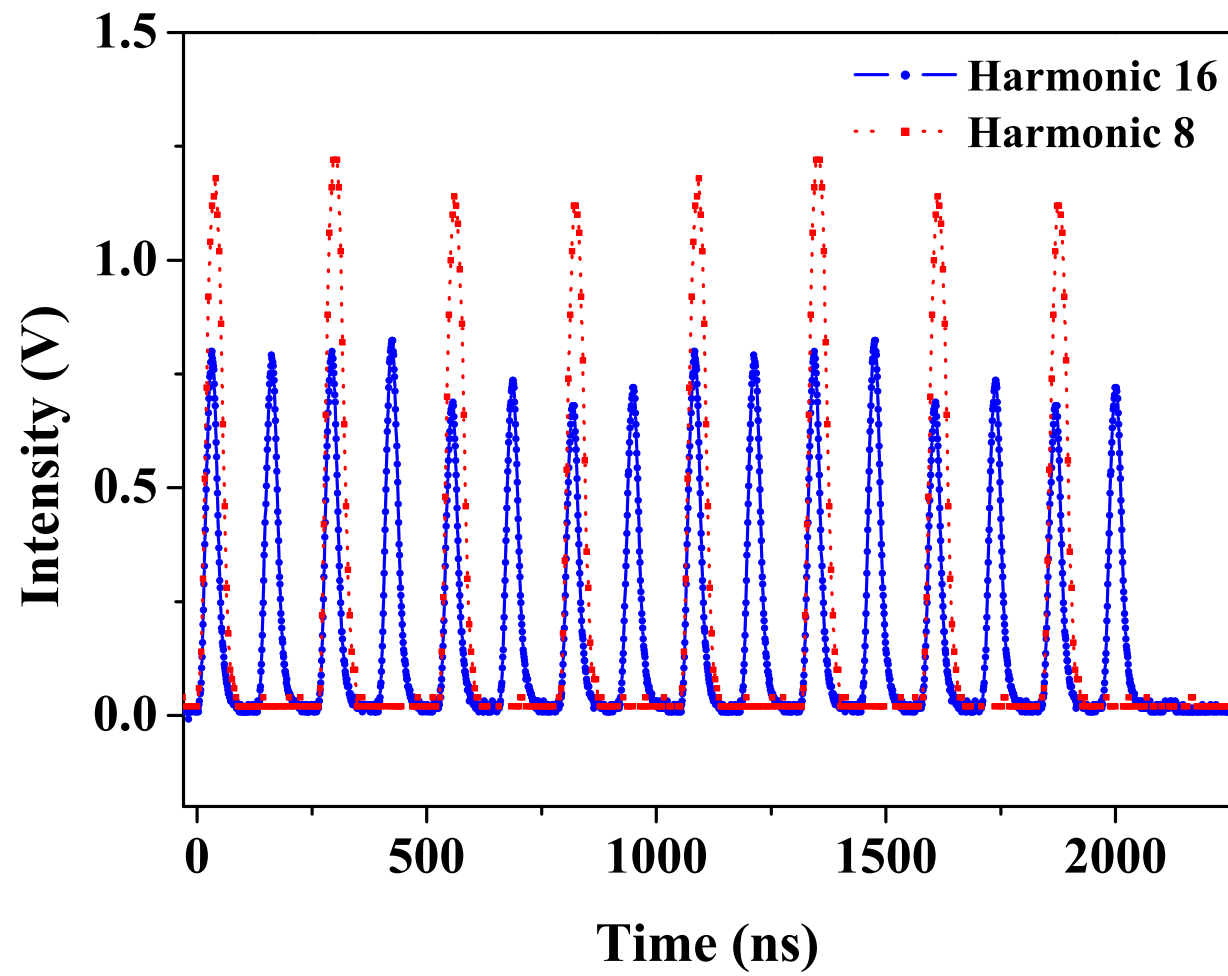


Figure 4.21: Proton beam pulse structure of harmonic 8 and harmonic 16 in 14 GeV and 6 TP.

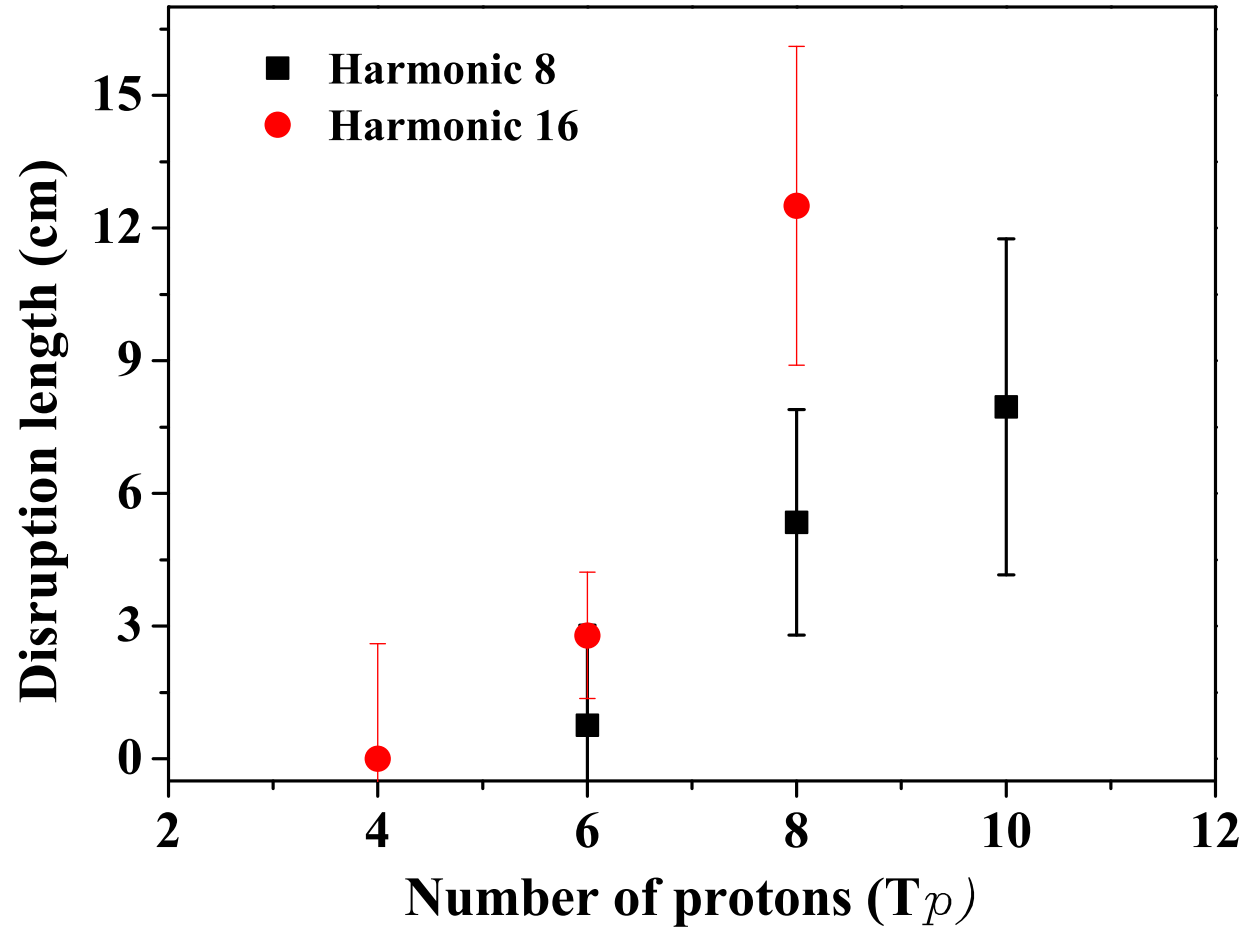


Figure 4.22: Disruption length of Hg jet depending on the beam pulse structure as a function of 14 GeV beam intensity in 5 T.  $T_p = 10^{12}$  protons

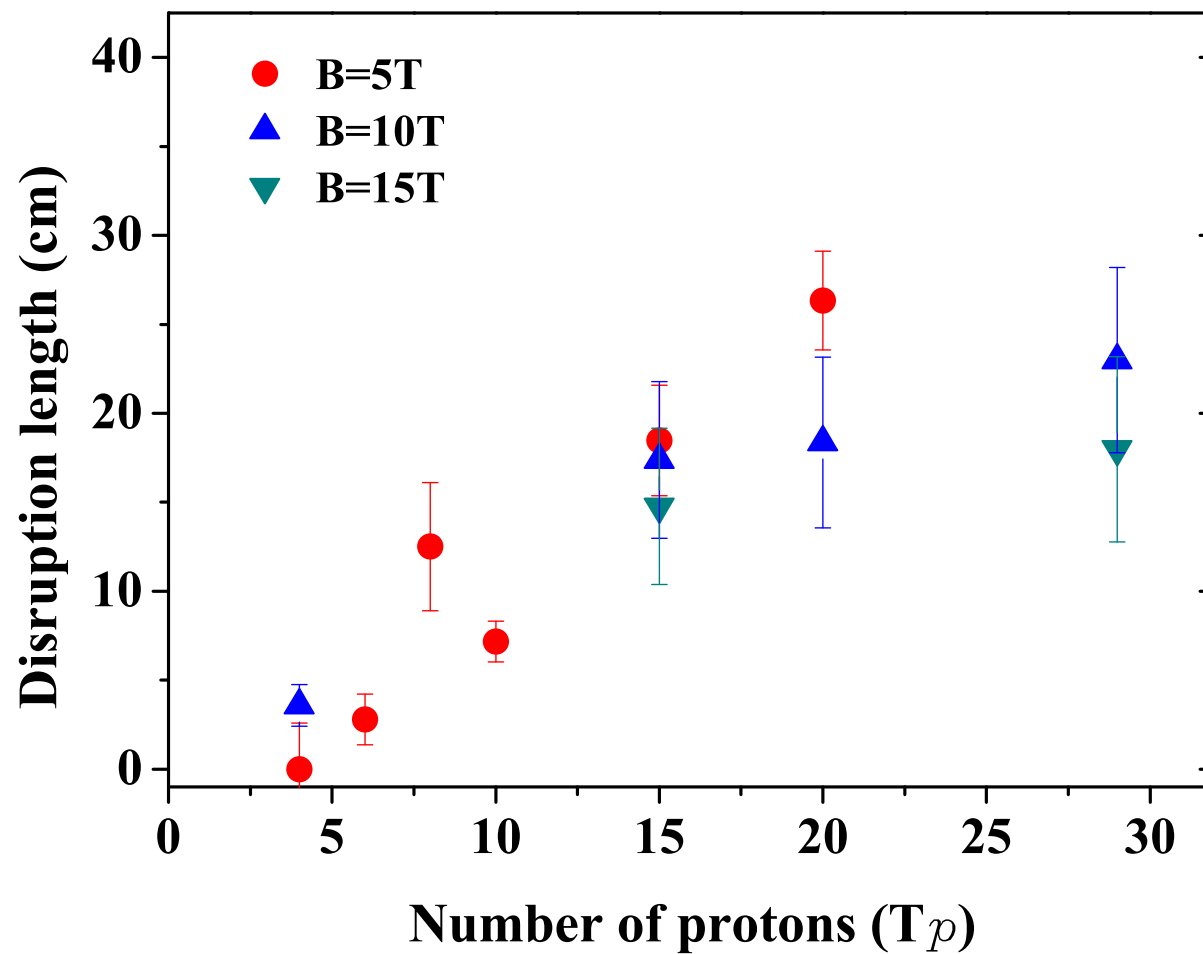


Figure 4.23: Disruption length of Hg jet as a function of 14 GeV beam intensity and magnetic field. Harmonic 16 with 16 bunches is used.



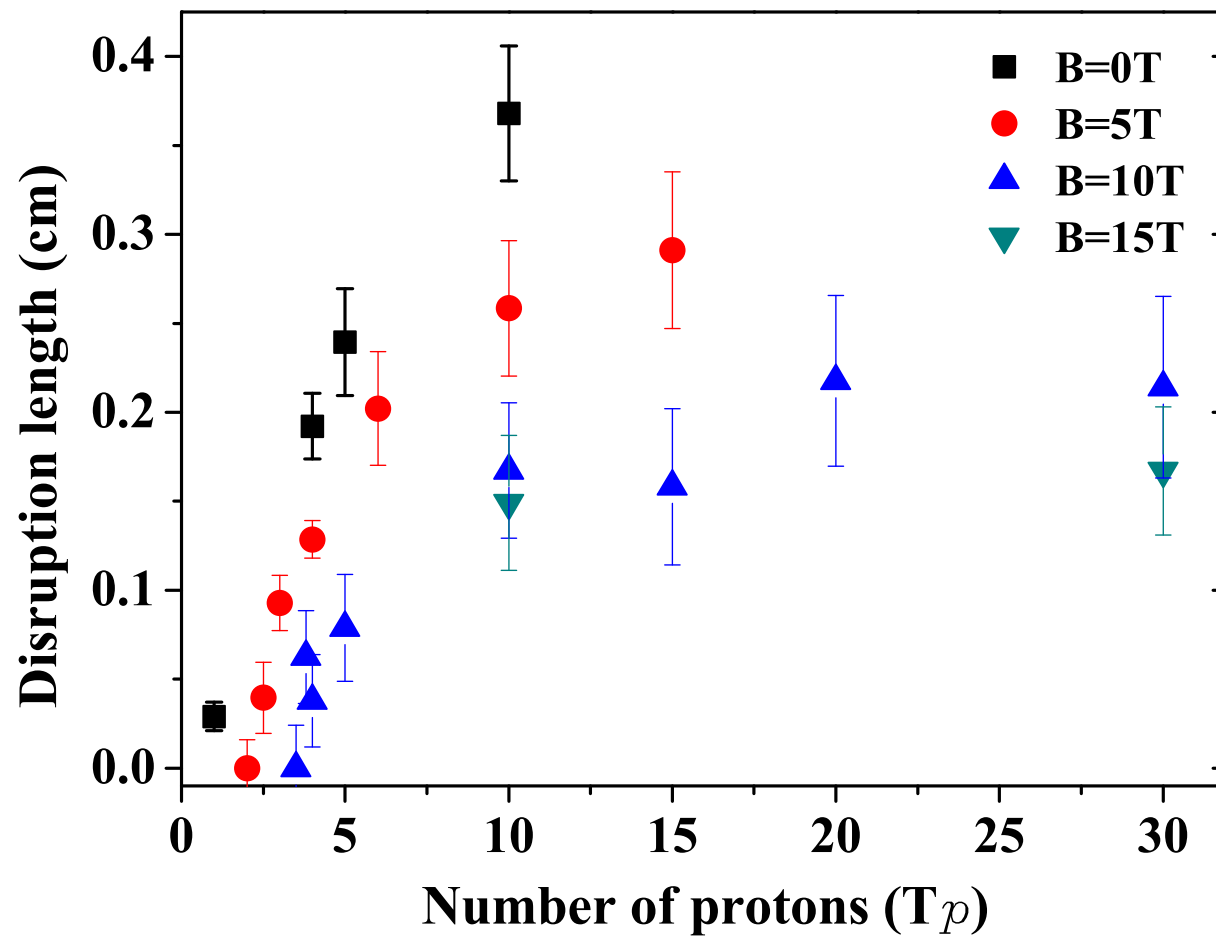


Figure 4.24: Disruption length of Hg jet as a function of 24 GeV beam intensity and magnetic field.

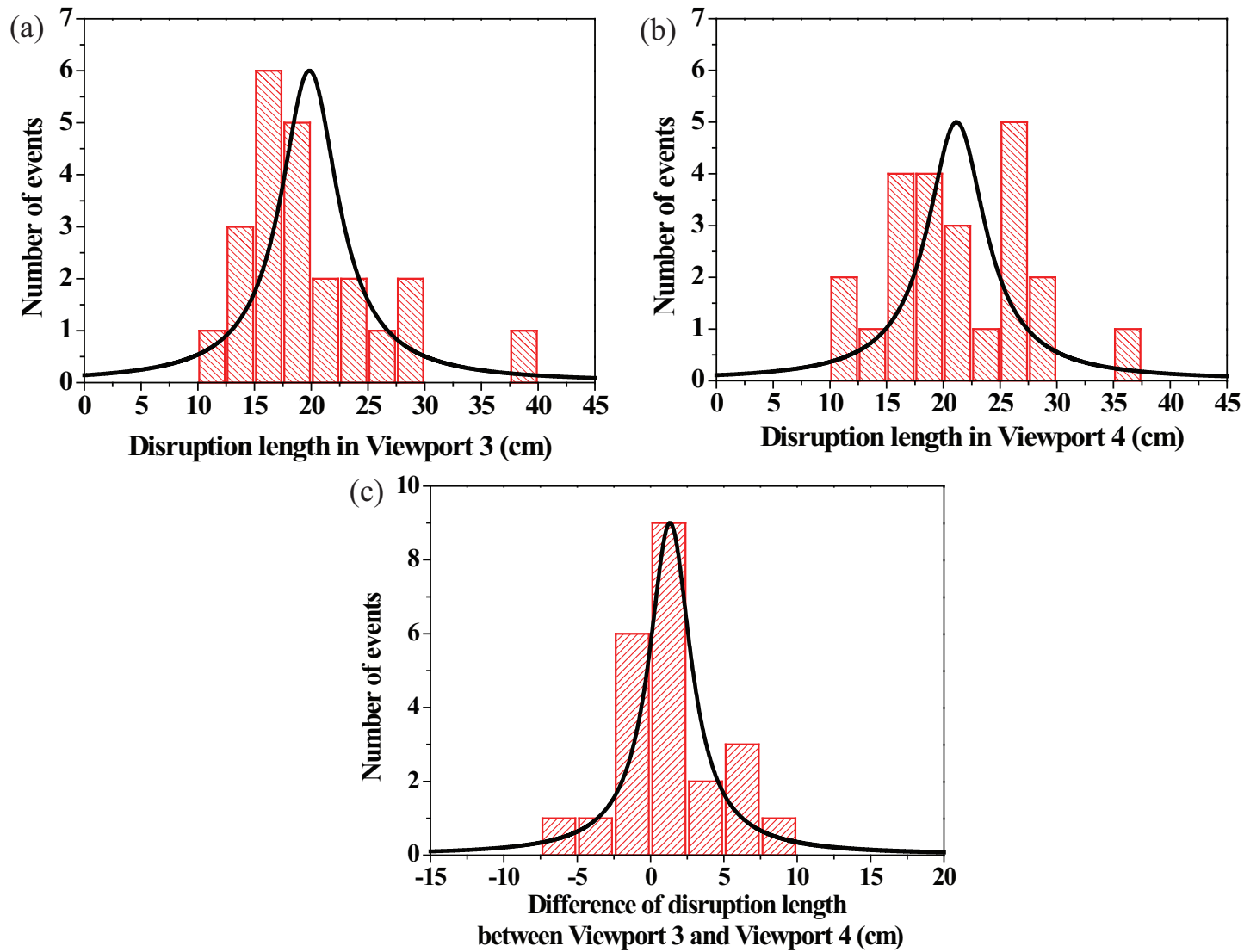


Figure 4.25: Validation of disruption measurement for the evaluation of evolution of disruption length from Viewport 3. a) Disruption length at Viewport 3. b.) Disruption length at Viewport 4. c.) Difference of the disruption length at Viewport 3 and Viewport 4.

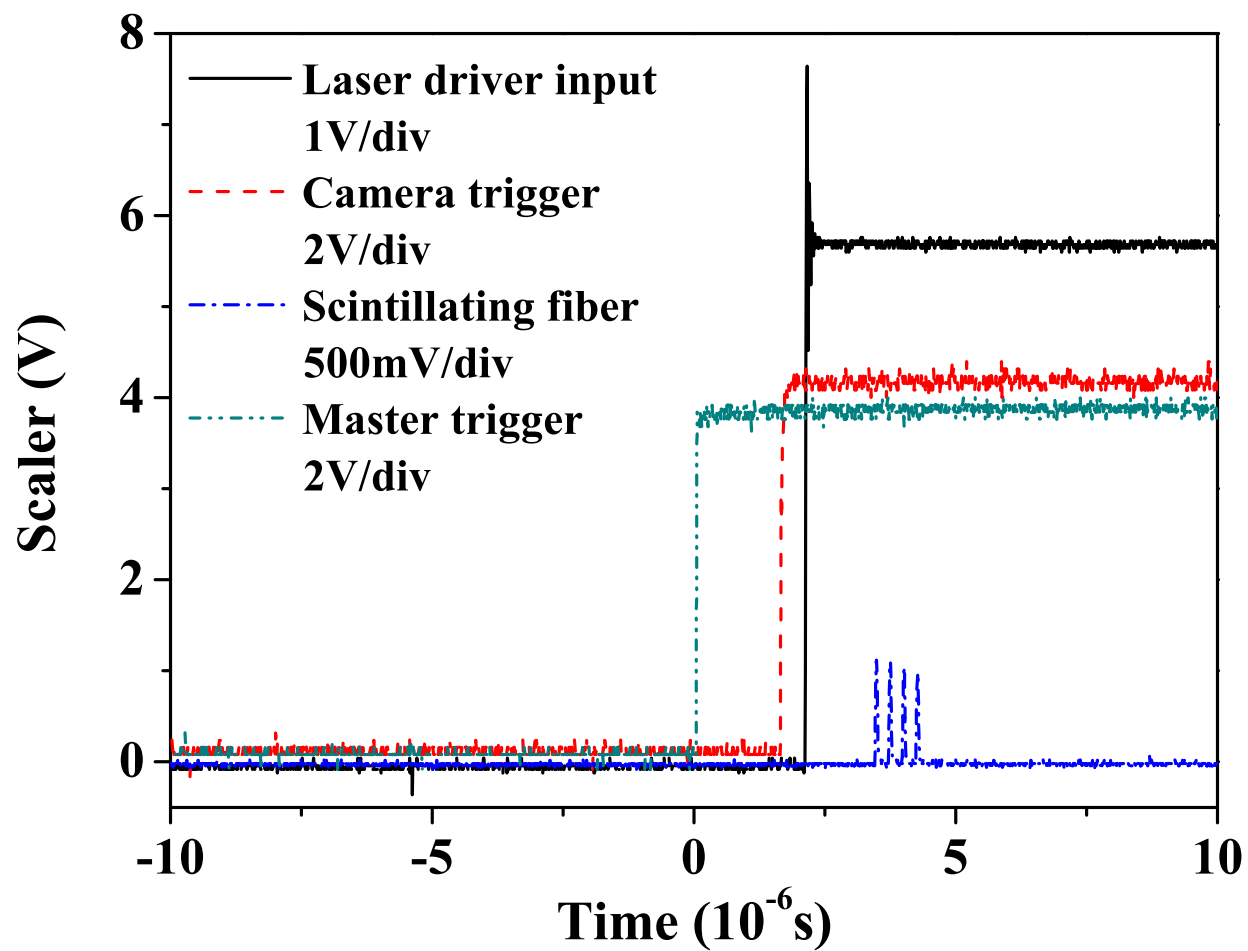


Figure 4.26: The triggering time for high speed camera upon beam arrival.

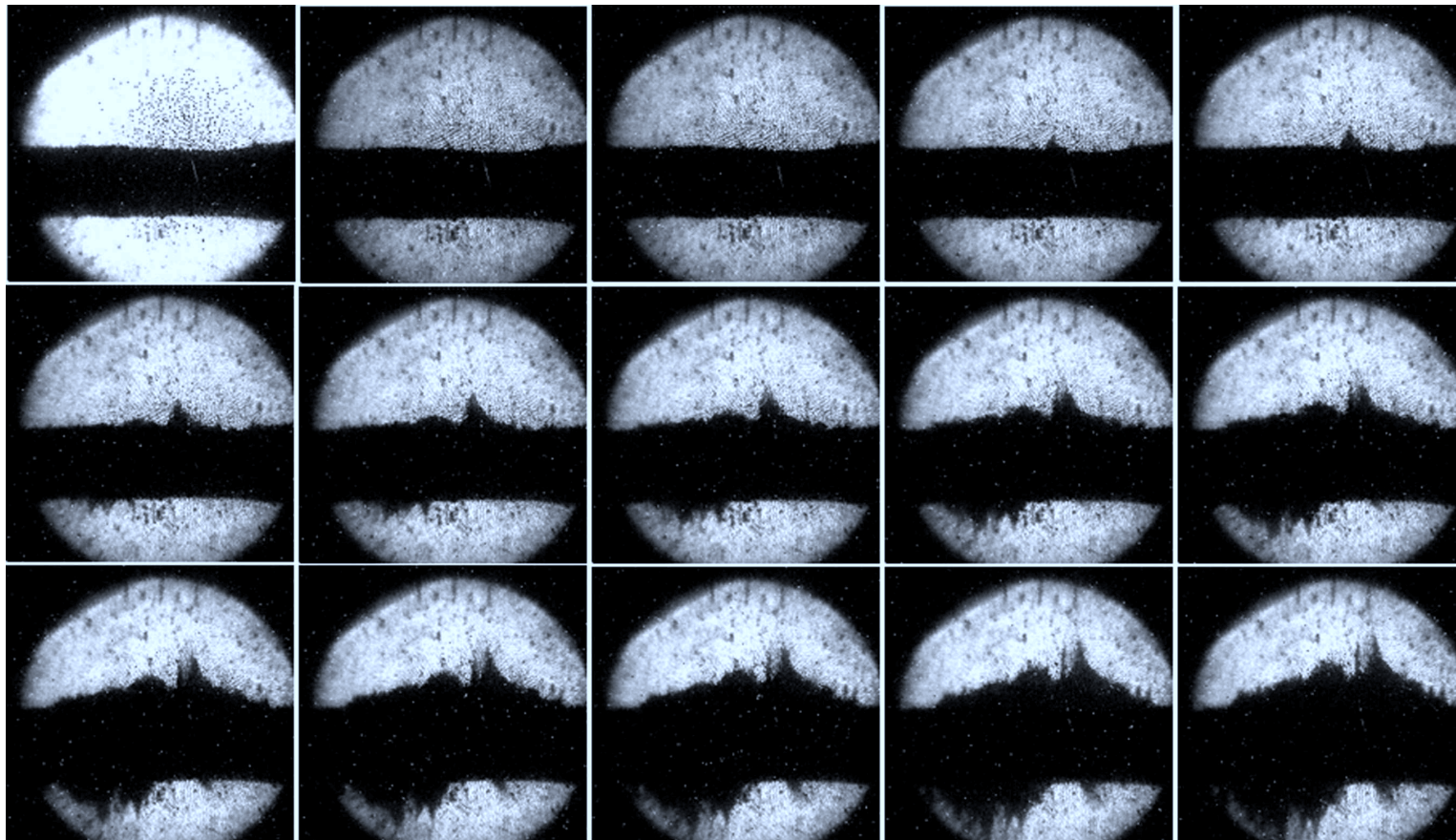


Figure 4.27: Photographs of filament evolution on the Hg jet surface as a function of time at  $25 \mu\text{s}$  frame rate. The beam is 10 TP, 24 GeV. The magnetic field is 10 T.

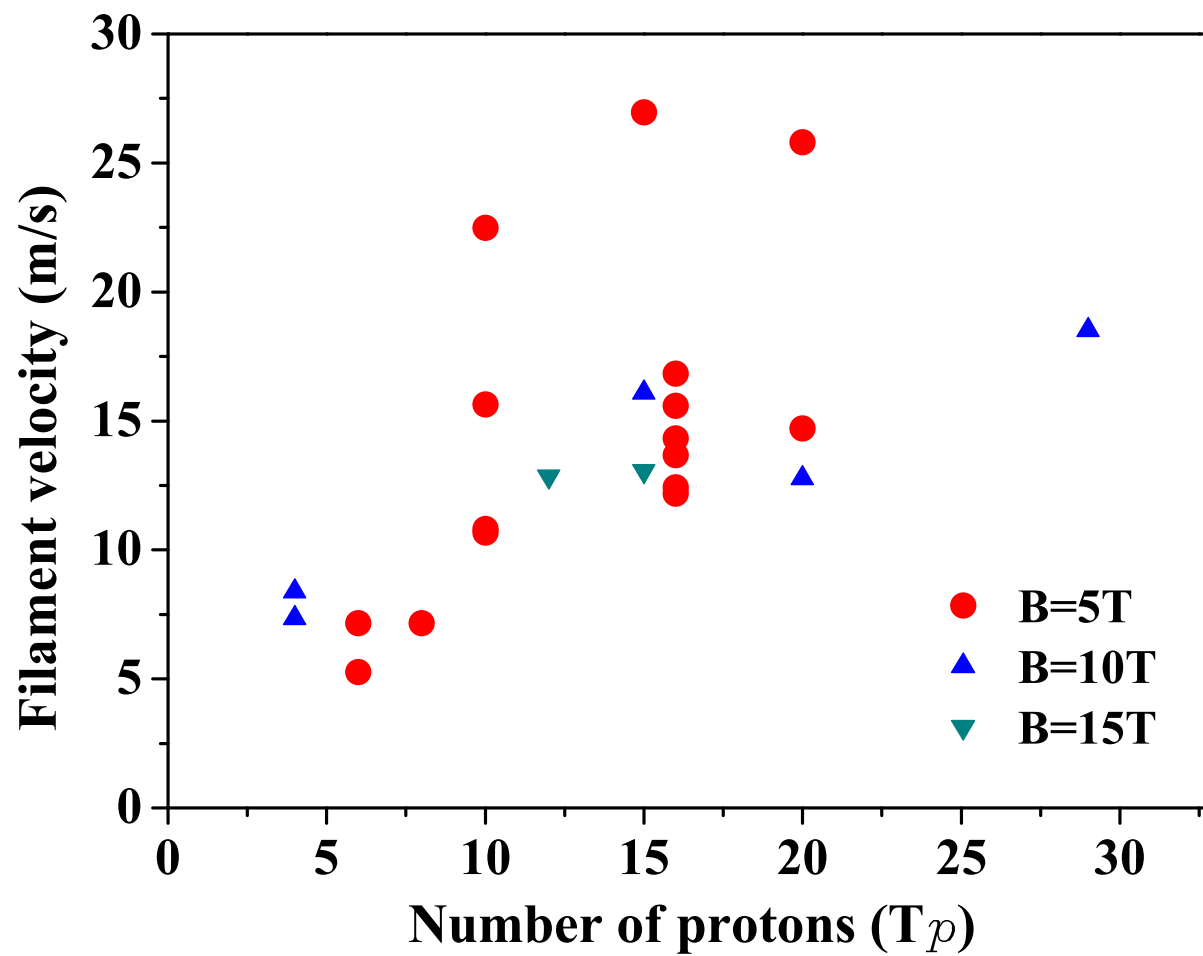


Figure 4.28: Filament velocity as a function of 14 GeV beam intensity and magnetic field.

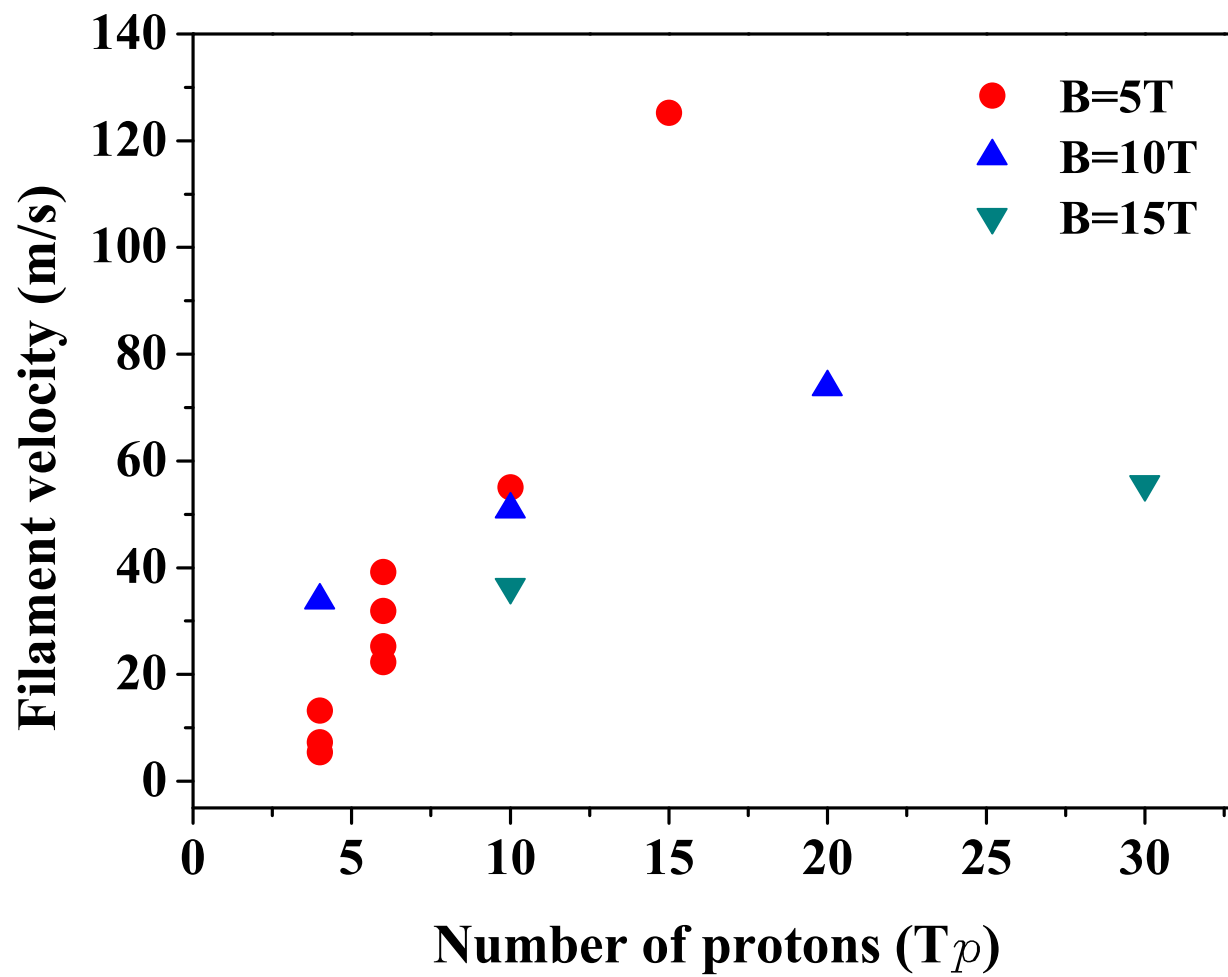


Figure 4.29: Filament velocity as a function of 24 GeV beam intensity and magnetic field.

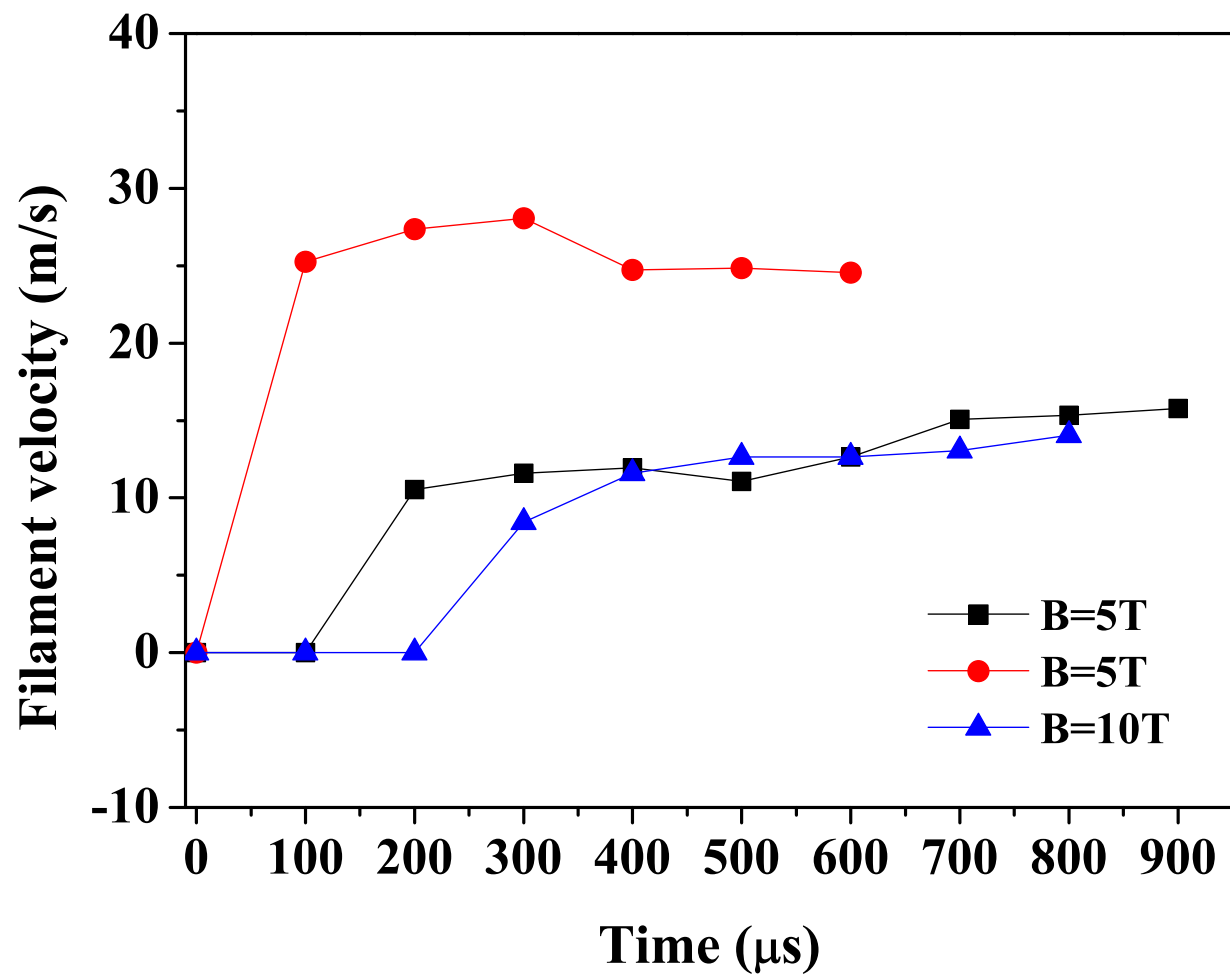


Figure 4.30: Time response of filament velocity as a function of magnetic field with 14 GeV, 20 TP beam.

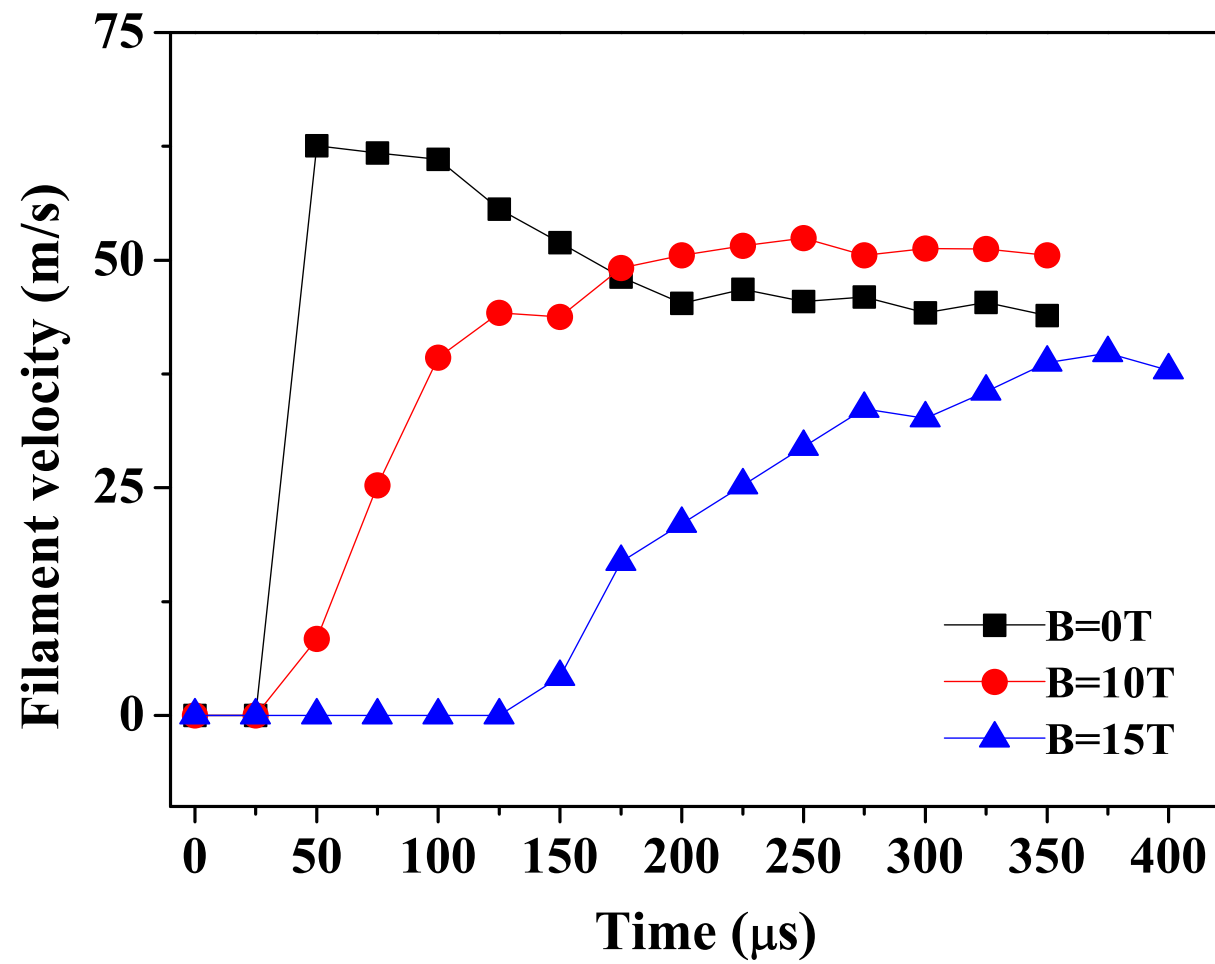


Figure 4.31: Time response of filament velocity as a function of magnetic field with 24 GeV, 10 TP beam.



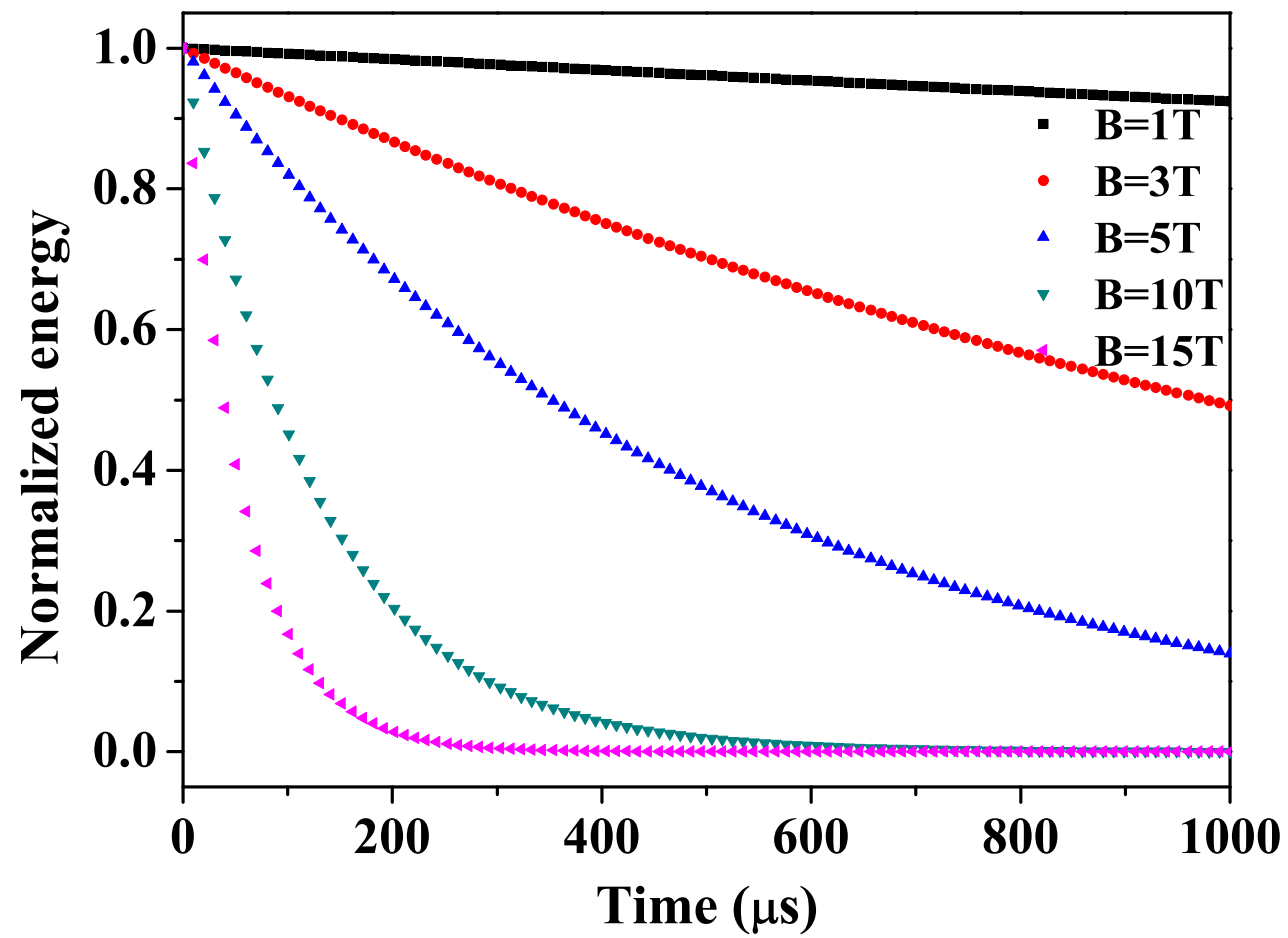


Figure 4.32: Energy decay in magnetic fields.

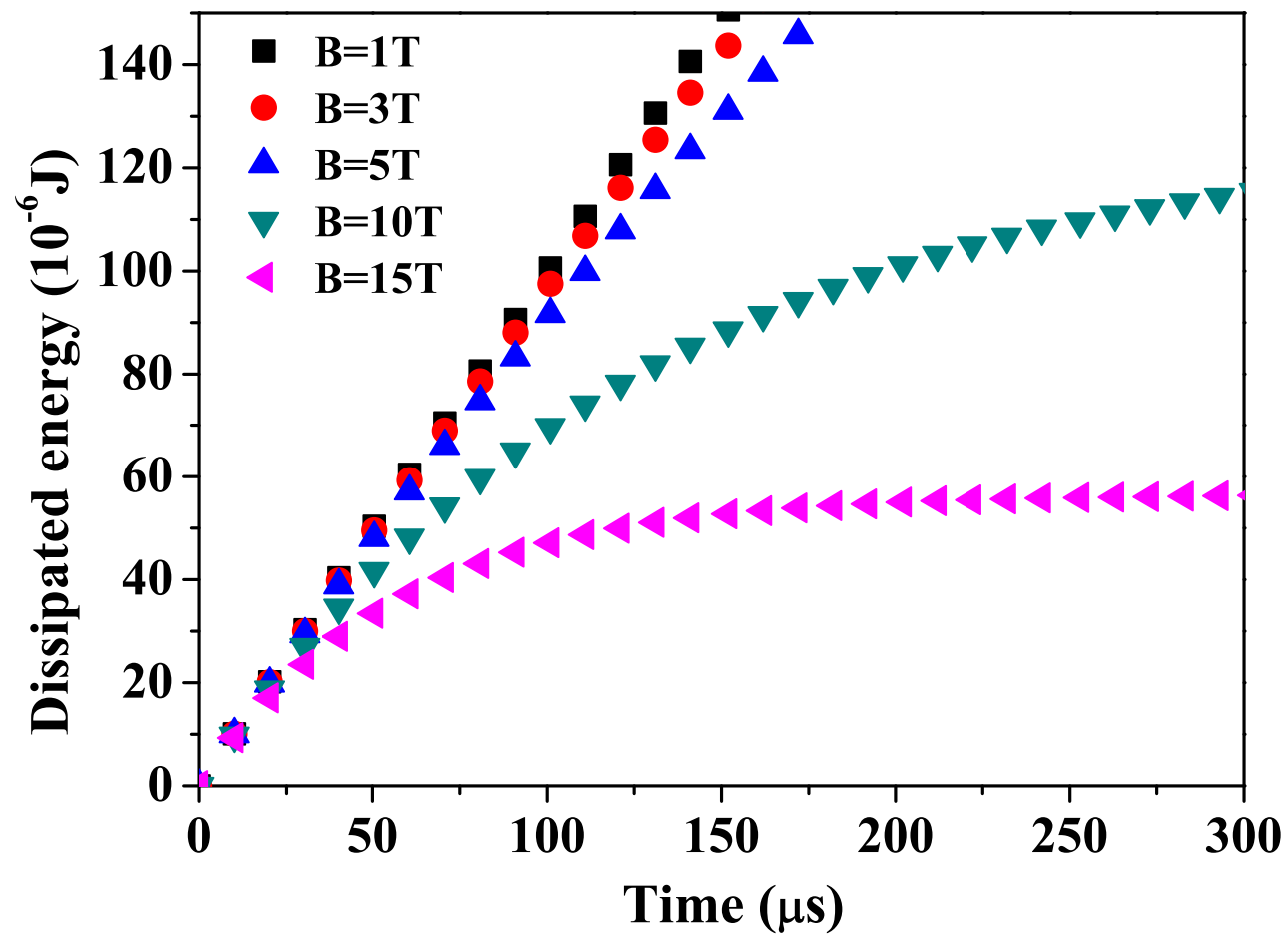


Figure 4.33: Integrated total energy with respect to time in magnetic fields.

# Chapter 5

## Conclusions

The experiment is a proof-of-principle test for a target system capable of accepting a high-intensity 4 MW proton beam. The system allows for the production of copious pions which subsequently decay into muons. These muons are magnetically captured, accelerated and inserted into storage rings. An experiment at the CERN Proton Synchrotron that combines a free mercury jet target with a 15 T solenoid magnet and 14 GeV 24 GeV proton beam was performed. It validates the target concept for producing an intense secondary source of muons. When combined with a beam bunch of  $30 \times 10^{12}$  protons on the mercury target, this will generate a peak energy deposition of 100 J/g. For this experiment, a pulsed solenoid was designed, which is capable of delivering a peak field of 15 T. The Hg jet loop system generates a mercury jet from 1 cm diameter nozzle with velocities up to 20 m/s. An optical diagnostic system based on back-illuminated laser shadow photography is employed to investigate the mercury jet flow. Synchronized short laser light pulses are used to illuminate the target and freeze the motion of the jet. A total of four optical imaging heads for each Viewport are mounted on the exterior of the

primary containment vessel. Three high speed cameras are used to simultaneously collect images on three Viewports. Integrated all-in-one compact optical heads, consisting of ball lens, illumination fiber, objective lens, and imaging fiber bundle, are placed at the radius of curvature of a retro-reflector allowing for the illumination and imaging collection on one side of the mercury primary containment vessel. Due to the short time of frame rate, the time delay from the light source to the image arrival at the camera CCD is adjusted considering the delay from the electronics as well as the fiber-optics. The optimum timing delay is judged by the uniformity of consecutive collected image brightness as well as the triggering signal pulse on the oscilloscope for each component of device. The trigger timing is adjusted using the response of the scintillating fiber on the oscilloscope with respect to the beam triggering timing. The motions of mercury jet for 0.4 s at Viewport 1, 3, and 4 and for 1.6 ms at Viewport 2 are collected, respectively, which enables us to give both the overall jet condition at upstream (downstream) and the accurate motion of jet at midstream, where the magnetic induction field is maximum and the center of beam-jet interaction is positioned. Image processing provides some information on the mercury jet thickness at various magnetic induction field strengths and velocities, i.e., the optical diagnostic observation shows the effects of the magnetic force on the cross-sectional distortion of mercury jet caused by the Lorentz force. In addition, the image analysis reveals the jet instability which might be caused by the strong induced axial magnetic induction field, which is possibly the onset of a quadrupole effect. Nevertheless, the experimental

results clearly show that the magnetic induction field stabilizes the mercury jet by smoothing out the edges of the otherwise turbulent mercury flow, as previously reported in the literatures (Shercliff 1956, Gold 1962, Kozyrev 1981, Bernshtam 1982). The comprehensive optical diagnostic method allows us to have a better understanding of the behavior of a conducting jet moving in a high magnetic induction field environment. It plays a key role as a primary diagnostic of free mercury jet interacting with an intense proton beam under high-magnetic induction field. The optical diagnostics will allow us to interpret the beam-jet interaction length caused by the energy deposition from the proton beam as well as the splash velocity on the mercury jet surface with the aid of the high speed camera.

In order to achieve an understanding of liquid metal flow in a magnetic field, magnetohydrodynamic equations considering Lorentz force effect based on the Navier-Stokes equations as well as Maxwell equations are presented. The jet height is measured as a function of the magnetic field strength. The suppression of vorticity by the perpendicular magnetic field is introduced and the Stuart number gives the magnetic field effect.

Such a reducing effect in rotational motion on the jet surface is observed. As a result, the rotational motion of jet on the surface becomes more two dimensional motion of flow and thus the jet surface is more stabilized.

For magnetohydrodynamic flow investigation, the mercury jet behavior is observed for various magnetic field strengths and then the jet deformation is measured. The fluctuation on the jet surface decreases as the magnetic field

increases and the jet height increases slightly with magnetic field assuming the major and minor axis of Hg jet is reversed. Gravity affects the jet trajectory so that the jet bends down as it goes downstream. But this deflection of the jet by gravity is reduced at higher magnetic field. The jet axis becomes more straight toward the direction of magnetic field line.

The stabilizing effect of the magnetic field on a turbulent jet is observed. It is well known that the turbulent fluctuation is suppressed by magnetic field. It is observed that the wave length on the jet surface increases. Thus, the jet surface is getting flattened as the magnetic field increases. Also, the critical Reynolds number increases due to the magnetic field. Therefore, the jet is getting more stabilized. The measured intermittency shows the fluctuating surface of jet is getting more flattened as the magnetic field increases. The transverse magnetic field is more dominant to the jet stabilization though the longitudinal magnetic field is also influential. However, the jet has a different type of instability at magnetic fields larger than 10 T. The jet height becomes larger at larger magnetic field than 10 T. This is induced by the longitudinal current due to the tilted jet axis with respect to the magnet axis. Thus, the induced current generates a Lorentz force. As a result, additional anisotropic magnetic force is changing the jet height. As the magnetic field increase up to 5 T, the jet fluctuation decreases and the jet is more elongating to the flow direction. Thus, the jet height decreases from 0 T to 5 T. However, the magnetic pressure is influencing at larger than 5 T. Since the optical diagnostics depends on the side view of jet flow, it is hard to tell in which direction the jet deflects

since the jet and the magnetic field line is axially symmetric. However, the jet height clearly increases at 15 T, which indicates that the magnetic pressure apparently affects the jet height at 15 T.

The longitudinal jet velocity is not varied. Again, the jet elongation to the field direction by the magnetic field is indicated from this result. The longitudinal magnetic field does not influence the jet flow velocity. The transverse magnetic field will change the jet velocity. This is known as the Hartmann flow. The longitudinal magnetic field does not influence the longitudinal jet flow as it is shown in the governing MHD equation.

The pipe pressure driven by the syringe piston was measured. It shows that the Hg driving pressure is the same regardless of the magnetic field variation. The driving pressure at the Hg pipe inlet is independent of the magnetic field strength. Therefore, the mercury delivery is not influenced by the longitudinal magnetic field. However, there may be some pressure loss or jet velocity profile change due to the pipe bend. According to the velocity measurement at upstream, mid-stream, and downstream, it is not significantly different but it is same comparing with the flow velocity at 0 T. Therefore, the field effect at the pipe bend is expected to be somewhat negligible. To support this result, the pipe loss due to the geometry and friction is estimated.

The most interesting result is the observation of the interaction of the proton beam with the jet. The disruption as manifested by the jet break up is caused by the energy deposition of proton beam. The filaments begins on the bottom surface of Hg jet where the proton beam enters. The filaments ends

on the top surface of Hg jet where the proton beam leaves. The jet breakup is occurring at the center of jet where the maximum energy is deposited. This phenomenon is consistent with the beam trajectory across the jet as well as the results of energy deposition by the proton beam. However, Hg jet breakup is influenced by the magnetic field. The filamentation velocity increases as the beam intensity increases due to the increased energy deposition but the magnetic field reduces the filamentation velocity. The disruption length increases with both beam energy and intensity because the energy deposition to Hg jet increases as the beam energies and the beam intensities increase. However, the disruption length is also suppressed by the magnetic field because of the magnetic damping. As a result, the intensity threshold for breakup is lower at higher energy. The time scale of magnetic damping indicates the rate of decay of global kinetic energy due to the magnetic field strength. Thus, the energy decreases faster as the magnetic field increases. Therefore, it was measured that the onset of filamentation occurs later at higher magnetic field since the equivalent energy required for the generation of filamentation takes more time as the field strength increases. Also, the rising time to the maximum velocity increases as the magnetic field increases. It indicates that the magnetic damping is getting larger by the magnetic field in terms of the transient response time.

Finally, the performance and feasibility of utilizing liquid metal jet as a target for an intense proton beam is explored. The liquid jet target concept is based on the target being recycled after each pulse. Therefore, the power



of the target has to be evaluated in terms of the replacing capability. The optimal interaction length for the 24 GeV beam energy is in the region of 30 cm which corresponds to approximately 2 interaction length for mercury (Kirk *et al*, 2008). For a 20 m/s jet velocity, replacing two interaction lengths will be taken in 14 ms thus allowing for operations with a repetition rate of up to 70 Hz. The beam energy per pulse is 115 kJ for a beam of  $30 \times 10^{12}$  protons with 24 GeV beam energy. The disruption length at  $30 \times 10^{12}$  protons with 24 GeV beam energy in a magnetic field of 15 T is less than 20 cm at 24 GeV beam energy, thus preserving the 70 Hz beam repetition rate option, which corresponds to a beam power of 8 MW. It is validated that a target system capable of supporting proton beams with powers of up to 8 MW (Kirk *et al*, 2008).

# Bibliography

- [1] J. Alessi *et al*, 1998, “A proposal for an *R&D* program for targetry and capture at a muon collider source,” *Approved as BNL E951*
- [2] M. M. Alsharoa *et al*, 2003, “Recent progress in neutrino factory and muon collider research within the muon collaboration,” *submitted to Phys. Rev. ST Accel. Beams.*, [http : //www.cap.bnl.gov/mumu/pubs/prstab – 030422/prstab.pdf](http://www.cap.bnl.gov/mumu/pubs/prstab-030422/prstab.pdf)
- [3] C. M. Ankenbrandt *et al*, 1999, “Status of muon collider research and development and future plans” *Phys. Rev. ST Accel. Beams* **2**, **081001**
- [4] Robert P. Benedict, 1980, *Fundamentals of pipe flow*, John Wiley & Sons, Inc.
- [5] V. A. Bernshtam, S. V. Kozyrev, A. I. Él’kin, 1982, “Stability of flow of films of a conducting viscous liquid in longitudinal magnetic field,” *Magnetohydrodynamics*, **18**, pp.132
- [6] Herman Branover, 1978, *Magnetohydrodynamic flow in ducts*, John Wiley & Sons, Inc.
- [7] Michael P. Brenner, 2002, “Single bubble sonoluminescence,” *Reviews of Modern Physics*, **74**, pp.425-440
- [8] G. A. Carlson, 1975, “Dynamic tensile strength of mercury,” *J. Appl. Phys.*, v.46, pp.4069-4070
- [9] Donald Chang, Thomas Lundgren, 1961, “Duct flow in magnetohydrodynamics,” *Z. angew. Math. Phys.*, **12**, pp.100-114

- [10] I. G. Currie, 1993, *Fundamental Mechanics of Fluids*, Marcel Dekker, Inc.
- [11] P. A. Davidson, 1999, "Magnetohydrodynamics in materials processing," *Annu. Rev. Fluid Mech.*, **31**, pp.273-300
- [12] G. F. D. Duff, D. Naylor, 1966, *Differential equations of applied mathematics*, John Wiley & Sons, Inc.
- [13] I. Efthymiopoulos, A. Fabich, J. Lettry, 2005, "CERN installation," <http://cern.ch/proj-hiptarget>
- [14] I. Efthymiopoulos, 2008, "The MERIT experiment or nToF11," *MUTAC review*, [http : //www.hep.princeton.edu/ mcdonald/mumu/target/Ilias/ie080408.pdf](http://www.hep.princeton.edu/mcdonald/mumu/target/Ilias/ie080408.pdf)
- [15] A. Fabich, 2005, "nToF11: Multi-MW target experiment in TT2A," <http://cern.ch/proj-hiptarget>
- [16] A. G. Fedin, 1973, "Use of optical methods in investigating MHD processes" *Magnetohydrodynamics (English translation of Magnitaya Gidrodinamika)*, **9**, pp.301-308
- [17] T. A. Gabriel *et al*, 2001, "Targets for high-intensity particle production," *Part. Accel. Conf.*, Chicago, pp.737
- [18] T.A. Gabriel, J.R. Haines, T. J. McManamy, P. Spampinato, B. W. Riemer, 2001, "Targets for high intensity particle production," *Part. Accel. Conf.*, Chicago, pp737-741
- [19] J. Gallardo *et al*, 2001, "Calculation for a mercury jet target in a solenoid magnet capture system," *Part. Accel. Conf.*, Chicago, pp627-629
- [20] J. Gallardo *et al*, 2002, "First order perturbative calculations for a conducting liquid jet in a solenoid," *MUC-NOTE-TARGET-242, MU-047*
- [21] D. Gao, N. B. Morley, 2002, "Equilibrium and initial linear stability analysis of liquid metal falling film flows in a varying spanwise magnetic field," *Magnetohydrodynamics*, **38**, No.4, pp. 359-375
- [22] Richard R. Gold., 1962, "Magnetohydrodynamic pipe flow: Part 1.," *J. Fluid Mech.*, **13**, pp.505-512

- [23] R. J. Goldstein, 1991, *Optical systems for flow measurement*, McGraw-Hill, Inc.
- [24] Andrew Gray and G. B. Mathews, 1966, *A treatise on Bessel functions and their applications to physics*, Dover, Inc.
- [25] V. Graves, 2007, "MIT testing results" *MUTAC review*, [http : //www.hep.princeton.edu/mcdonald/mumu/target/graves/VGraves-070418.pdf](http://www.hep.princeton.edu/mcdonald/mumu/target/graves/VGraves-070418.pdf)
- [26] J. Hartmann, 1937, "Hg dynamics I," *Kgl. Danske Videnskab Selskabs Math. Fys.*, Medd. 15, No.6
- [27] H. Ito, 1960, "Pressure losses in smooth pipe bends," *Trans. ASME., J. Basic Eng.*, **82**, pp.131
- [28] Uhlenbusch J., Fishcer E., 1961, "Hydromagnetische strömung im kreiszylindrischen rohr," *Z. Phys.*, **165**, pp.190-198
- [29] Colin Johnson, 2002, "A self focusing mercury jet target," *CERN-NUFACT-113*
- [30] T. Kakuta, T. Shikama, M. Marui, 1999, "Optical fibers and their applications for radiation measurement," *Seventh Int. Conf. on Nuclear Engineering*, Tokyo, Japan, pp.19
- [31] H. G. Kirk *et al*, 2001, "Target studies with BNL E951 at the AGS," *Part. Accel. Conf.*, Chicago, pp.1531-1537
- [32] H. G. Kirk *et al*, 2008, "The MERIT high power target experiments at the CERN PS," *European Part. Accel. Conf.*, Genoa, Italy, *WEPP169*
- [33] B. A. Kolovandin, 1965, "Stability of flow of conducting liquid with free surface in the presence of magnetic and electric fields," *Prikl. Mekh.*, **1**, No. 11, pp.95
- [34] S. V. Kozyrev, A. I. Él'kin, 1981, "Stability of flow of thin films of electrically conducting liquid in crossed magnetic and electric fields," *Magnetohydrodynamics*, **17**, No. 4, pp.353

- [35] J. Lettry *et al*, 2003, “Thermal shocks and magnetohydrodynamics in high power mercury targets,” *J. Phys. G: Nucl. and Part. Phys.*, **29**, pp.1621
- [36] Junwoo Lim *et al*, 1998, “Control of streamwise vortices with uniform magnetic fluxes,” *Physics of Fluids*, **10**, 8, pp.1997
- [37] S. P. Lin, D. J. Kang, 1987, “Atomization of a liquid jet,” *Physics of Fluids*, **30**, pp.2000-2006
- [38] K. T. McDonald *et al.*, 2001, “The primary target facility for a neutrino factory based on muon beams,” *Proc. Part. Accel. Conf.*, Chicago, IL, pp.1583
- [39] K. T. McDonald, 2000, “Cooling of a target by helium gas,” *Princeton / $\mu/\mu/00-25$*
- [40] K. T. McDonald, 2000, “Damping of radial pinch effects,” *Princeton / $\mu/\mu/00-26$*
- [41] K. T. McDonald, 2000, “Magnetohydrodynamics of a continuous mercury jet coaxially entering a solenoid,” *Princeton / $\mu/\mu/00-29$*
- [42] K. T. McDonald, 2000, “Magnetohydrodynamics of a pulsed mercury jet entering a solenoid at an angle,” *Princeton / $\mu/\mu/00-30$*
- [43] K. T. McDonald, 2000, “Optics for E951 target tests in the A3 beamline,” *Princeton / $\mu/\mu/00-28$*
- [44] N. V. Mokhov, 2000, “Particle production for a muon storage ring: I. Targetry and  $\pi/\mu$  yield” *MUC0169*, <http://www-mucool.fnal.gov/mcnotes/muc0169.pdf>
- [45] Neil B. Morley *et al*, 2000, “Liquid magnetohydrodynamics - recent progress and future directions for fusion,” *Fusion Engineering and Design*, **51**, pp.701-713
- [46] Neil B. Morley, Sergey Smolentsev, Donghong Gao, 2002, “Modeling infinite/axisymmetric liquid metal magnetohydrodynamic free surface flows,” *Fusion Engineering and Design*, **63**, pp. 343-351

- [47] S. Osaki, R. Palmer, M. Zisman, J. Gallardo, 2001, “Neutrino factory feasibility study 2,” *BNL-52623*, Ch.3, [http :  
//www.cap.bnl.gov/mumu/studii/FS2-report.html](http://www.cap.bnl.gov/mumu/studii/FS2-report.html)
- [48] N. Otsu, 1979, “A threshold selection method from gray-level histograms,” *IEEE Trans. Sys., Man., Cyber.*, **9**, pp. 62-66
- [49] SAE, 1960, “Aero-space thermodynamics manual,” pp. A18-A20
- [50] R. Samulyak, 2006, “Target simulations” *MUTAC review*, [http :  
//www.hep.princeton.edu/mcdonald/mumu/target/samulyak/  
mutac06-samulyak-targetsimulations.pdf](http://www.hep.princeton.edu/mcdonald/mumu/target/samulyak/mutac06-samulyak-targetsimulations.pdf)
- [51] N. Simos, 2005, “MERIT experiment window study,” *BNL Review*, [http :  
//www.hep.princeton.edu/mcdonald/mumu/target/simos/  
Simos-121205.pdf](http://www.hep.princeton.edu/mcdonald/mumu/target/simos/Simos-121205.pdf)
- [52] Sergei Striganov, 2008, Private communication
- [53] Shuzo Oshima, Ryuichiro Yamane, Yoshihiro Mochimaru, Toshihiro Matsuoka, 1987, “The shape of a liquid metal jet under a non-uniform magnetic field,” *JSME International Journal*, **30**, No.261, pp.437-448
- [54] R. B. Palmer, 1998, “Muon collider design,” *Report BNL-65242, CAP-200-MUON-982C*
- [55] Mark A. Pinsky, 1991, *Partial differential equations and boundary value problems with applications*, McGraw-Hill, Inc.
- [56] R. D. Reitz, F. V. Bracco, 1982, “Mechanism of atomization of a liquid jet,” *Physics of Fluids*, **25**, pp.1730-1742
- [57] Uflyand Y. S., 1960, “Hartmann problem for a circular tube,” *Soviet Phys.*, **5**, pp.1194-1196
- [58] Roman Samulyak, 2006, “Target simulations,” *MUTAC Review*, [http :  
//www.hep.princeton.edu/mcdonald/mumu/target/samulyak/  
mutac06-samulyak-targetsimulations.pdf](http://www.hep.princeton.edu/mcdonald/mumu/target/samulyak/mutac06-samulyak-targetsimulations.pdf)
- [59] J. A. Shercliff, 1953, “Steady motion of conducting fluids in pipes under transverse magnetic fields,” *Proc. Camb. Phil. Soc.*, **49**, pp.136-144

- [60] J. A. Shercliff, 1956, "The flow of conducting flows in circular pipes under transverse magnetic fields," *J. Fluid Mech.*, **13**, pp.644-666
- [61] J. A. Shercliff, 1962, "Magnetohydrodynamic pipe flow: Part 2 High Hartmann number," *J. Fluid Mech.*, **13**, pp.513-518
- [62] J. A. Shercliff, 1965, *A textbook of magnetohydrodynamics*, Pergamon Press
- [63] P. T. Spampinato *et al*, 2005, "A free jet mercury system for use in a high power target experiment," *Part. Accel. Conf.*, Knoxville, TN, pp.1637
- [64] P. Thieberger, H. G. Kirk, R. J. Weggel, K. T. MacDonald, 2003, "Moving solid metallic targets for pion production in the muon collider/neutrino factory project," *Proc. Part. Accel. Conf.*, Portland, OR, pp.1634
- [65] N. Tsoupas *et al*, 2003, "Injection acceleration and extraction of high intensity proton beam for the neutrino facility project at BNL," *Part. Accel. Conf.*, Portland, OR, pp.1637
- [66] C. D. West, 2000, "Cavitation in a mercury target," *ORNL/TM-2000-263*
- [67] H. Q. Yang, 1992, "Asymmetric instability of a liquid jet," *Physics of Fluids*, **30**, pp.681-689
- [68] K. T. Yen, 1967, "Role of intermittency in free turbulent flows," *American Institute of Aeronautics and Astronautics*, **5**, No. 12 pp.2187-2192
- [69] W. M. Yao *et al*, 2006, "Accelerator physics of colliders" *Journal of Physics*, **33**, No.1, pp.35-62

# Appendix A

## Tabular Data for Chapter 3 and Chapter 4

### A.1 Specifications of Optics

Table A.1: Specifications of optical components in optical diagnostics.

Item	Value
<b>Right angle prism mirror</b>	Gold coated, $25 \times 25 \times 35.4$ , Surface flatness $\lambda/10$
<b>Gradient index lens</b>	
Size	d=1.0 mm, L=2.48 mm
Numerical aperture	0.5
Working distance	Infinity
Coating	AR coated at 800 ~ 960 nm
Sapphire ball lens	D=0.5 mm, $Al_2O_3$ , Index of refraction=1.77
<b>Retro-reflecting Parabolic mirror</b>	
Diameter	76.2 mm
Thickness	12.7 mm
Focal length	444 mm
Coating	Gold
<b>Microscope objective</b>	
Magnification	40 $\times$

*Continued on next page*



Table A.1: *Continued from previous page*

Item	Value
Numerical aperture	0.65
Working distance	0.6 mm
Clear aperture	5.0 mm
Power	160 mm (tube length) / f
<b>Optical fiber</b>	
Number of picture elements	30000
Jacketing diameter	800 $\mu\text{m}$
Picture elements area diameter	720 $\mu\text{m}$
Coating diameter	960 $\mu\text{m}$
Core material	$\text{GeO}_2$ containing Silica
Coating material	Silicone
Numerical aperture	0.35
Allowable bending radius	40 mm
Core diameter	200 $\mu\text{m}$

## A.2 Mercury Properties

Table A.2: Properties of mercury.

Property	Value	Unit
Atomic number	80	-
Atomic mass	200.59	-
Number of protons/electrons	80	-
Number of neutrons	121	-
Classification	Transition metal	-
Melting point	-38.87	°C
Boiling point	356.58	°C
Density	13.456 at 25 °C	$g/cm^3$
Naturally occurring isotopes	Hg-194 Hg-206	-
Group in periodic table	12	-
Period in periodic table	6	-
Electrical conductivity	$1.06 \times 10^6$ at 25 °C	$\Omega^{-1}m^{-1}$
Thermal conductivity	8.34	$W m^{-1} K^{-1}$ at 27 °C
Specific heat	0.139	$J g^{-1} K^{-1}$
Heat of vaporization	59.229	kJ/mol
Heat of fusion	2.295	kJ/mol
Electrical resistivity	961 at 25 °C	$n\Omega \cdot m$
Speed of sound	1451.4 at 20 °C	m/s
Coefficient of thermal expansion	$60 \times 10^{-6}$ at 20 °C	$K^{-1}$
Bulk modulus	25	GPa
Dynamic viscosity	1.552	$kg m^{-1} s^{-1}$
Kinematic viscosity	$1.145 \times 10^{-4}$	$m^2 s^{-1}$
Dielectric constant	1.00074	-
Surface tension	485.5 (Hg-Air) at 25 °C	mN/m °C
Magnetic permeability	$4\pi \times 10^{-7}$	H/m

# Appendix B

## Mathematical Derivation for Chapter 2

### B.1 The governing equations for MHD in cylindrical coordinates

The momentum equations in the  $(r, \theta, z)$  coordinates in Fig. 2.2 can be written as follows:

$$\begin{aligned} & -\rho\left(v_r \frac{\partial v_r}{\partial r} + \frac{v_\theta}{r} \frac{\partial v_r}{\partial \theta} + v_z \frac{\partial v_r}{\partial z}\right) - \frac{\partial p_t}{\partial r} - \rho g \cos \theta + \eta\left(\frac{\partial^2 v_r}{\partial r^2} + \frac{1}{r} \frac{\partial v_r}{\partial r} + \frac{1}{r^2} \frac{\partial^2 v_r}{\partial \theta^2} + \frac{\partial^2 v_r}{\partial z^2}\right) \\ & + \frac{1}{\mu}\left(B_r \frac{\partial B_r}{\partial r} + \frac{B_\theta}{r} \frac{\partial B_r}{\partial \theta} + B_z \frac{\partial B_r}{\partial z}\right) = \rho \frac{\partial v_r}{\partial t} , \end{aligned} \tag{B.1}$$

$$\begin{aligned} & -\rho\left(v_r \frac{\partial v_\theta}{\partial r} + \frac{v_\theta}{r} \frac{\partial v_\theta}{\partial \theta} + v_z \frac{\partial v_\theta}{\partial z}\right) - \frac{1}{r} \frac{\partial p_t}{\partial \theta} + \rho g \sin \theta + \eta\left(\frac{\partial^2 v_\theta}{\partial r^2} + \frac{1}{r} \frac{\partial v_\theta}{\partial r} + \frac{1}{r^2} \frac{\partial^2 v_\theta}{\partial \theta^2} + \frac{\partial^2 v_\theta}{\partial z^2}\right) \\ & + \frac{1}{\mu}\left(B_r \frac{\partial B_\theta}{\partial r} + \frac{B_\theta}{r} \frac{\partial B_\theta}{\partial \theta} + B_z \frac{\partial B_\theta}{\partial z}\right) = \rho \frac{\partial v_\theta}{\partial t} , \end{aligned} \tag{B.2}$$

$$\begin{aligned}
& -\rho(v_r \frac{\partial v_z}{\partial r} + \frac{v_\theta}{r} \frac{\partial v_z}{\partial \theta} + v_z \frac{\partial v_z}{\partial z}) - \frac{\partial p_t}{\partial z} + \eta(\frac{\partial^2 v_z}{\partial r^2} + \frac{1}{r} \frac{\partial v_z}{\partial r} + \frac{1}{r^2} \frac{\partial^2 v_z}{\partial \theta^2} + \frac{\partial^2 v_z}{\partial z^2}) \\
& + \frac{1}{\mu}(B_r \frac{\partial B_z}{\partial r} + \frac{B_\theta}{r} \frac{\partial B_z}{\partial \theta} + B_z \frac{\partial B_z}{\partial z}) = \rho \frac{\partial v_z}{\partial t} ,
\end{aligned} \tag{B.3}$$

where  $p_t = p + \frac{\mathbf{B}^2}{2\mu}$ . The magnetic induction equation in the  $(r, \theta, z)$  coordinate directions can be written as follows:

$$\begin{aligned}
& \frac{1}{\mu\sigma}[\frac{\partial^2 B_r}{\partial r^2} + \frac{1}{r} \frac{\partial B_r}{\partial r} + \frac{1}{r^2} \frac{\partial^2 B_r}{\partial \theta^2} + \frac{\partial^2 B_r}{\partial z^2}] + \frac{1}{r} B_r(r \frac{\partial v_r}{\partial r}) + \frac{1}{r} B_\theta \frac{\partial v_r}{\partial \theta} + B_z \frac{\partial v_r}{\partial z} \\
& - \frac{1}{r} v_r(r \frac{\partial B_r}{\partial r}) - \frac{1}{r} v_\theta \frac{\partial B_r}{\partial \theta} - v_z \frac{\partial B_r}{\partial z} = \frac{\partial B_r}{\partial t} ,
\end{aligned} \tag{B.4}$$

$$\begin{aligned}
& \frac{1}{\mu\sigma}[\frac{\partial^2 B_\theta}{\partial r^2} + \frac{1}{r} \frac{\partial B_\theta}{\partial r} + \frac{1}{r^2} \frac{\partial^2 B_\theta}{\partial \theta^2} + \frac{\partial^2 B_\theta}{\partial z^2}] + \frac{1}{r} B_r(r \frac{\partial v_\theta}{\partial r}) + \frac{1}{r} B_\theta \frac{\partial v_\theta}{\partial \theta} + B_z \frac{\partial v_\theta}{\partial z} \\
& - \frac{1}{r} v_r(r \frac{\partial B_\theta}{\partial r}) - \frac{1}{r} v_\theta \frac{\partial B_\theta}{\partial \theta} - v_z \frac{\partial B_\theta}{\partial z} = \frac{\partial B_\theta}{\partial t} ,
\end{aligned} \tag{B.5}$$

$$\begin{aligned}
& \frac{1}{\mu\sigma}[\frac{\partial^2 B_z}{\partial r^2} + \frac{1}{r} \frac{\partial B_z}{\partial r} + \frac{1}{r^2} \frac{\partial^2 B_z}{\partial \theta^2} + \frac{\partial^2 B_z}{\partial z^2}] + \frac{1}{r} B_r(r \frac{\partial v_z}{\partial r}) + \frac{1}{r} B_\theta \frac{\partial v_z}{\partial \theta} + B_z \frac{\partial v_z}{\partial z} \\
& - \frac{1}{r} v_r(r \frac{\partial B_z}{\partial r}) - \frac{1}{r} v_\theta \frac{\partial B_z}{\partial \theta} - v_z \frac{\partial B_z}{\partial z} = \frac{\partial B_z}{\partial t} .
\end{aligned} \tag{B.6}$$

The Ampère's law can be written as

$$\begin{aligned}
j_r &= \frac{1}{\mu}(\frac{1}{r} \frac{\partial B_z}{\partial \theta} - \frac{\partial B_\theta}{\partial z}) , \\
j_\theta &= \frac{1}{\mu}(-\frac{\partial B_z}{\partial r} + \frac{\partial B_r}{\partial z}) , \\
j_z &= \frac{1}{\mu}(\frac{\partial B_\theta}{\partial r} - \frac{1}{r} \frac{\partial B_r}{\partial \theta}) ,
\end{aligned} \tag{B.7}$$

and the equation of continuity and the solenoidal condition for the magnetic field are

$$\frac{1}{r} \frac{\partial}{\partial r}(rv_r) + \frac{1}{r} \frac{\partial v_\theta}{\partial \theta} + \frac{\partial v_z}{\partial z} = 0 , \quad (\text{B.8})$$

$$\frac{1}{r} \frac{\partial}{\partial r}(rB_r) + \frac{1}{r} \frac{\partial B_\theta}{\partial \theta} + \frac{\partial B_z}{\partial z} = 0 . \quad (\text{B.9})$$

## B.2 Derivation of Rayleigh's instability at an interface separating two flows in magnetic field

### B.2.1 *kinematic boundary condition at interface*

We consider the  $(x, y, z)$  coordinate system in Fig. 2.1. A particle of fluid that is at some time on the free surface will always remain on the free surface. Then, since the equation of the free surface is  $y - (\xi + a) = 0$ , it follows that

$$\frac{D}{Dt}(y - (\xi + a)) = 0 . \quad (\text{B.10})$$

Neglecting quadratically small terms, Eqn. (B.10) yields at the interface( $y = \pm a$ ),

$$\frac{\partial \xi}{\partial t} + U_i \frac{\partial \xi}{\partial x} = \frac{\partial \phi_i}{\partial y} \quad (\text{B.11})$$

In the region  $(-a < y < a)$ , the velocity potential  $\phi_i$  must satisfy  $\frac{\partial^2 \phi_1}{\partial x^2} + \frac{\partial^2 \phi_1}{\partial y^2} = 0$ ,  $|\nabla \phi_1| = \text{finite}$ . In the region  $y > a$ ,  $y < -a$ , the velocity potential must satisfy  $\frac{\partial^2 \phi_2}{\partial x^2} + \frac{\partial^2 \phi_2}{\partial y^2} = 0$ ,  $|\nabla \phi_2| = \text{finite}$ . In view of the shape of the interface, the solutions should be trigonometric in  $x$ , then the  $y$  dependence will be exponential. In view of the finite conditions of velocity potentials, the negative exponential should be rejected for  $\phi_1$  and the positive exponential should be rejected for  $\phi_2$ . Therefore, the general solutions are

$$\begin{aligned} \phi_1(x, y, t) &= A_1 e^{(2\pi/\lambda)y} e^{i(2\pi/\lambda)(x-ct)} , \\ \phi_2(x, y, t) &= A_2 e^{-(2\pi/\lambda)y} e^{i(2\pi/\lambda)(x-ct)} \end{aligned} \quad (\text{B.12})$$

Imposing the kinematic conditions on these solutions, the coefficients are determined at  $y = a$  and  $y = -a$  respectively.

$$\begin{aligned}\phi_1(x, y, t) &= -i\epsilon(c - U_1)e^{i(2\pi/\lambda)(x-ct)}, \\ \phi_2(x, y, t) &= i\epsilon(c - U_2)e^{i(2\pi/\lambda)(x-ct)}\end{aligned}\quad (\text{B.13})$$

,where  $U_1 = U_1(a)$ ,  $U_2 = U_2(a)$ .

$$\begin{aligned}\phi_1(x, y, t) &= i\epsilon(c - U_1)e^{i(2\pi/\lambda)(x-ct)} \\ \phi_2(x, y, t) &= -i\epsilon(c - U_2)e^{i(2\pi/\lambda)(x-ct)}\end{aligned}\quad (\text{B.14})$$

,where  $U_1 = U_1(-a)$ ,  $U_2 = U_2(-a)$ .

Since the perturbed surface at  $y = a$  and  $y = -a$  are supposed to be symmetric, half of the jet section for the surface stability is considered in the following work.

### B.2.2 *hydrodynamic stability in magnetic field*

Substituting the perturbed expressions into the equations of motion, neglecting second order terms in the perturbed quantities, and making use of the fact that  $U$ ,  $P$  satisfy the flow equations and the current density in Lorentz force term can be represented using Ohm's law, we have the linearized equations governing the motion of disturbance.

$$\begin{aligned}\frac{\partial v'_{xi}}{\partial t} + U_i \frac{\partial v'_{xi}}{\partial x} + v'_{xi} \frac{dU_i}{dy} \\ = -\frac{1}{\rho_i} \frac{\partial p'_i}{\partial x} - \frac{\sigma_i}{\rho_i} B_y^2 v'_{xi} + \frac{\sigma_i}{\rho_i} B_x B_y v'_{yi}\end{aligned}\quad (\text{B.15})$$

$$\begin{aligned}\frac{\partial v'_{yi}}{\partial t} + U_i \frac{\partial v'_{yi}}{\partial x} \\ = -\frac{1}{\rho_i} \frac{\partial p'_i}{\partial y} - \frac{\sigma_i}{\rho_i} B_x^2 v'_{yi} + \frac{\sigma_i}{\rho_i} B_x B_y v'_{xi}\end{aligned}\quad (\text{B.16})$$

,where  $p'_i = f_i(c, \lambda, y)e^{i(2\pi/\lambda)(x-ct)}$ .

The perturbed velocity  $v'_x, v'_y$  are given

$$\begin{aligned} v'_x &= \frac{\partial \phi_1}{\partial x} = i\left(\frac{2\pi}{\lambda}\right)A_1 e^{(2\pi/\lambda)y} e^{i(2\pi/\lambda)(x-ct)} \\ v'_y &= \frac{\partial \phi_1}{\partial y} = \left(\frac{2\pi}{\lambda}\right)A_1 e^{(2\pi/\lambda)y} e^{i(2\pi/\lambda)(x-ct)} \end{aligned} \quad (\text{B.17})$$

Putting Eqn. (B.17) into Eqn. (B.15) and Eqn. (B.16), equate the hydrodynamic pressures since it is isotropic, which leads to Rayleigh's stability equation for the flow in magnetic field.

$$\sigma_1 B_x B_y + i\sigma_1 B_x^2 = \sigma_1 B_y^2 i - \sigma_1 B_x B_y + \rho_1 \left(\frac{\lambda}{2\pi}\right) \frac{d^2 U_1}{dy^2} \quad (\text{B.18})$$

, where  $U_1 = U_1(y)$ . In the same manner, the Rayleigh's stability equation for the upper flow in magnetic field is derived.

$$\sigma_2 B_x^2 + \sigma_2 B_x B_y i = \sigma_2 B_y^2 - i\sigma_2 B_x B_y - \rho_2 i \left(\frac{\lambda}{2\pi}\right) \frac{d^2 U_2}{dy^2} \quad (\text{B.19})$$

, where  $U_2 = U_2(y)$ .

### B.2.3 *dynamic boundary condition at interface*

The difference of the normal stresses must be balanced by the normal stress induced by surface tension at the interface.

$$(P_1 + \frac{\partial P_1}{\partial y} \xi + \frac{\partial^2 P_1}{\partial y^2} \xi + \dots + p'_1) - (P_2 + \frac{\partial P_2}{\partial y} \xi + \frac{\partial^2 P_2}{\partial y^2} \xi + \dots + p'_2) + \Gamma \frac{\partial^2 \xi}{\partial x^2} = 0 \quad (\text{B.20})$$

, where  $\Gamma$  is surface tension.

Considering the gravity force in the free surface waves, Eqn. (B.20) can be rewritten as follows.

$$\begin{aligned} &(\rho_2 - \rho_1)g \cos \theta + \rho_1(c - U_1)^2 \left(\frac{2\pi}{\lambda}\right) + \rho_2(c - U_2)^2 \left(\frac{2\pi}{\lambda}\right) \\ &+ \rho_1(c - U_1) \frac{dU_1}{dy} - \rho_2(c - U_2) \frac{dU_2}{dy} + iB_y^2(\sigma_1(c - U_1) + \sigma_2(c - U_2)) \\ &+ B_x B_y(\sigma_2(c - U_2) - \sigma_1(c - U_1)) - \Gamma \left(\frac{2\pi}{\lambda}\right)^2 = 0 \end{aligned} \quad (\text{B.21})$$

,where  $U_1 = U_1(a)$ ,  $U_2 = U_2(a)$ .

Consider the case that  $U_2 = 0$ ,  $\frac{dU_2}{dy} = 0$ ,  $\rho_2 = 0$ ,  $\sigma_2 = 0$ . This would correspond to the stationary fluid on the upper and the density and conductivity of the upper fluid are very small compared with these of the lower fluid. The wave velocity is represented as follow.

$$\begin{aligned}
c = [ & -\rho_1 \frac{dU_1}{dy} + B_x B_y \sigma_1 - i B_y^2 \sigma_1 + 2 \left( \frac{2\pi}{\lambda} \right) \rho_1 U_1 \\
& \pm \sqrt{\rho_1^2 \left( \frac{dU_1^2}{dy} \right) + 4 \left( \frac{2\pi}{\lambda} \right) \cos \theta g \rho_1^2 - 2 B_x B_y \rho_1 \sigma_1 \frac{dU_1}{dy} + 2 i B_y^2 \rho_1 \sigma_1 \frac{dU_1}{dy}} \\
& \left. + B_x^2 B_y^2 \sigma_1^2 - 2 i B_x B_y^3 \sigma_1^2 - B_y^4 \sigma_1^2 + 4 \left( \frac{2\pi}{\lambda} \right)^3 \rho_1 \Gamma \right] \times \frac{1}{2 \left( \frac{2\pi}{\lambda} \right) \rho_1} \quad (B.22)
\end{aligned}$$